CHAPTER 1

Introduction and Overview

1.1 Mission and contributions to NOAA

The mission of the Climate Diagnostics Center (CDC) is to advance understanding and predictions of weather and climate variations on time scales ranging from a week to centuries. To achieve its mission, CDC develops and applies a wide range of research methods, particularly emphasizing state-of-the-art diagnostic techniques, to elucidate fundamental processes governing climate phenomena such as droughts, floods, and the El Niño–Southern Oscillation, and to identify the causes of longer-term (decadal to centennial) climate variations. CDC also performs extensive intercomparisons of observational and climate model data, an activity vital to improving current research and prediction models.

The development of improved climate assessments and predictions enhances the Nation's economic and environmental security, and is a fundamental part of NOAA's mission. Diagnostic studies, for which CDC has exceptional breadth and expertise, vitally contribute to this process by linking basic observational and theoretical research to improvements in operational climate predictions and, ultimately, to the development of new climate products that better serve the needs of the public and decision-makers (**Fig. 1.1**). NOAA Strategic Goals directly addressed by CDC research include: 1) Implementing seasonal to interannual climate forecasts; 2) Predicting and assessing decadal-to-centennial changes; and 3) Advancing short-term forecast and warning services.

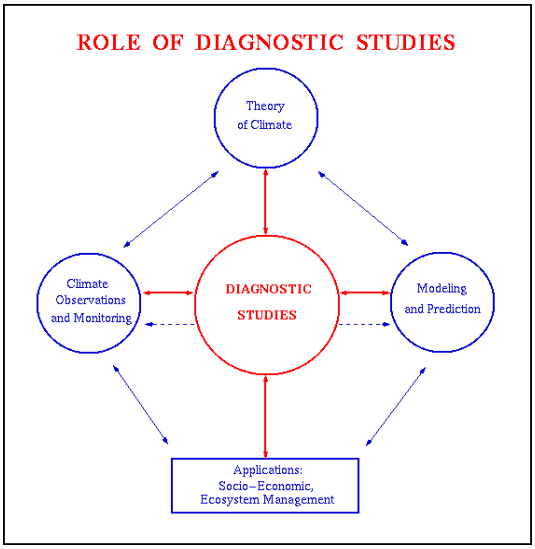

Fig. 1.1 Illustration of the linkages between diagnostic studies and other climate disciplines.

1.2 Background and organization

The NOAA Climate Diagnostics Center was formed in 1993 through a Memorandum of Agreement (MOA) between the

Office of Oceanic and Atmospheric Research (OAR) and the Office of Global Programs (OGP), with personnel derived from what had formerly been the Climate Research Division of the Climate Monitoring and Diagnostics Laboratory. The purpose of the OAR-OGP agreement was to establish a unique, focused center of expertise within NOAA to develop and apply diagnostic methods that would (i) aid in understanding the dominant processes influencing climate variability, and (ii) link observational analyses to model testing and evaluation. Under the terms of the MOA, CDC is managed as one of the Research Laboratories in OAR.

CDC is staffed by NOAA personnel and affiliated scientists from the University of Colorado Cooperative Institute for Research in Environmental Sciences (CIRES), with approximately forty CIRES staff and fourteen federal staff directly affiliated with the CDC. In order to more explicitly recognize this large and focused set of joint activities, a University Center within CIRES, also named the Climate Diagnostics Center, was formed in 1997. This organization integrates and coordinates climate research in NOAA/OAR and CIRES with other existing University research and instructional programs, thereby enhancing prospects for mutually beneficial collaborations among NOAA and University scientists over a broad range of disciplines.

Specific goals of ongoing CDC research include: (i) identifying key processes contributing to extreme short-term climate events, including major droughts and floods; (ii) advancing understanding and predictions of El Niño-Southern Oscillation, other major modes of climate variability and their global and regional impacts; (iii) developing new diagnostic techniques to improve determinations of fundamental atmospheric quantities, such as atmospheric heating; (iv) improving monitoring and descriptions of climate variability; (v) diagnosing general circulation and operational prediction models to identify areas where model improvements are needed; (vi) identifying sources for climate variability on decadal and longer time scales and assessing to what extent they may be predictable; (vii) investigating the role of ocean-atmosphere interactions in modulating longer-term variability; (viii) developing new approaches, including stochastic methods, for climate diagnostics and predictions; and (ix) improving interactions and communications with potential external users in areas such as water, energy, and environmental resources management, in order to increase the value to society of climate analyses and predictions.

CDC also conducts joint climate research with scientists at other universities, NOAA research laboratories and other national laboratories, and with the National Centers for Environmental Prediction on projects aimed at improving medium-range weather forecasts, seasonal-to-interannual climate predictions, and developing new climate products. Strong and growing interactions exist with the Geophysical Fluid Dynamics Laboratory in climate model diagnostics, and with NCEP Climate Prediction Center and Environmental Modeling Center

on real-time diagnostics, seasonal climate predictions and the development of experimental medium-range and seasonal climate forecasts. CDC also is one of five Applied Research Centers (ARCs) within the Climate Dynamics and Experimental Prediction Program of the Office of Global Programs. The ARCs serve as a system of linked centers focusing on applied climate research, with a major unifying goal being to improve predictions of climate on time scales ranging from a season to a decade. CDC is one of the central contributors to ARC research, and CDC scientists have developed collaborations across the ARC network. Important objectives of ARC research include supporting the development of improved forecast capabilities and experimental climate products for applications by NCEP, the International Research Institute for Climate Prediction (IRI), and regional assessments projects funded by the NOAA Office of Global Programs. In addition, CDC collaborates extensively with CIRES and other University of Colorado partners in an OGP-supported regional assessment of Water, Climate and Society in the Interior Western United States.

1.3 Research themes

CDC research is organized into three principal themes: 1) Intraseasonal-to-Interannual Climate Research, including modeling and prediction research and empirical and process studies; 2) Decadal-to-Centennial Climate Research; and 3) Experimental Climate Services. Chapters 2–6 provide reviews of recent research accomplishments in these areas; chapter 7 describes CDC's computing, network, web, and data services; chapter 8 lists CDC publications since 1997; and chapter 9 provides an organizational chart and list of current CDC personnel associated with each of these areas.

The first two themes directly support the long-term NOAA Strategic Goals to "Implement Seasonal to Interannual Climate Forecasts" and "Predict and Assess Decadal to Centennial Climate Change". Research within the first theme extends down to sub-seasonal time scales in order to address emerging research priorities linking climate and weather. The third theme was developed to support future requirements for NOAA's Climate Services, which in FY01 was supported as a new program. Research in this third component focuses on the climate-society interface, and particularly on how interactions between scientists and decision-makers can accelerate development of more useful climate products, and thereby improve the value of the climate information that NOAA will provide to address a broad range of social, economic, and environmental issues.

All of the above themes involve ongoing, long-term research that is central to NOAA's mission. Within the general themes, specific research foci are adjusted as needed to meet current mission requirements or anticipated future priorities. For example, over the past few years, CDC has placed increasing emphasis on developing new capabilities for forecasting climate probability distributions, including the likelihood of extreme events. This enhanced research

emphasis has led to new advances in ensemble prediction methods, the development of new stochastic approaches to modeling and predicting climate variability, and new experimental forecast products. CDC is also gradually redirecting resources to increase research into the mechanisms and predictability of decadal-to-centennial climate variability and assessment of long-term climate change, including diagnosis of GFDL models used to study climate change in response to human-induced forcings.

1.4 Future directions

CDC will continue its role as a focused center of expertise within NOAA for developing and applying diagnostic analyses to address fundamental climate problems. This work will increasingly involve intercomparisons of observational and climate model data, an activity central to improving climate models.

Continuing key research areas

Vigorous CDC research will continue in specific areas where CDC has special expertise and provides major contributions to NOAA's mission. Such areas include:

- Diagnostic and modeling studies to improve understanding and predictions of intraseasonal variability.

- Studies to advance fundamental scientific understanding of El Niño-Southern Oscillation (ENSO) and, more generally, the roles of ocean-atmosphere interactions in both the tropics and extratropics in interannual to multi-decadal climate variability.

- Model-based research to assess and improve climate models used in analyses, short-term climate predictions and climate change projections, with particular emphasis on NCEP operational prediction models and GFDL climate models. Increasingly, advances in this area require expertise in understanding and diagnosing fundamental physical processes, such as convection, cloud-radiation interactions, and land surface-atmosphere interactions, and the use of ensemble methods for analyses and predictions.

- Development of stochastic approaches for climate modeling, parameterization, and prediction.

Emerging research thrusts

Emerging areas of new research are strongly motivated by a few overarching questions that CDC is well-positioned to address, including:

- What are the links between climate variability and weather, particularly extreme events such as floods, droughts, and hurricanes, and how might these links be exploited to develop new and more useful NOAA climate forecast products?

- What are the relationships between short-term climate phenomena such as El Niño, decadal variability, and global change, and to what extent do these relationships offer prospects for improved

understanding and predictions of regional climate variability and change?

• How can climate information and products be improved to increase societal benefits and mitigate potential adverse impacts related to climate variability and change?

Corresponding emerging areas for CDC research include:

• *Improving understanding and predictions of the links between climate and extreme weather events.*

Our fundamental objective is to increase NOAA's lead-time capabilities for providing watches and warnings of large-scale severe weather and climate events. Research goals include increasing the skill and utility of forecasts on time scales ranging from approximately ten days to a season, and developing new products that extend NOAA's current operational prediction capabilities for high impact weather and climate events. This research supports the NWS operational objective to create an integrated suite of forecast products spanning time scales from minutes to years in advance. The FY01 budget includes new funding in this area under the Climate Observation and Services line, based on an Initiative developed in part by CDC.

• *Improving understanding and forecasts of sub-seasonal tropical-midlatitude interactions.*

The fundamental goal is to improve NOAA's weather and climate forecasts through advances in observations, analyses, understanding, and modeling of sub-seasonal tropical-midlatitude interactions and their regional impacts on the U.S. This area builds on research indicating that sub-seasonal tropical variability, such as the Madden-Julian Oscillation, can modulate mid-latitude sub-seasonal weather variability in a manner somewhat analogous to El Niño's effects on seasonal climate, and on other work indicating that current models are severely deficient in simulating this tropical variability. An FY02 Initiative in this area has been developed jointly between CDC and ETL, and is a component within the NOAA FY02 Climate Observations and Services budget currently before Congress.

• *Conducting regional integrated science and assessments research.*

It has become increasingly clear that, to be useful for many applications, climate information and forecasts must be provided at regional-to-local scales. Accordingly, CDC will devote increased emphasis on assessing predictability and developing new climate products at regional scales, with the interior western U.S. serving as one focus for development and evaluation. This physical science research will be coordinated with ongoing social science assessments designed to identify current and possible future uses of climate information and forecasts, and to clarify the relationships between climate, society and ecosystems in this highly climate-sensitive region. The initial stages of this research have been funded through the OGP regional

assessments program as a joint project between CDC and CIRES. CDC will also participate in and assist other regional assessment projects, as well as the International Research Institute for Climate Predictions (IRI), to fully exploit our climate diagnostic expertise in addressing other fundamental regional climate problems.

• *Increasing CDC research on the connections between short-term climate variability and decadal-to-centennial variability and change.*

One of the critical issues facing society is understanding, and potentially predicting, the links between short-term and long-term climate variability and change. The issue is paramount if we are to minimize the possibility of "climate surprises" as well as identify potential impacts of longer-term climate variability on ecosystems and society. Toward this end, CDC has been redirecting some of its resources toward longer-term climate issues, and is also establishing stronger linkages with GFDL (and other climate modeling institutions) to clarify mechanisms for longer-term climate variability and change. Increasing emphasis in this area is likely to continue over the next several years.

Linkages

The above issues are not independent, and we envision considerable coordination among activities. Likely foci will include the western U.S. as a testbed for evaluating climate forecasts and other experimental regional climate products, and the Pacific sector as a major focus region for evaluating mechanisms for producing climate variability, particularly coupled atmosphere-ocean and tropical-extratropical interactions. Such efforts will also enable coordination with other research programs that are planned in these areas over the next decade under the auspices of programs such as CLIVAR and GEWEX.

In addition to the above areas, over the next 5-10 years CDC envisions opportunities to expand its research to help contribute toward addressing several problems of major societal importance. Much of this work is fundamentally interdisciplinary in nature, and will require collaborations with other research organizations within and outside NOAA. Examples include climate and air quality, climate and human health, and climate effects on ecosystems, including marine resource management in support of NOAA's fundamental environmental stewardship mission. Pilot efforts in some of these areas are already underway.

CHAPTER 2

Modeling Research on Seasonal to Interannual Variability

The discovery in the 1980s of a significant extratropical impact of the tropical Pacific ENSO phenomenon, and the demonstration that several elements of the phenomenon could be predicted two or more seasons in advance using relatively simple models, were important developments in climate research. They rekindled interest in gaining a better understanding of ENSO dynamics, in the hope of making even better predictions. They also raised hopes that at least some aspects of interannual variability might be similarly predictable in other parts of the globe, not only from ENSO's remote impact but also through possibly predictable slow variations in other ocean basins. International research programs such as TOGA and CLIVAR were launched in pursuit of these hopes. Largely from their impetus, the observing system in the tropical Pacific was vastly improved, global gridded observational datasets spanning several decades were generated through various 'reanalysis' efforts, and extensive numerical simulations and predictions of interannual climate variations were undertaken with both uncoupled and coupled global climate models. Our understanding of the variability and predictability of the climate system on this time scale has matured considerably as a result. CDC has contributed significantly to the present store of knowledge in this area, and is at the forefront in addressing many of the remaining questions.

*CDC scientists have provided important evidence that the **predictable** evolution of ENSO and of the associated remote teleconnections are governed largely by **linear, low-dimensional** dynamics. This may be one reason why simple empirical linear models remain competitive with sophisticated GCMs at making seasonal predictions. Indeed the question of how much extratropical predictability exists on this scale beyond that associated with simple linear ENSO signals has become a recurring theme in CDC research. In the last four years, we have identified the situations in which the dynamics of ENSO are significantly nonlinear, clarified the extent to which the remote impacts can be nonlinear, and explored the extent to which those impacts might be sensitive to the details of the tropical SST anomaly patterns, i.e. be "higher-dimensional". We have also explored how the nonlinear and higher-dimensional dynamics might affect the tails of the probability distributions of atmospheric variables on synoptic, intraseasonal, and seasonal scales, and thus the risk of extreme anomalies on those scales. We have investigated the predictability of SSTs in other oceans basins, both through "atmospheric bridge" ENSO teleconnections and through the year-long persistence and subsequent re-emergence of SST anomalies from below the seasonally-varying surface mixed layer. We have also continued to assess the impact of such SSTs on the atmospheric circulation.*

2.1 Understanding and predicting seasonal tropical SST variations

CDC scientists have pioneered the development of Linear Inverse Modeling (LIM) as a diagnostic and forecasting tool. LIM is a method of extracting the dynamical parameters of a system from data. The assumption is made that the dynamics can be modeled as a stable linear multivariate process driven by geographically coherent white noise. The estimated dynamical parameters can then be used to make forecasts of the system. Real-time seasonal LIM forecasts of tropical Indo-Pacific SST anomalies are published monthly in the *Climate Diagnostics Bulletin* and quarterly in the

Experimental Long-Lead Forecast Bulletin (ELLFB). They are also available through CDC's website at http://www.cdc.noaa.gov/~lem/IndoPacific.frcst.html.

An important original result from our LIM diagnosis of Indo-Pacific SST variability was the identification, through a singular-vector analysis of the empirically-determined system propagator, of an *optimal initial SST pattern* for SST anomaly growth over 7 months in the basin. This structure evolves in 7 months into a pattern resembling a mature ENSO event (**Fig. 2.1**), and may therefore be viewed as a dynamically relevant precursor to ENSO. And indeed, as **Fig. 2.2**. shows, whenever an SST anomaly pattern projects appreciably on this structure, there is a good chance of obtaining large SST anomalies in the Niño 3.4 area 7 months later. **Figure 2.2** also shows that the projection statistics are similar whether they are evaluated for a time period including the training period (COADS data: 1950–1990) or for independent data (NMC Real-time Surface Marine data: 1991–2001). Encouraged by this robust behavior, we now provide real-time monitoring of the projection of the SST anomaly field on this structure through our website at http://www.cdc.noaa.gov/~lem/opt/optstr.html.

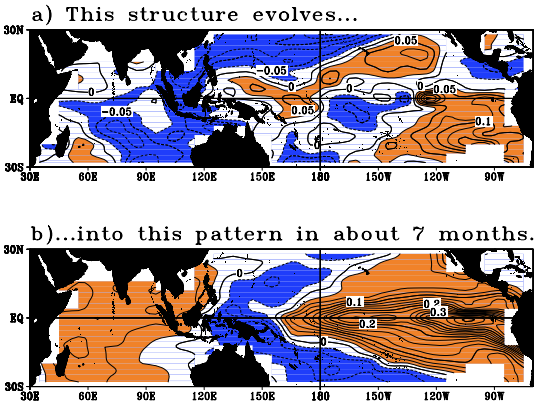

Fig. 2.1 (a) The optimal initial structure for SST anomaly growth. The pattern is normalized to unity. The contour interval is 0.025. Loadings greater than 0.025 are colored red; dashed lines indicate negative contours. **(b)** The pattern predicted when the pattern in (a) is used as the initial condition.

We have also recently published procedures for estimating improved confidence intervals on our SST forecasts. Until recently, the confidence intervals were those appropriate to our assumed stationary linear Markov process; that is, they showed the expected forecast error of a stable linear model driven by stationary white noise. The improved error bars also include estimated contributions from our neglect of the seasonal variation of the stochastic forcing, from estimating the model's parameters in a training period of finite length, and from initial condition errors.

The actual forecast error normalized by the rms of the total expected error estimated in this manner (**Fig. 2.3**) shows how much better the forecast skill is during La Niña than El Niño. This is consistent with our conclusion, stated in several papers, that nonlinear dynamics become important during the warmest phase of warm events. We have continued to investigate the failure of LIM during such periods. Although the lack of skill is mostly due to the greater importance of nonlinearity, an interesting recent finding was that LIM would nevertheless have been useful during late 1994–early 1995 had it been applied to *weekly* instead of seasonal SSTs. Evidence has also been found that unpredictable sto-

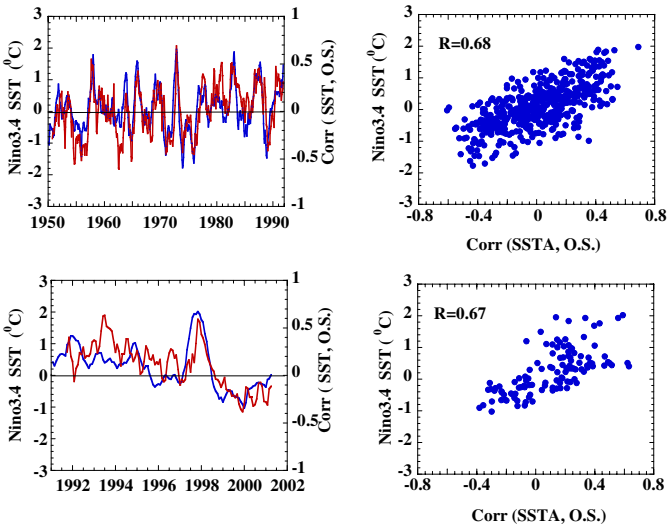

Fig. 2.2 Left panels: Time series of SST anomaly in Niño 3.4 (blue line), and the pattern correlation of the SST anomaly pattern seven months earlier with the optimal structure (red line). The information in these left panels is also displayed in the form of scatter plots in the right panels.

chastic forcing accounted for a large portion of the observed warming during the strong 1997–1998 event.

CDC also provides LIM forecasts of the tropical north Atlantic and Caribbean SSTs in the *ELLFB*. Again, these forecasts are available through our website at http://www.cdc.noaa.gov/~lem/Atlantic.forecast.html. We have shown that forecast skill in these Atlantic regions is related to the skill of predicting El Niño. We have also used LIM to diagnose the dynamical nature of tropical Atlantic SST variability, and published evidence that the familiar "dipole" SST anomaly pattern is a dynamically realizable structure (as opposed to merely the dominant EOF of regional SST variability), but whose development is often interrupted by ENSO influences from the east Pacific.

Our original claim that the basic dynamics of ENSO are stable, linear and stochastically forced has been independently confirmed by others and is gradually forcing a paradigm shift in this field. We have continued investigating

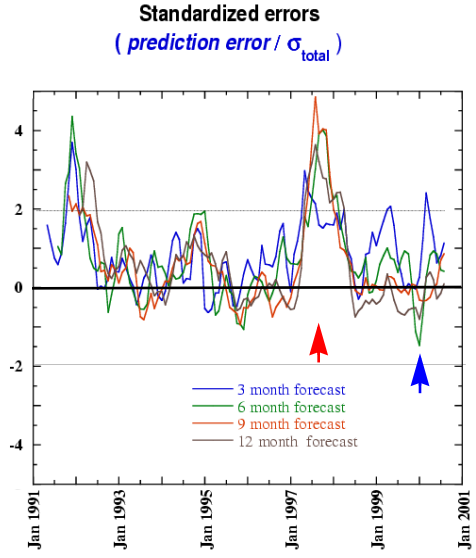

Fig. 2.3 Time series of actual LIM forecast errors normalized by one standard deviation of the total forecast uncertainty. The horizontal lines at ± 1.96 indicate the 95% confidence interval. The red and blue arrows indicate prominent El Niño and La Niña events during this period.

the dynamical nature of ENSO, especially in collaboration with scientists at Texas A&M University. A recently published study showed that an intermediate coupled ENSO-prediction model of the Cane-Zebiak type, tuned to be in a stable stochastically forced regime, generated more realistic SST variability than did the same model tuned to give self-sustained oscillations.

2.2 Understanding and predicting the global impact of tropical SST variations

CDC scientists are using a combination of observational and general circulation modeling approaches to address this problem. The observational studies rely heavily on the 50-year NCEP reanalysis dataset. The GCM studies are conducted by running various versions of the NCEP and GFDL global atmospheric models with prescribed SST forcing, in some cases by coupling to a mixed layer in parts of the world ocean. We have also analyzed 10–12 member ensembles of 50-year runs made by several GCM groups (NCEP, GFDL, NCAR, ECHAM, IRI) with prescribed observed SST forcing, generally for the period 1950–1995, prescribed either globally or in the tropics.

2.2.1 Prediction skill and predictability

Outside the tropics, SST-forced signals account for a relatively small (generally less than 25%) portion of extratropical variability on seasonal to interannual scales. This fundamentally limits the average skill of a deterministic (as opposed to a probabilistic) seasonal forecast, regardless of whether it represents the mean of a large forecast ensemble or even a multi-model ensemble. The limitation arises from a generally small signal-to-noise ratio, and cannot be overcome by improving models. The noise is associated with chaotic (i.e., unpredictable) nonlinear interactions and is intrinsic to the extratropical atmosphere. Still, in extreme individual cases, the signal can exceed the noise, making relatively skillful forecasts possible.

There are two other confounding factors that make it difficult for even sophisticated GCMs to improve upon the forecast skill of simple statistical models based on linear correlations between tropical SST and extratropical circulation anomalies. The first is the approximate linearity of the remote response to ENSO. The other is the relative *insensitivity* of that response to details of the tropical SST forcing; it appears that knowledge of the area-averaged anomaly in Niño-3.4 alone is almost enough.

Figure 2.4 provides a good illustration of these points. It shows the correlation of observed JFM-mean 200 mb geopotential height anomalies with those predicted, over a 26-year period, using two forecasting systems of vastly different complexity. The top panel shows the skill of a 9-member ensemble-mean forecast by the NCEP atmospheric GCM forced with observed concurrent SST anomalies in the tropical Pacific between 20°N and 20°S. Consistent with many studies, the correlation of the observed and predicted height anomalies is high in the tropics, and appreciable over North America and the northeast and southeast Pacific

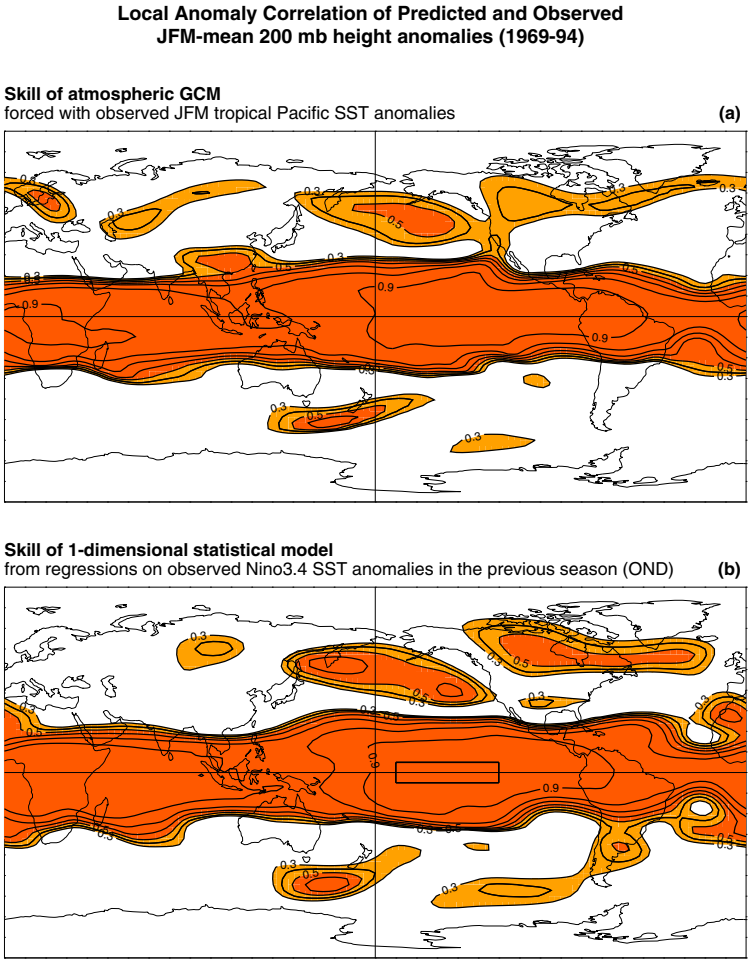

Fig. 2.4. Wintertime 200 mb height seasonal forecast skill of (a) the NCEP atmospheric GCM with specified observed SSTs in the tropical Pacific basin and (b) a simple linear regression model based on seasonal 200 mb height correlations with Niño 3.4 SSTs. See text for details.

oceans. This is encouraging, although it should be noted that the GCM forecasts are not true forecasts. Still, they give an idea of the potential predictability of seasonal anomalies around the globe if the tropical Pacific SSTs were to be predicted accurately. The surprise in **Fig. 2.4** is the lower panel. It shows the skill of the simplest conceivable linear regression forecasts for the same cases as in the upper panel, using the regression coefficients of observed JFM 200 mb height anomalies against the area-averaged observed JFM SST anomaly in Niño-3.4. The forecasts themselves are made using the observed Niño-3.4 SST anomaly in the *previous* 3-month period (OND) as the predictor. These simple forecasts are clearly comparable in skill to the GCM forecasts. They also represent legitimate 1-season 'coupled model' forecasts, in that they incorporate a trivial persistence forecast of the Niño-3.4 SST anomalies from OND to JFM.

The rough agreement between the two panels in **Fig. 2.4** may be interpreted as reflecting either true seasonal predictability limits or the need for further GCM improvement. There is room for both interpretations, although we are more inclined toward the former. GCM error is probably not the main culprit here: several other GCMs analyzed by us yield skill patterns very similar to that in the upper panel. Also, when the NCEP GCM is asked to predict its own behavior, such as when using an 8-member ensemble-mean to predict the 9th member's seasonal anomalies, its skill is again similar to that in the upper panel. One can thus make a case that the modest extratropical values in **Fig. 2.4** are mainly a reflection of the limited intrinsic predictability of extratropical seasonal averages associated with tropical SST forcing. As mentioned earlier, this in turn is mainly due to a modest signal-to-noise ratio.

CDC scientists have attempted to clarify the relationship between the expected anomaly correlation skill ρ of ensemble-mean forecasts and the signal-to-noise ratio *s*, defined as the ratio of the ensemble-mean anomaly to the ensemble spread. **Figure 2.5** summarizes this general relationship, which is useful in interpreting many GCM results. The ρ_∞ and ρ_1 curves show the expected skill of infinite-member and single-member ensemble-mean forecasts with a perfect model. The third (blue) curve depicts the expected skill of infinite-member ensemble-mean forecasts with an imperfect model, whose systematic error s_e (i.e., its error in determining the true *s*) is of the same magnitude as *s*. Note that these curves are applicable to any forecast variable, in any forecasting situation, and to any forecasting method, including the regression method used in **Fig. 2.4b**.

The ρ_∞ curve represents a hard predictability limit with a perfect model, and shows that to produce 'useful' forecasts with anomaly correlations greater than 0.6, *s* needs to be greater than 0.75. To produce 'excellent' forecasts with anomaly correlations greater than 0.9, *s* needs to be greater than 2. Given the evidence from several studies that *s* for ENSO-related 200 mb seasonal height anomalies is approximately between 0.5 and 1 in the extratropical Pacific-American sectors of both hemispheres, and greater than 2 in the tropics, the results in **Fig. 2.4** are not surprising. **Figure 2.5** is also useful for assessing to what extent the modest skill in **Fig. 2.4a** might be due to model error or using only 9-member ensembles. The difference between ρ_∞

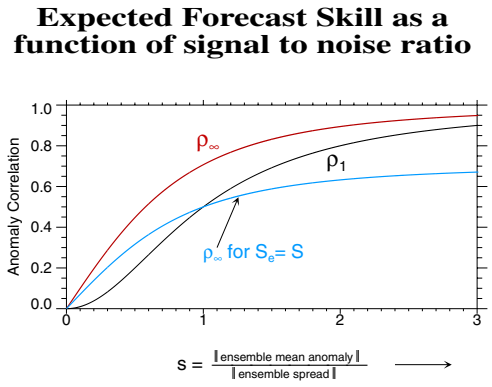

Fig. 2.5 Expected anomaly correlation forecast skill of ensemble-mean forecasts as a function of signal to noise ratio *s*. The red curve is the expected skill of an infinite-member forecast, the black curve the expected skill of a single-member forecast. The blue curve shows the expected skill of an infinite-member ensemble forecast using an imperfect model whose standardized systematic error is of the same magnitude as *s*.

and ρ_1 shows the potential gain in skill by using infinite-member ensembles instead of a single member. The maximum gain is 0.25, for $s \sim 0.6$. However, most of this gain is attainable with about 25 members, and even a ρ_9 curve (not shown) is close to the ρ_∞ curve. The loss of skill due to model error (blue curve) is probably of greater concern in **Fig. 2.4a** than not having enough members. However, model error could equally be affecting skill in **Fig. 2.4b**.

2.2.2 New research challenges

Figures 2.4 and **2.5** together suggest that the modest skill, on average, of deterministic extratropical seasonal forecasts is largely consistent with the predictability limits imposed by the modest local values of *s* associated with the tropically forced signal. Given also the evidence in **Fig. 2.4b** that similar skill can also be achieved with simple linear regression models, the question naturally arises as to what further useful predictive information can be extracted by running GCM ensembles.

CDC scientists have spent considerable time pondering this issue, and have come up with several encouraging possibilities. In one way or another, they all involve focusing on the distributional aspects of the ENSO response rather than on the ensemble-mean. For example, as **Fig. 2.6a** shows, a modest shift in the mean of 0.5 (in units of standard deviation), while not large enough to affect appreciably the expected seasonal mean of an extratropical variable, can still greatly affect the probability of its extreme values. The risk of obtaining an extreme positive value of greater than +1 increases from 16% to 31%, and the risk of obtaining an extreme negative value decreases from 16% to 7%. Thus without ENSO the risks of extreme positive and negative anomalies are the same, but with ENSO, even for a modest *s* of 0.5, the risk of an extreme positive anomaly becomes 4.4 (=31/7) times the risk of an extreme negative anomaly. **Figure 2.6b** shows how this risk ratio can be equally strongly affected by modest changes of noise. In this example, a 20% reduction of standard deviation combined with a mean

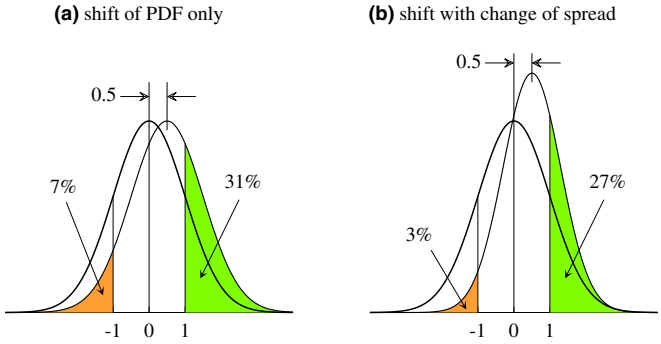

Fig. 2.6. (a) An illustration of how a mean shift of 0.5 of a normal distribution increases the probability of extreme positive values from 16% to 31% and decreases the probability of extreme negative values from 16% to 7%. **(b)** Illustration of the altered probabilities of extreme values when the mean shift of 0.5 is also accompanied by a reduction of the standard deviation from 1 to 0.8.

shift of 0.5 changes the risk ratio from 1 (=16/16) to 9 (=27/3).

When even minor PDF shifts and changes of variance imply large changes in the risks of extremes values, determining them accurately becomes important. It is easy to see how a good GCM might have an advantage over the regression model of **Fig. 2.4b** in this regard, whose parameters cannot be estimated accurately enough from the limited observational record to have confidence in its predictions of extreme values. Further, one can run as many GCM ensemble members as necessary in individual forecast cases to predict the changes of extreme risks within specified confidence intervals. The regression-model also assumes, in effect, that ENSO-induced mean PDF shifts are strictly linear with respect to the SST forcing and that there are no changes of noise, or variability. CDC scientists have spent considerable effort on ascertaining the extent to which such assumptions are valid, since they have a large bearing on the problem at hand.

2.2.3 Understanding the sensitivity of the atmospheric response to details of the anomalous SST forcing

The regression-model used in **Fig. 2.4b** always predicts the same signal pattern of the global atmospheric response; only its amplitude varies from forecast case to case in direct proportion to the strength of the Niño 3.4 SST anomaly. As we have seen, this doesn't seem to affect its deterministic forecast skill overmuch, but the question is whether it limits predictions of the risk of extreme anomalies. To what extent does the remote SST-forced signal vary from case to case? To what extent are its variations determined by the nonlinearity of the response to the amplitude and sign of the SST forcing in Niño 3.4, and to what extent by the details of the SST anomaly pattern in the wider tropical Indo-Pacific domain? We have conducted several studies to answer these questions.

Figure 2.7 gives a sense of the signal variation from case to case. Sampling uncertainty is an issue in this problem, given that the number of samples required to establish that s is statistically different from zero is inversely proportional to the *square* of s. At the 5% level, the number of samples should be greater than $8/s^2$. To establish the significance of $s = 0.5$ thus requires 32 samples; to establish the significance of *changes* of s from case to case, say of order 0.25, would require many more, 128. With this in mind, we ran a very large 180-member seasonal ensemble with the NCEP atmospheric GCM with prescribed observed global SST forcing corresponding to the El Niño of 1987, and another 180-member ensemble for the La Niña of 1989. The right-hand panels of **Fig. 2.7** show the ensemble-mean 500-mb height anomalies obtained in these integrations (defined with respect to the ensemble-mean obtained in another set of 180 integrations with climatological-mean SST forcing). To our knowledge this is the most statistically confident determination of the global SST-forced signal ever made for two different observed SST forcing patterns. Note that the sign of the response has been reversed in the lower panel for easier comparison with the

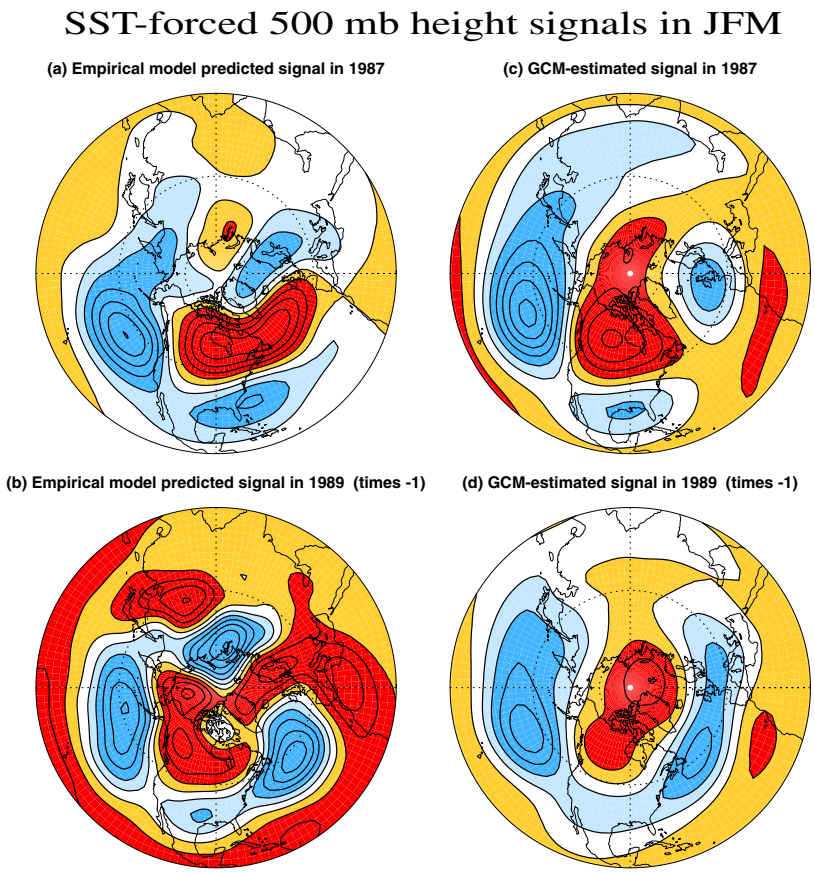

Fig. 2.7 The SST-forced signal in 500 mb heights during the El Niño winter of JFM 1987 (top panels) and the La Niña winter of JFM 1989 (bottom panels, with sign reversed) estimated by a GCM (right panels) and an empirical method (left panels). The right panels show the ensemble-mean anomaly fields obtained in 180 seasonal integrations of the NCEP AGCM with prescribed global SST forcing during JFM 1987 and JFM 1989. The left panels show scaled historical composite 500 mb anomaly fields derived from 10 observed El Niño and 10 observed La Niña events in the 1958–1999 period, defined with respect to a Niño 3.4 SST anomaly index. The composite patterns were scaled by factors of 0.73 and 1.36 to account for the moderate Niño 3.4 index magnitude during 1987 and the larger magnitude during 1989, respectively. The contour interval is 10 m in all panels. Positive values are indicated by red and negative by blue shading.

upper panel. For comparison we also show in the left panels, in an identical format, observational 500-mb composite anomaly patterns for 10 El Niño and 10 La Niña events based on the Niño 3.4 index, and defined with respect to 10 "neutral" events. Note that the *amplitudes* of these composite patterns have been scaled by 0.73 and 1.36, in proportion to the observed Niño 3.4 SST anomaly magnitudes during the moderate 1987 El Niño and the strong 1989 La Niña events, respectively. Thus these left panels may be interpreted as the SST-forced 500-mb height signals during 1987 and 1989 as predicted by an empirical method. This method is superior, in principle, to that used in **Fig. 2.4b** in that it predicts different response patterns in

El Niño and La Niña cases, as shown here.

Although the GCM's signal patterns for these individual El Niño and La Niña winters are generally similar to one another, there are some notable differences. The El Niño response is stronger in the PNA sector, despite the weaker SST forcing. This is also true in the empirical forecast. There is little else to compare between the GCM and empirical forecasts because of sampling uncertainty in the empirical forecasts, i.e., the fact that the left panels are derived from only 10 cases each in the historical record. In areas such as the North Atlantic where the left panels predict a strong asymmetric signal of the same sign in 1987 and 1989, the significance of that asymmetry is therefore questionable. The differences between the GCM's predicted signal patterns for 1987 and 1989 are much more reliable in this regard, and though more modest, are large enough that they would have had important implications for predicting the risks of extreme anomalies during these winters.

There is thus evidence of significant signal variation from case to case. To put these results on a stronger footing, one might ideally wish to generate similar 180-member ensembles for each one of the past 50 or so winters. This has not yet been done. However, results from a 46-member multi-model ensemble of four different atmospheric GCMs (NCAR CCM3, NCEP, GFDL, and ECHAM) offer additional evidence of the existence of different response patterns. Between 10 and 12 member ensembles were gen-

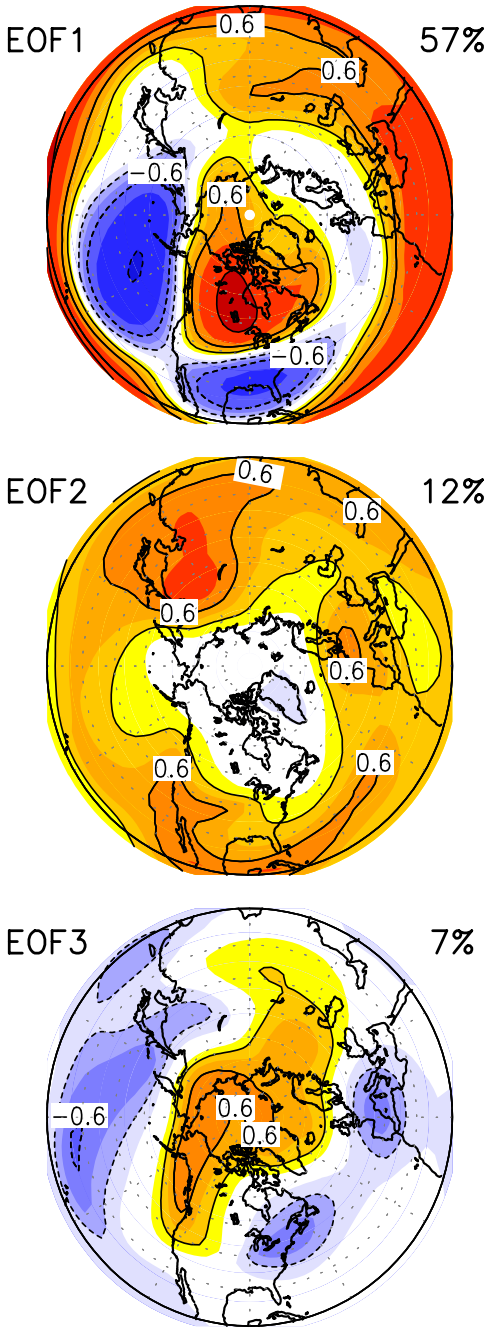

Fig. 2.8 The first three EOFs of SST-forced 500 mb height signals in a multi-GCM ensemble of 50-year integrations made with prescribed evolving observed global SST boundary conditions. See text for further details. The values plotted are the correlations of the EOF's Principal Component time series with the local 500 mb height time series of the SST-forced signal. Positive values are indicated by red and negative by blue shading.

erated for each model forced with identical evolving observed global SSTs over the past 50 years. For each one of the 50 winters, the SST-forced signal at 500 mb was defined as a weighted average of the ensemble-mean responses of the 4 GCMs. Finally, an EOF analysis of these 50 signal patterns was performed. **Figure 2.8** shows the first three EOFs, together with their fractions of the total signal variance explained. The leading EOF alone accounts for 57% of the global signal variance, and as much as 80% over the PNA region. Most elements of this pattern are evident in all the four panels of **Fig. 2.7**. The dominance of this signal pattern, its strong similarity to the classic observed ENSO teleconnection pattern, and also to the unchanging forecast pattern of the regression model used in **Fig. 2.4b**, explains why the upper and lower panels of **Fig. 2.4** are so similar. Still, there is evidence in **Fig. 2.8** of apparently minor but potentially important deviations from this dominant signal pattern from winter to winter. The second EOF is largely zonally symmetric, with out-of-phase anomalies in polar and subtropical latitudes. Locally, it explains a substantial fraction of the signal variability in the subtropics, and its associated Principal Component (PC) time series describes a tropospheric warming trend of lower latitudes over 1950–1999 associated with a long-term tropical SST warming trend. The third EOF resembles a tropically forced wavetrain with centers spatially shifted relative to those of the leading EOF. Its PC time series regressed on the simulated tropical precipitation fields yields a regression map with appreciable magnitudes in the western and central equatorial Pacific. This third EOF may thus reflect a genuine sensitivity of the SST-forced extratropical signal to variations of the anomalous tropical SST pattern from winter to winter.

It should be stressed that the GCM results in **Figs. 2.7** and **2.8** are all for global SST forcing. To what extent can the signal variation evident in these figures be attributed strictly to the *tropical Pacific* SST forcing, in particular to asymmetric responses to El Niño and La Niña forcing? There is a strong suggestion of a weaker response to La Niña forcing in the lower panels of **Fig. 2.7**. Such a weaker response (not shown) is also clearly evident in the composite El Niño and La Niña signals in the 4 different ensemble GCM simulations for 1950–1995 described above. Are there also significant differences in the *patterns* of the response? To what extent do they contribute to the third EOF in **Fig. 2.8**? Several CDC studies have attempted to address such questions cleanly, by examining the atmospheric response to the first EOF pattern of tropical Pacific SST (very similar to the Pacific portion of the lower panel of **Fig. 2.1**) with positive ("El Niño") and negative ("La Niña") signs. A weaker response to the negative EOF forcing has indeed been confirmed, but is appreciable only for large amplitude forcing.

Figure 2.9 shows results from a GCM experiment designed specifically to address this issue. A 9-member NCEP GCM ensemble was generated for 1963–1989 by forcing throughout the 27 years with the first SST EOF pattern, varying

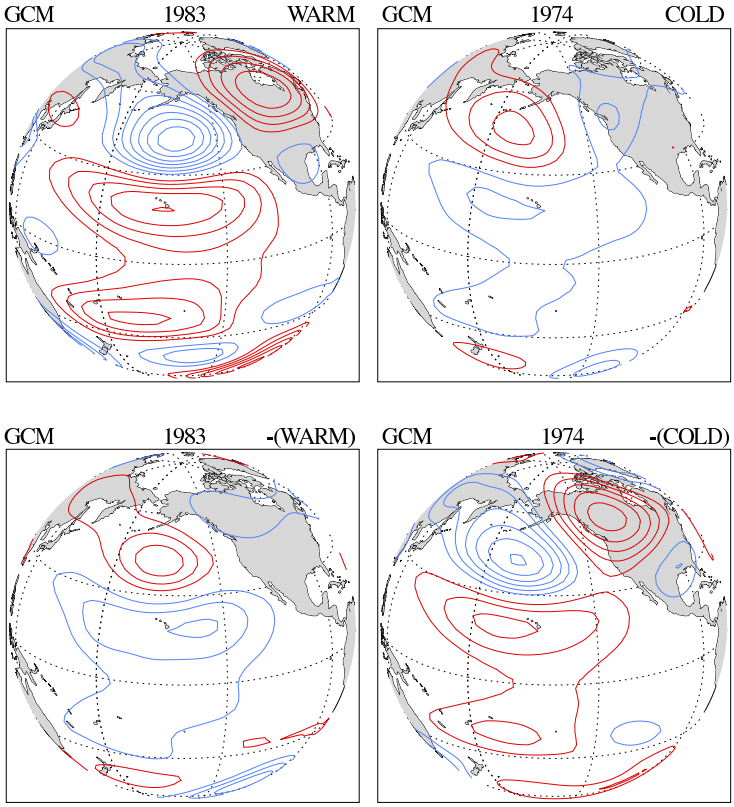

Fig. 2.9 GCM 200 mb height responses in northern winter (DJF) to the first EOF pattern of tropical Pacific SST forcing, with the observed amplitude during DJF 1982/83 (upper left panel), the observed amplitude during DJF 1973/74 (upper right), the negative of the observed amplitude during DJF 1982/83 (lower left), and the negative of the observed amplitude during DJF 1973/74 (lower right). The contour interval is 10 m. Positive values are indicated by red and negative by blue contours. See text for further details.

in magnitude and sign as its associated PC time series. The upper panels of **Fig. 2.9** show the ensemble-mean responses during the strongest warm and cold winters of 1983 and 1974, respectively, in this period. The response is clearly weaker for the 1974 event. This is suggestive but not conclusive, since the magnitude of the SST forcing was also weaker in 1974. To settle this, the entire experiment was repeated with the sign of the PC time series reversed. The ensemble-mean responses for the sign-reversed 1983 and 1974 winters are shown in the lower panels. The 1974 response is now stronger than the 1983 response, despite the weaker magnitude forcing. We had noted this effect earlier in **Fig. 2.7**, but the result here is cleaner. It confirms that the remote atmospheric response to the tropical Pacific SST forcing is appreciably stronger for strong warm than for the strong cold SST forcing. A top-to-bottom comparison in **Fig. 2.9** compares the responses to the same SST forcing but of

opposite sign, and further confirms this result.

2.2.4 ENSO-induced changes of variability

To what extent does ENSO affect the atmospheric noise (i.e., the variability) as hypothesized in **Fig. 2.6b**? We have addressed this issue in several recent publications. In one study, we examined the standard deviation of seasonal-mean 500 mb heights in our 180-member GCM ensembles for the winters of 1987 and 1989, and found a modest overall increase in the warm (1987) and a decrease in the cold (1989) ensemble compared to that in the neutral 180-member ensemble. This was speculated to be forced partly by the increased variability of seasonal precipitation in the warm (and decreased variability in the cold) ensemble in the Niño-4 area of the central equatorial Pacific, which has been shown to be sensitive region for forcing a large global circulation response. Another study searched for ENSO-induced changes of seasonal noise in the smaller AMIP-style GCM ensembles used in **Fig. 2.8**, but found little impact in the PNA region. While these findings seem to conflict, a closer look at the published figures shows that the results are not inconsistent in the PNA region. To the extent that the altered extratropical noise is due to the tropical precipitation noise, the effect is also probably both GCM-dependent and ENSO event-dependent. It should be mentioned that sampling uncertainty is of even greater concern here than in **Figs. 2.7** and **2.8**. The number of samples required to establish the significance at the 5% level of a fractional change Δ of an ensemble's standard deviation is close to $3/\Delta^2$. To establish the significance of the Δ of 0.2 (corresponding to a 20% change of standard deviation) in **Fig. 2.6b** would thus require 75 samples from both the neutral and altered distributions. Any change of smaller than 17.5% would require more than 100 samples.

The effect of ENSO on *subseasonal* extratropical variability is equally important, and somewhat easier to establish. These effects can be distinct from the effects on seasonal mean quantities, and can have important practical implications. For instance, one may imagine a situation in which El Niño alters the occurrence of both cold waves and warm spells in a winter. The effect is a meaningful change in the risk of extreme weather, even though little seasonal mean signal might be evident. The few published studies on this topic, constrained either by sampling requirements or data availability, have formed composites over several ENSO events to diagnose the effect in limited regions. In an ambitious recent study, we have estimated the effect globally from our large AGCM ensembles for 1987 and 1989, and compared them with observational composites based on 11 El Niño and 11 La Niña events in the recent record. As in **Fig. 2.7**, the purpose of this comparison was to gauge to robustness of the changes of variability, their predictability, and their variation from event to event.

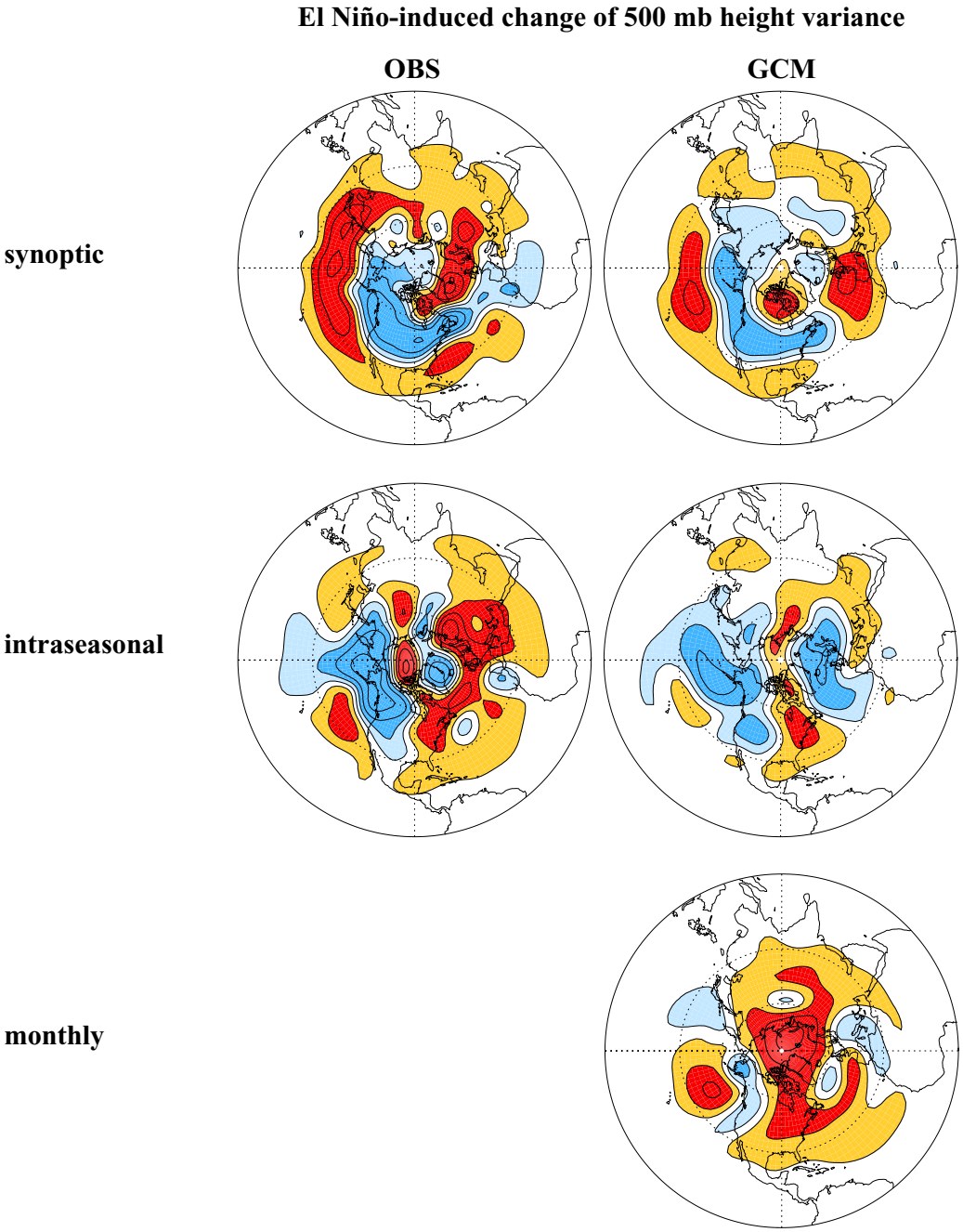

Fig. 2.10 El Niño-induced changes of variance on three different subseasonal time scales. The quantity plotted is the square root of the anomalous variance, with red shading for positive and blue for negative anomalous variance. The left panels are based on statistics averaged over 11 observed El Niño and 11 observed "neutral" JFM winters in the NCEP reanalysis dataset. The right panels are derived from a large AGCM ensemble with observed SST forcing for the El Niño winter of JFM 1987. Top panels: Synoptic scale (2 to 6 day periods), Middle panels: Intraseasonal scale (8 to 45 day periods.). Bottom panel: Monthly scale (30-day averages). Contours are drawn at 8 m intervals starting at 4 m in the top panels, and at 16 m intervals starting at 8 m in the middle and lower panels. See text for a fuller explanation.

The most important result from this analysis, depicted in **Fig. 2.10**, is that the patterns of the SST-forced anomalous height variability are markedly different for the synoptic (2 to 7 days), intraseasonal (8 to 45 days), and monthly (30 -day average) time scales. In contrast, the patterns of the anomalous tropical rainfall variability (not shown) are nearly identical across these time scales. **Figure 2.10** shows contours of Δ_σ , defined as the signed square root of the anomalous variance difference of 500 mb heights on these time scales (where by "signed" we mean that if the anomaly is negative, we depict its square root with a minus sign). The results for La Niña (not shown) are similar and generally of opposite sign. The comparison between the GCM and observational panels in **Fig. 2.10** is not clean. Nevertheless, their gross similarity is reassuring, both for the robustness of the changes of variability and this GCM's ability to simulate them. To that extent, their dissimilarity can be attributed to the comparison not being clean (i.e., event-to-event differences) and sampling error, especially in the observations (which is why the observational anomalous monthly variability map has been omitted).

The main ENSO effect on the synoptic scale is a southward shift of the storm track over the Pacific ocean and North America. On the intraseasonal scale, it is a decrease of height variance over the north Pacific, consistent with a tendency of reduced blocking activity during El Niño. On monthly (and seasonal) scales there is a suggestion of an overall increase of variance. Referring back to **Fig. 2.6b**, it is evident that these differing ENSO impacts on extratropical noise on different time scales have very different implications for the risks of extreme anomalies on these scales. We believe that three quite distinct dynamical mechanisms are responsible for these sharp differences, and are currently investigating them in a hierarchy of dynamical models.

2.3 Understanding the impact of extratropical SST variations

Despite many studies, the precise role of extratropical SST variations in the dynamics of atmospheric low-frequency variability remains unclear. Many atmospheric GCM experiments have been performed with prescribed extratropical SST anomalies to determine the atmospheric response to them. The results have been variable and confusing, not only because the response is weak and difficult to establish in short integrations, but also because it is sensitive to the precise location of the prescribed SST anomaly in relation to the atmospheric jet streams and their associated storm tracks. The largest extratropical SST anomalies tend to occur near the jets, and may be thought of as having a direct effect on the mean flow, and on the storm tracks through the change in the mean flow. The altered storm tracks can, however, feed back on the mean flow. This indirect effect can be very important, but is difficult for GCMs to represent accurately.

We have investigated these issues in a series of long NCEP AGCM runs with

prescribed extratropical SST forcing. In a previously published study, an idealized warm SST anomaly was imposed near the Kuroshio region of the northwest Pacific. The atmospheric response to this was radically different in perpetual January and perpetual February integrations of the GCM: a baroclinic response in January and a nearly equivalent-barotropic ridge response in February. To understand this, we used a linear model to investigate the response to the SST anomaly as the sum of the direct heating-induced component and the indirect eddy-driven component associated with the altered storm tracks. (A novel feature of this calculation was that the altered storm-track forcing specified in the linear model was specifically that induced by the heating altered mean flow, diagnosed using Whitaker and Sardeshmukh's storm-track model). This diagnosis confirmed the dominance of the eddy-driven component, forced mainly by the altered eddy-momentum fluxes, in determining the barotropic ridge response. Without the eddy forcing, the response to a shallow heat source associated with the warm SST anomaly was always baroclinic, with a trough near the surface and a ridge aloft and downstream. This explains the baroclinic response to extratropical SST anomalies obtained in many low-resolution GCMs, in which the simulated storm tracks and eddy momentum-fluxes are generally too weak: in such GCMs the SST-induced alterations of the storm track are also too weak. An equivalent-barotropic ridge response develops only if the storm track is altered sufficiently strongly that strong anomalous eddy-forcing is generated at the correct locations to reinforce the heating-induced upper-level ridge and offset the lower-level trough. In this way, the atmospheric response becomes sensitive to the characteristics of the storm track and the position of the SST anomaly relative to the storm track.

As an example, **Fig. 2.11** shows the linear model results for idealized shallow heat sources associated with warm extratropical SST anomalies imposed on the

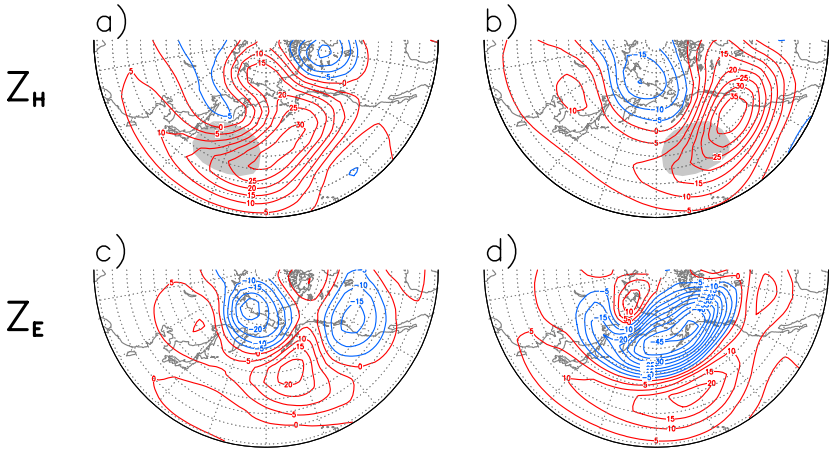

Fig. 2.11 A linear balance model's 250 mb geopotential height response in winter to a shallow elliptic heat source centered (a) at 40°N,160°E and (b) at 40°N,160°W. The model's height response to the anomalous eddy vorticity fluxes induced by these heat sources is shown in (c) and (d), respectively. The contour interval is 5 m; positive values are indicated by red and negative by blue contours.

observed winter-mean basic state. With an elliptic source specified over the western Pacific (left panels), the heating-induced upper-level ridge (upper panel) is reinforced by the eddy-driven equivalent-barotropic ridge (lower panel) over the Pacific, similar to the GCM's February response. No such reinforcement by the transients occurs for a similar source specified over the eastern Pacific (right panels).

2.4 Understanding and predicting SST variations outside the tropical Pacific

2.4.1 The atmospheric bridge

One example of global climate interaction is the "atmospheric bridge", where atmospheric teleconnections associated with ENSO drive anomalous ocean conditions outside of the equatorial Pacific through changes in the heat, momentum, and fresh water fluxes across the air-sea interface. The resulting SST anomalies can also feed back on the initial atmospheric response to ENSO. As part of the GFDL-Universities Consortium project, we developed a coupled AGCM-mixed layer ocean model and used it to conduct experiments to study the atmospheric bridge and other air-sea interaction processes. In the "MLM" experiment, observed SSTs were prescribed as boundary conditions in the tropical Pacific (15°N–15°S, 172°E–South American Coast), and the remainder of the global oceans were simulated using the variable-depth mixed-layer model. As **Fig. 2.12** shows, the simulated SLP and SST anomalies associated with ENSO are fairly realistic, with stronger cyclonic

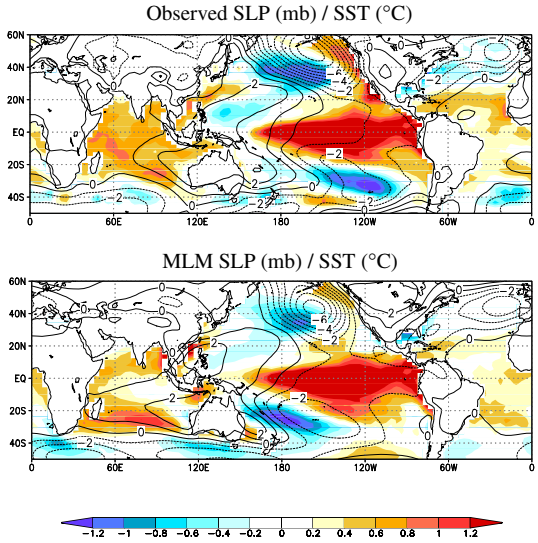

Fig. 2.12. (a) Observed and (b) simulated El Niño minus La Niña composite of SLP (contour interval of 1 mb) and SST (shading interval of 0.2 °C) for DJF(0/1), where 0 indicates the ENSO year and 1 the next year. The composite is based on 9 El Niño and 9 La Niña events during 1950–1999. The observed values are from the NCEP reanalyses and the model results from an average of 16 MLM integrations.

circulation and cold water over the central North and South Pacific and warm water along the west coast of the Americas. ENSO-induced changes in the Walker circulation also lead to warm SSTs in the north tropical Atlantic and Indian Oceans.

How useful is this effect in actually predicting the interannual variations of SSTs outside the tropical Pacific basin? **Figure 2.13** provides one measure of the forecast skill. It shows the correlation of the observed seasonal-mean SST anomalies, over the 50-year 1950–1999 period, with those predicted by the MLM model. The predicted field for each season represents a 16-member ensemble-mean. Results are shown separately for the 50 winter (JFM) and 50 summer (JAS) forecast

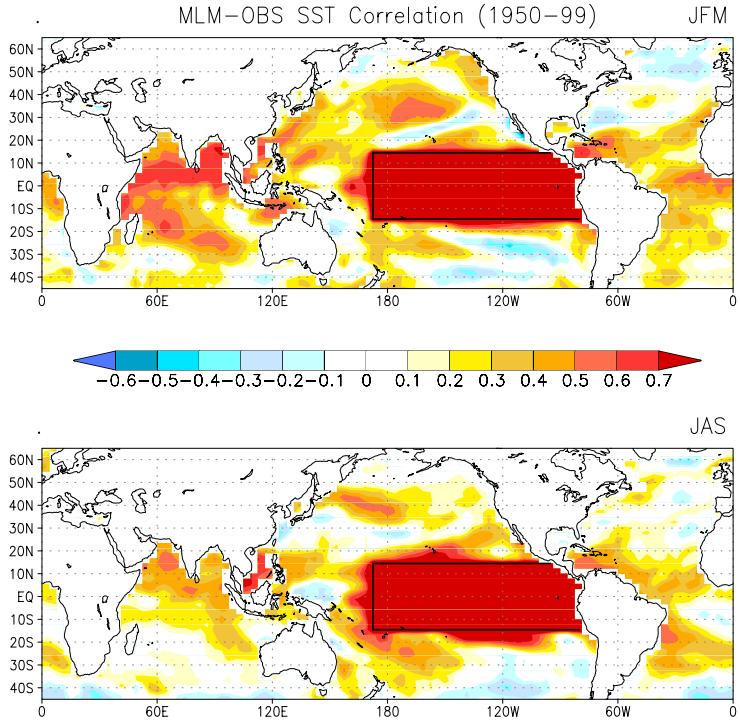

Fig. 2.13. Predictability of seasonal SST anomalies worldwide via the "atmospheric bridge" from the tropical Pacific ocean, in winter (top panel) and summer (bottom panel). Values plotted are the correlations of observed SST anomalies with those predicted by an atmosphere–mixed layer ocean coupled model with specified observed SSTs in the central and eastern tropical Pacific ocean. See text for further details.

cases over which the correlations were calculated. The correlations are generally higher than 0.4 in the central north and south Pacific oceans, and also in the tropical Indian and tropical Atlantic oceans. This is encouraging, and also sheds some light on why the LIM SST forecast models described in section 2.1, that are based solely on SST correlations between different tropical locations, perform as well as they do: the "bridge" effect is implicitly included in them. It is also interesting to compare **Fig. 2.13** with **Fig. 2.12** in areas such as the north Atlantic, where **Fig. 2.12** suggests a bridge effect but **Fig. 2.13** shows it to be unimportant.

2.4.2 The re-emergence of long-lived subsurface temperature anomalies

The atmospheric changes associated with ENSO influence upper-ocean processes that affect the subsurface temperature structure and mixed-layer depth (MLD) long after the ENSO signal decays. Thermal anomalies that form in the surface waters of the extratropics during winter partially reemerge in the following winter, after being sequestered beneath the mixed layer in the intervening summer. SST anomalies generated via the atmospheric bridge recur in the following winter in central North Pacific via this reemergence mechanism (**Fig. 2.14**). The MLD is substantially deeper in the cen-

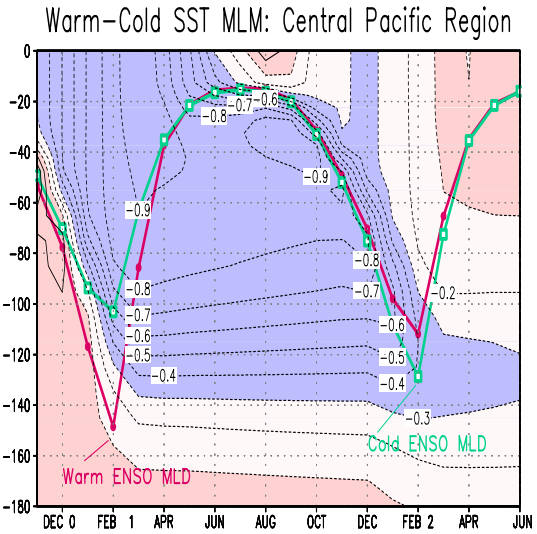

Fig. 2.14 The composite El Niño minus La Niña ocean temperature from Nov(0)–Jun(2) and the composite mixed layer depth (m) during El Niño (red line) and La Niña (blue line) from the MLM experiment in the central North Pacific (180°–160°W, 28°N–42°N).

tral North Pacific during El Niño than La Niña winters, but the reverse is true in the subsequent winter. During El Niño winters, enhanced buoyancy forcing (surface cooling) and mechanical mixing creates a colder and deeper mixed layer. After the MLD shoals in late spring, the cold water stored beneath the surface layer as part of the reemergence process increases the vertical stability of the water column, reducing the penetration of the mixed layer in the following fall and winter.

The reemergence process is not confined to the central North Pacific, nor does it occur solely in conjunction with the atmospheric bridge. **Figure 2.15** shows the evolution of the leading pattern of North Pacific SST variability in observations and in two distinct AGCM – ocean model experiments. In the first experiment, the mixed layer ocean model is active over the entire globe, including the tropical Pacific, and thus does *not* include ENSO. In the second experiment,

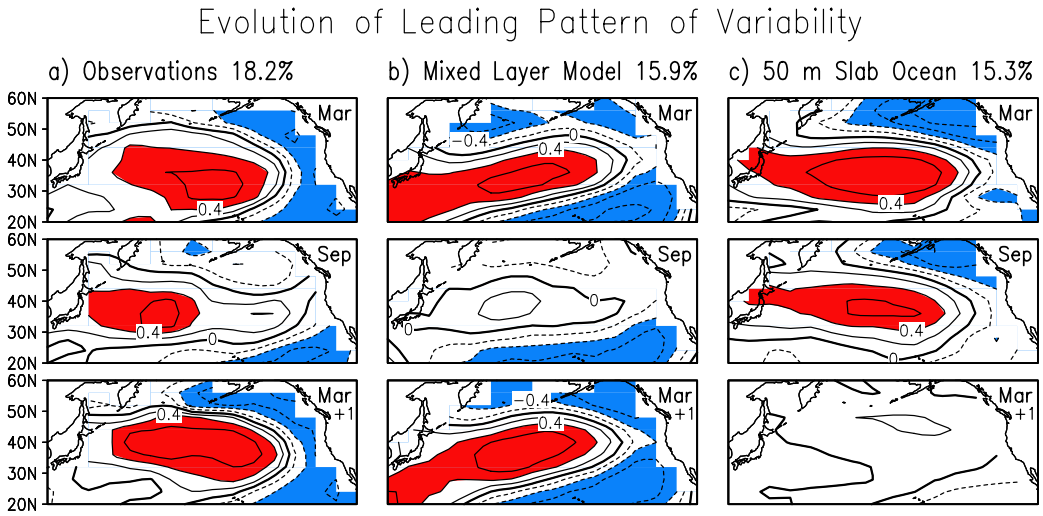

Fig. 2.15. The evolution of the leading pattern of SST variability over 20°N–60°N in the Pacific as indicated by extended EOF analyses of monthly SST anomalies from January through April of the following year. The results are presented as the correlation between the leading principal component (time series of EOF1) with SST anomalies at the individual grid points for March, September and March of the following year. (The other months, which are not shown, indicate a similar evolution). Results are presented for (a) observations for 1950–1995, (b) an AGCM-global MLM simulation, and (c) 4 TOGA-50m slab simulations. The contour interval is 0.2 with values > 0.4 shaded red and those < -0.4 shaded blue.

observed SSTs are specified in the tropical Pacific, but the remainder of the world oceans are simulated by a slab model without mixed-layer physics. The observational column in **Fig. 2.15** shows that the dominant large-scale SST anomaly pattern that forms in the eastern two-thirds of the North Pacific during winter recurs in the following winter without persisting through the intervening summer. Experiment 1 (middle column) reproduces this behavior, but Experiment 2 (right column) does not. These results suggest 1) that the winter-to-winter SST correlations are due to the reemergence mechanism and not due to similar atmospheric forcing of the ocean in consecutive winters, and 2) that the SST anomalies in the tropical Pacific associated with El Niño are not essential for reemergence to occur.

EPILOGUE

Climate variability on seasonal to interannual scales is dominated by the tropical ENSO phenomenon and its global impacts. CDC scientists have been at the forefront in providing evidence that much of the *predictable* evolution of ENSO and its remote atmospheric and oceanic impacts are governed by low-dimensional, linear dynamics. This clarification has proved extremely valuable for basic understanding and for building simple, useful, forecast models. However, it has also raised important new questions. Foremost among these is perhaps that raised by **Figure 2.4**. How much predictability, especially extratropical predictability, exists on this time scale beyond that associated with simple linear ENSO signals? What additional useful predictive information can be extracted by running large GCM ensembles? CDC scientists have addressed these questions by exploring the nonlinearity and sensitivity of the global response to the details of anomalous tropical Pacific SST fields and by focusing on the distributional aspects of the response, especially the changes of variance, rather than just shifts of the mean. We have also contributed to improved understanding of the predictability of SSTs in other ocean basins, through both "atmospheric bridge" and "re-emergence' mechanisms, and the impact of such SSTs on atmospheric predictability. There is encouraging evidence that one will be able to provide substantially improved forecast guidance on this time scale, especially on the tails of the distributions, through better understanding and prediction of these formally second-order but still important effects. The overarching theme of new research in this area must be a community-wide shift from deterministic to probabilistic seasonal predictions. Ultimately, one can extract only so much information from deterministic predictions of a chaotic system. The utility of probabilistic predictions, on the other hand, is unbounded in an important practical sense, in that it is determined to a large degree by the needs of particular users. Future CDC research on this time scale will increasingly reflect this shift of focus to probabilistic predictions, with the climate-society interface and the needs of different categories of user groups in mind.

***Contributed by**: M. Alexander, J. Barsugli, G. Compo, M. Hoerling, S. Peng, C. Penland, and P. D. Sardeshmukh.*

CHAPTER 3

Understanding and Predicting Subseasonal Variations

Given that the details of daily weather are unpredictable beyond about a week, the questions of what aspects of the circulation remain predictable and what useful information can be extracted from predicting them present interesting challenges. The forecast problem is particularly difficult for Week 2, because boundary conditions have begun to become important but initial conditions have not yet completely lost their influence; at the same time, the chaos from unpredictable nonlinear interactions has nearly saturated. This is mainly why prediction efforts have traditionally focused on shorter (synoptic) and longer (seasonal to interannual) time scales. And yet there is much to said for shifting some of the focus to the subseasonal scale, if only because variability on this scale accounts for a large fraction of the total atmospheric variability from synoptic to decadal scales. Also, episodes of springtime floods, summertime droughts, and prolonged wet or dry spells are phenomena with obvious societal consequences.

CDC scientists are addressing these issues by focusing on the variability and predictability of weekly averages, through both modeling and diagnosis of the observed statistics, and through detailed investigations of NCEP's operational forecast ensembles for Week 2. A significant recent accomplishment was the construction of a low-dimensional 37-component linear empirical-dynamical model that not only successfully represents the statistics of weekly anomalies but also has comparable forecast skill in Week 2 to that of NCEP's operational ensemble. There is evidence that much of this model's skill arises from processes not well represented in the NCEP or other numerical models, such as subseasonal variations of tropical convection. On the other hand, much of the skill of the numerical models is likely due to processes not well represented in the empirical model, such as nonlinear baroclinic cyclogenesis or blocking development in Week 1. It is therefore possible that an intelligent combination of the empirical and numerical model forecasts will yield a Week 2 forecast that is superior to either in isolation. Constructing such a combination is now one of our primary efforts. This effort will benefit from and build on our recent success in improving both statistical and numerical forecast products for this time scale.

3.1 Modeling and understanding the statistics of weekly averages

The principal mechanism of tropical-extratropical interaction is through diabatically forced Rossby waves. On seasonal and longer scales, tropical diabatic heating is strongly linked to tropical SST; hence one speaks of an "SST-forced" global response as in Chapter 2. On the subseasonal scales of interest here, the SST variability is relatively weak, and its coupling to the heating variability is much less rigid. The heating variability itself is considerable, however, and has a significant extratropical impact. Some of this variability (especially that associated with the MJO) is predictable, and raises the hope that at least some aspects of subseasonal extratropical variability may therefore also be predictable. Unfortunately, for various reasons the simulation and predictability of subseasonal tropical heating variations has thus far proved difficult in general circulation models. This has been a major stumbling block in capitalizing on this source of subseasonal extratropical predictability.

Inspired by the success in **Figs 2.1–2.4** of simple empirical predictions of seasonal tropical SST variations and their global impact, we have recently constructed a linear inverse model (LIM) suitable for studies of atmospheric variability and

predictability on weekly time scales using global observations of the past 30 years. Notably, it includes tropical diabatic heating as an evolving model variable rather than as an externally specified forcing. It also includes, in effect, the feedback of the extratropical weather systems on the more slowly varying circulation. We have found both of these features to be important contributors to the model's realism.

The model is concerned with the behavior of 7-day running mean anomalies of extratropical streamfunction and column-averaged tropical diabatic heating. It assumes that atmospheric states separated by time lags τ are related as $\mathbf{x}(t+\tau) = \mathbf{G}(\tau)\,\mathbf{x}(t) + \varepsilon$, where $\mathbf{G}$ is a linear operator and ε is noise. This implies that the zero-lag and time-lag-covariance matrices of $\mathbf{x}$ are related as $\mathbf{C}(\tau) = \mathbf{G}(\tau)\mathbf{C}(0)$. We use this relationship at a particular lag, say τ = 5 days, to obtain $\mathbf{G}(5)$ from observational estimates of $\mathbf{C}(5)$ and $\mathbf{C}(0)$. We then make another assumption that is at the heart of the LIM formalism, that distinguishes it from other empirical models, and that enables one to make dynamically meaningful diagnoses of direct relevance to modelers. This is that $\mathbf{G}(\tau)$ satisfies the relation $\mathbf{G}(\tau) = \exp(\mathbf{L}\tau)$, where $\mathbf{L}$ is a *constant* linear operator. We use this to obtain $\mathbf{L}$ from $\mathbf{G}(5)$, and having done so, use it again to obtain $\mathbf{G}$ for all other lags. We are finally in a position to make forecasts for all lags as $\mathbf{x}(t+\tau) = \mathbf{G}(\tau)\,\mathbf{x}(t)$. Crucially, having obtained $\mathbf{L}$, we can also diagnose the relative importance of its elements associated with tropical-extratropical and internal extratropical interactions. For example, we can use $\mathbf{L}$ to estimate what the statistics of extratropical variability would be without diabatic forcing from the tropics.

Figure 3.1 demonstrates the success of this model in reproducing the observed variance and 21-day lag covariance of 7-

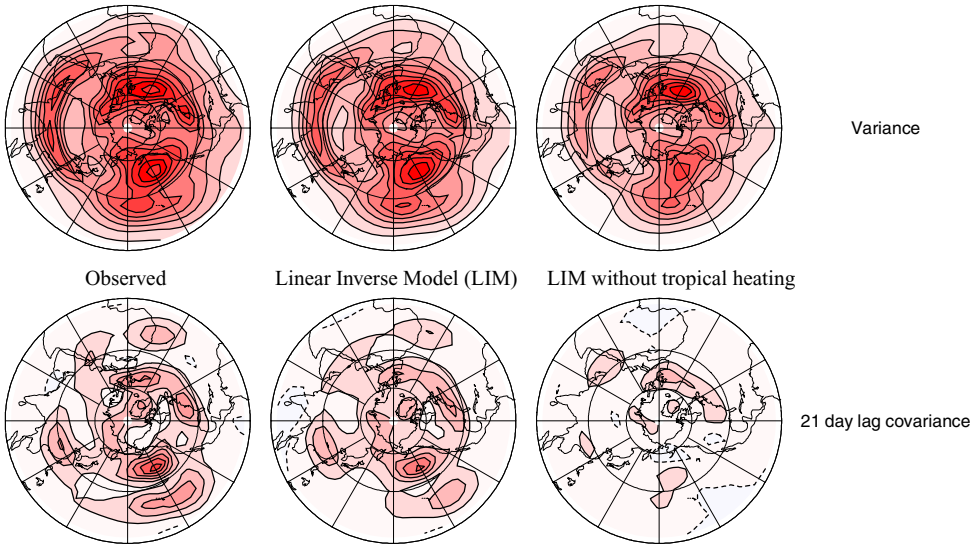

Fig. 3.1: Observed and modeled (using the full LIM and a version of the LIM in which the effects of tropical heating are removed) statistics of weekly 250 hPa streamfunction anomalies.

day running-mean anomalies of 250 mb streamfunction during northern winter. Note again that we are effectively using the observed 5-day lag covariances to predict the 21-day lag covariances here. The comparison of the observed and predicted covariances is clearly encouraging. The right column shows that the effect of tropical heating is relatively small on the variance but relatively large on the 21-day lag covariance. This is consistent with our finding that although tropical heating contributes a relatively small portion of the extratropical variability, it contributes a large portion of the *predictable* variability.

Forecast skill is an important test of any model. The LIM is better at forecasting Week 2 anomalies than a dynamical model based on the linearized baroclinic equations of motion (with many more than the LIM's 37 degrees of freedom) that is forced with *observed* tropical heating throughout the forecast. Indeed at Week 2 the LIM's skill is competitive with NCEP's MRF model with nominally $O(10^6)$ degrees of freedom. The upper panel of **Fig. 3.2** shows such a comparison of Week 3 forecast skill during the winters of 1985/86–1988/89. Other experiments show that this encouraging forecast performance is not limited to years of El Niño or La Niña episodes.

The LIM assumes that the dynamics of extratropical low-frequency variability are linear, stable, and stochastically forced. The approximate validity of these assumptions has been demonstrated through several tests. A potentially limiting aspect of such a stable linear model with decaying eigenmodes concerns its ability to predict anomaly growth. We have nevertheless found, through a singular vector analysis of the model's propagator **G**, that predictable anomaly growth can and does occur in this dynamical system through constructive modal interference. Examination of the initial structures associated with optimal anomaly growth further confirms the importance of tropical heating anomalies associated with El Niño and La Niña as well as Madden-Julian oscillation episodes in the predictable dynamics of the extratropical circulation.

The LIM formalism also allows one to estimate predictability limits in a straightforward manner. Indeed it allows one to estimate the expected skill of any *individual* forecast from the strength of its predicted signal. Given that in many cases the predictable signal is associated with tropical forcing, one can quantify the effect of that forcing on extratropical predictability. Our general conclusion is that without tropical forcing, extratropical weekly averages may be predictable only about two weeks ahead, but with tropical forcing, they may be predictable as far as seven weeks ahead. This difference is highlighted in the lower panel of **Fig. 3.2**. This suggests that accurate prediction of tropical diabatic heating, rather than of tropical sea surface temperatures *per se*, is key to enhancing extratropical predictability on these time scales.

As mentioned earlier, most current GCMs have difficulty in representing and predicting heating variations on these scales. This is especially true of the

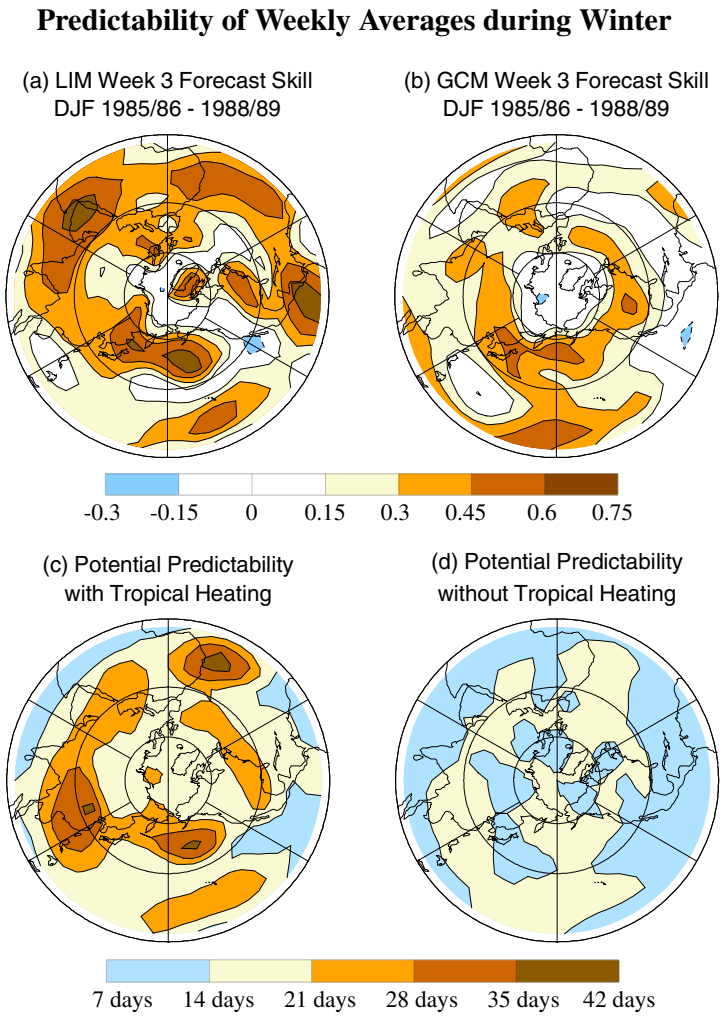

Fig. 3.2: Forecast skill and predictability of weekly averages during winter. Top: Correlation of observed and Week 3 forecasts of upper tropospheric streamfunction anomalies averaged over 52 forecast cases in the winters of 1985/86–1988/89 for (a) LIM and (b) the NCEP MRF. Bottom: Potential predictability limit: forecast lead at which skill (i.e., the correlation of observed and predicted anomalies) drops below 0.5. (c) Determined from the full LIM. (d) Determined from a version of the LIM in which the effects of tropical forcing are removed.

NCEP MRF model. We have documented significant deficiencies in the "reanalysis version" of that model in maintaining and propagating MJO-related heating and circulation anomalies. **Figure 3.3** shows that forecasts initialized when the MJO is active over the Indian ocean are unable to represent the subsequent eastward propagation of 850-mb zonal wind anomalies; indeed they do not predict propagation at all but a rapid decay. This has been demonstrated to have a negative impact on extratropical forecasts.

Figure 3.4 shows that the LIM's forecast skill over the PNA region is comparable to that of the operational MRF ensemble mean, especially in summer. The MRF can represent some phenomena that the LIM cannot, such as nonlinear baroclinic cyclogenesis and blocking. To the extent

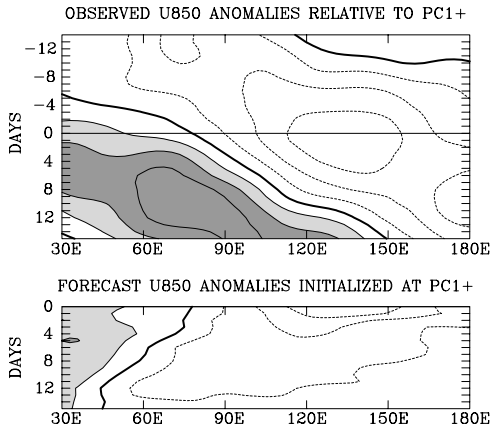

Fig. 3.3 Composite anomalies of 850 mb zonal wind averaged between 5°N–15°S relative to the maximum of the first EOF of subseasonal tropical OLR anomalies, when MJO activity is maximum over the east Indian ocean. The upper panel is for observed anomalies from Days –14 to +14, where Day 0 refers to the time of maximum EOF coefficient. The lower panel is for the anomalies predicted by the NCEP MRF model, with the mean model error removed.

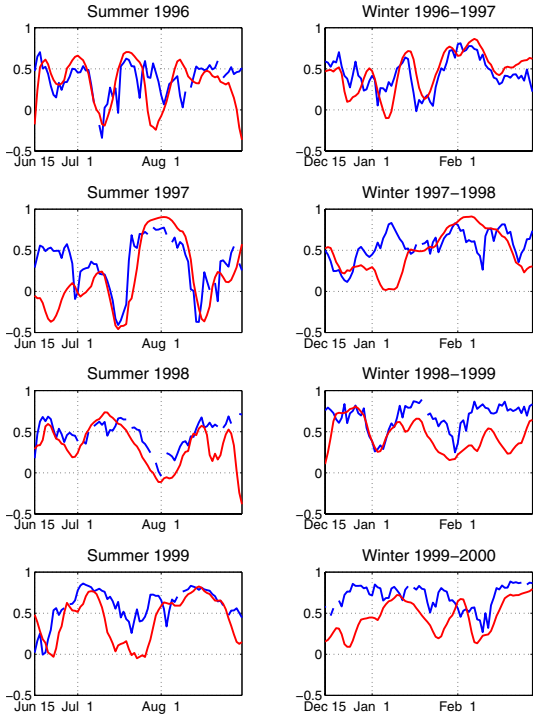

Fig. 3.4: Week two forecast skill (as measured by pattern anomaly correlation over the PNA regions) for the operational NCEP MRF ensemble mean (blue curve) and the LIM (red curve) for four winter and summer seasons.

that these phenomena are predictable, the MRF should have an advantage. This is indeed the case in Week 1. By Week 2, these phenomena become unpredictable; even so, their role in exciting larger scale, slowly evolving structures such as the PNA pattern in Week 1 can contribute to maintaining forecast skill in Week 2. On the other hand, the LIM is much better at predicting subseasonal variations of tropical convection than the MRF, and being an anomaly model, also does not suffer from climate drift by construction. Therefore, it seems likely that the comparable skill of the LIM and the operational MRF models is not arising entirely from the same sources. This is in contrast to the seasonal prediction problem discussed in Chapter 2, in which the comparable skill of GCMs and simple statistical models arises from essentially the same source. To the extent that the sources of Week 2 forecast skill in the statistical and dynamical models are distinct, combining the two forecasts should, in principle, yield forecasts that are superior to either in isolation. Constructing such a combination is currently one of our main priorities.

3.2 Subseasonal variations in tropical convection and predictability of California rainfall.

Figure 3.2 demonstrates that much of the LIM skill in the extratropics arises from its ability to predict tropical heating variations. Operational models are notoriously poor at this. This has implications for predictions of extratropical rainfall:

for example, rainfall along the west coast of North America is known to be influenced by subseasonal tropical heating. This suggests that operational precipitation forecasts over North America could be improved, particularly in Week 2–3 range, by using statistical methods to augment the numerical product. CDC scientists have obtained a conservative lower bound on the potential improvement through a statistical prediction model of weekly precipitation over western North America in winter.

The model is based on Canonical Correlation Analysis (CCA), with tropical Outgoing Longwave Radiation (OLR) anomalies as the predictor and NCEP Reanalysis precipitation over the eastern Pacific and western North America as the predictand. A single CCA mode accounts for most of the predictable signal. The rank correlation of this mode and observed rainfall anomalies over Southern California over a 25-winter period is 0.2 for a two-week lag, which is comparable to the correlation between a weekly ENSO index and weekly rainfall in this region. **Figure 3.5** shows that this corresponds to a 50% increase above the climatological risk (33%) of above-normal rainfall in California when the projection of tropical OLR on the leading CCA mode two weeks earlier is high, i.e. in the upper quintile of its distribution.

The leading CCA mode represents suppressed convection over the equatorial Indian Ocean and enhanced convection east of the dateline (**Fig 3.6**). Associated with this canonical tropical OLR anomaly pattern is the development of upper tropospheric westerly wind anomalies

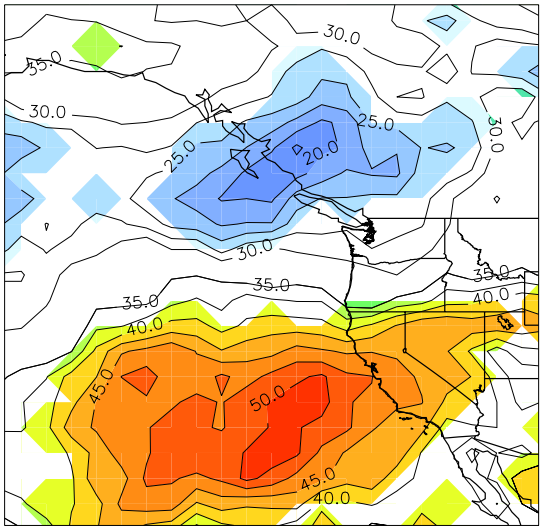

Fig. 3.5: Probability that rainfall will be in the upper tercile of its distribution when the projection of the tropical OLR on the leading CCA mode two weeks prior is in the upper quintile of its distribution.

near 30°N in the eastern Pacific (not shown). Synoptic-scale weather systems are steered farther east toward California by these enhanced westerlies.

An analysis of four years of operational Week 2 ensemble forecasts indicates that the skill of this statistical model is comparable to that of the operational ensemble mean, just like the LIM forecasts discussed earlier (see **Fig. 3.4**). Since by Week 2 the operational forecast model has lost its ability to represent subseasonal tropical heating variability, the statistical model provides essentially independent guidance to the forecaster. The fact that the skill of the two models is comparable suggests a significant potential for improvement of the operational Week 2 precipitation forecasts. We are investigating ways of optimally combining the numerical and statistical forecasts. This requires estimating the covariances of the ensemble mean fore-

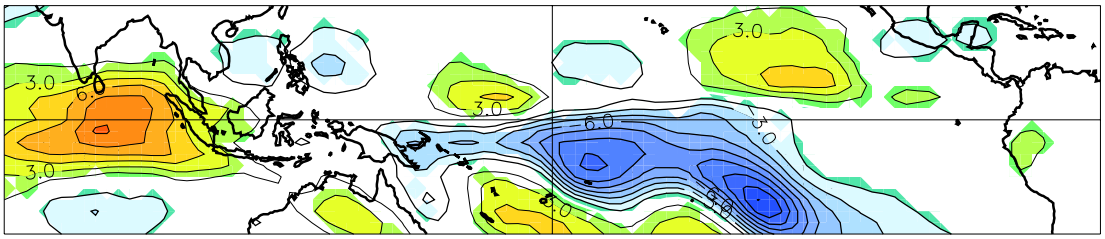

Fig. 3.6: OLR regressed on leading canonical predictor vector, scaled for one standard deviation of the canonical predictor variable. Contour interval is 1.5 W m^{-2}. Positive contours are thicker, the zero line is omitted and shading indicates statistical significance at the 95% level.

cast errors and observed tropical heating variability. Since the tropical convective events associated with predictability on this scale occur only about once or twice a season, a long (20+ year) record of numerical forecasts with a frozen model is needed to estimate the required forecast error statistics. Work is underway at CDC to create such a retrospective forecast database.

3.3 The role of ENSO-related tropical heating on operational weather forecasts

The crucial role of tropical heating in the evolution of at least some extratropical weather events is evident in a study of the effect of the 1997–98 El Niño on the operational 1–14 day ensemble forecasts. This study was motivated by the hypothetical question: What would happen to the medium-range (up to 14-day) forecast if the anomalous tropical SSTs were replaced by climatological values? The difference of such forecasts from those made with the actual SSTs— "the ENSO signal"—could then be used to diagnose the influence of El Niño or La Niña on evolving midlatitude storm systems. Because of the uncertainty inherent in weather forecasting, we used the operational MRF ensemble to look at the average of many forecasts of a given storm. The ensemble also provided us with a rigorous way of assessing the statistical significance of our results. It is perhaps worth mentioning that the ensemble with climatological SSTs was run in-house at CDC in real time. Results from the comparison with NCEP's operational ensemble with actual SSTs were made available to public on the web, also in real time.

This study provided the first demonstration of a direct impact of El Niño SST anomalies on individual extratropical weather systems. Perhaps the most interesting case was the devastating ice storm that hit Canada in early January 1998. **Figure 3.7** shows the predicted 500 mb ensemble-mean height anomaly patterns with and without the El Niño SST forcing, as well as the observed verification. The forecast was a lot closer to the observed with the El Niño forcing included, showing that it played an important role in the evolution of this storm. The area of unusually warm mid-level air associated with the production of freezing rain is indicated by the red arrow. The operational runs (with El Niño SSTs) show a wavetrain aligned

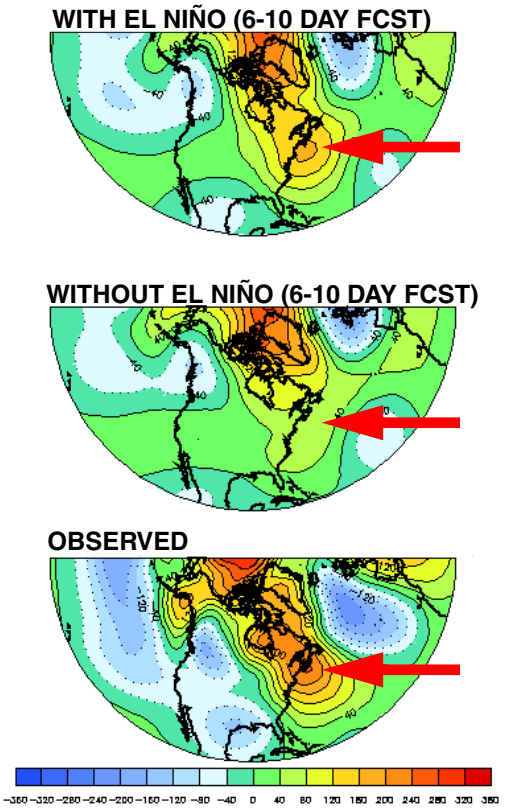

Fig. 3.7: Ensemble mean 6–10d average 500 hPa height anomalies for the ensemble with observed tropical SSTs (upper panel) and the ensemble with climatological tropical SSTs (middle panel) for forecasts verifying the first week of January 1997. The lower panel shows the verifying analysis, and the red arrows indicate where unusually warm air at mid-levels contributed to the development of freezing rain at the surface.

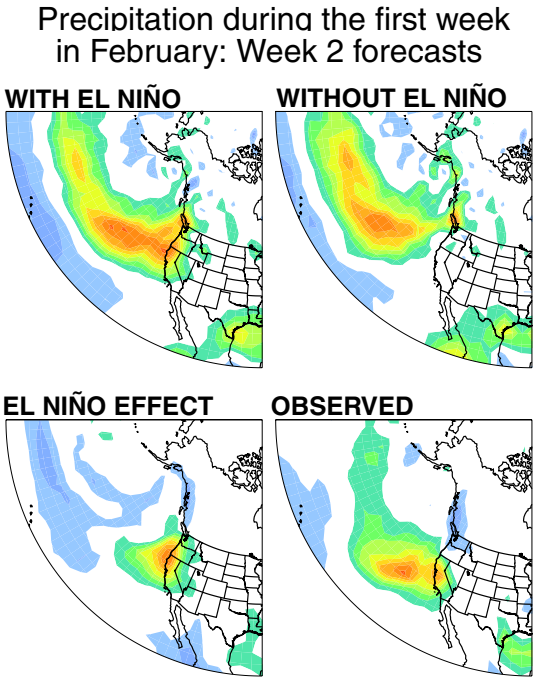

Fig. 3.8: Precipitation accumulated over the second week of the forecast for the ensemble with observed tropical SSTs (upper left), climatological SSTs (upper right), and the difference between the two (lower left) for forecasts verifying the first week of February 1998.

along the Atlantic Coast of the United States that is nearly absent in the runs without the El Niño forcing. This wavetrain appears to have been a product of convective forcing in the eastern tropical Pacific interacting with a deep mid-latitude/subtropical trough over Mexico: a previously unnoticed mechanism for El Niño teleconnections.

The much-anticipated "El Niño rains" in California provide another example. California rainfall is episodic, even during El Niño years. Rain also falls during non-El Niño years, making attribution of an individual storm to El Niño nearly impossible using historical data alone. However, our use of a dynamical model allowed us to make the attribution directly. In **Fig. 3.8** the runs with and without the El Niño forcing differ substantially. The "El Niño effect" is a clear eastward extension of the rainfall into California.

We conducted a similar study for the following winter, during which there was a substantial La Niña event. However, the results were less conclusive, partly because of model changes and partly due to the weaker SST forcing. Nonetheless,

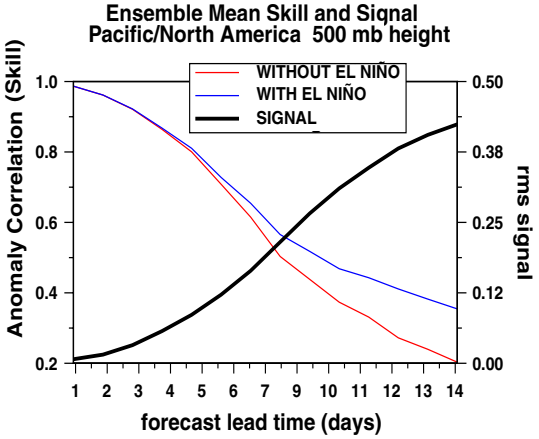

Fig. 3.9: Week 2 500 hPa height anomaly correlation skill over the PNA region for the ensemble mean with (blue) and without (red) El Niño SST anomalies in the tropics. The black curve shows the RMS 500 hPa height El Niño Week 2 forecast "signal", defined as the difference in the ensemble mean forecasts with and without tropical SST anomalies.

over the course of these two winters this experiment provided evidence of a large influence of tropical convection on medium and extended-range forecasts in midlatitudes, especially in Week 2. **Figure 3.9** shows that the tropical influence on forecast skill became significant after Week 1 in this experiment, and was responsible for almost all of the skill by day 14. This study also underscored the great difficulty, but also the great rewards, of using an operational forecast model in research mode. As an added benefit, we were able to assist NCEP during their fire-related computer outage by running the operational ensemble forecasts at CDC in real time.

3.4 The relationship between spread and skill in the operational NCEP ensemble forecasts

The studies discussed in sections 3.1 and 3.2 show that statistical models can have skill comparable to NWP models in the Week 2 to Week 3 range because subseasonal variations of tropical convection, which the NWP models do not simulate well, provide significant predictive information. However, the NWP models, unlike the statistical models, can provide information on day-to-day variations of both the signal (the amplitude of the predictable component of the forecast) and noise (the amplitude of the unpredictable component of the forecast). The statistical models assume the noise to be stationary, i.e. to not vary from forecast to forecast. An NWP ensemble can be used to estimate the noise in each forecast case, and hence a case-dependent estimate of the RMS error of the ensemble-mean forecast.

The simplest measure of forecast noise is the width, or spread, of the forecast probability distribution for any quantity of interest. CDC scientists have investigated the relationship between spread and skill in the operational NCEP forecast ensembles using an archive of operational forecasts maintained at CDC since 1995. Simple statistical considerations show that such a measure is most useful when the case-to-case variability of the ensemble spread is large. This was shown to be true in two winters of operational ensemble predictions. However, the short data record precluded a detailed analysis of

the dynamical mechanisms of the spread variability.

To get around this limitation, a five-level linear quasi-geostrophic (QG) model, linearized about three-day segments of the observed flow for 21 years, was used to model the spread variability. The fundamental assumption was that day-to-day variations of spread are due primarily to day-to-day variations in the growth rate of small perturbations during the forecast period, and that day-to-day variations in the initial error, i.e. in the spread of the analysis-error distribution, are either unimportant or not well sampled. The five-level model was able to reproduce the main results (not shown) of the shorter 2-winter study mentioned above. When run for 21 years, the QG model showed the largest spread variability of 3-day forecasts over the eastern Pacific and eastern Atlantic oceans, which was associated with modulations of the local jets by the PNA and NAO modes of low-frequency variability (**Fig. 3.10**). To the extent that such modulations are predictable, the results from this study suggest that skill should also be most predicable in these regions.

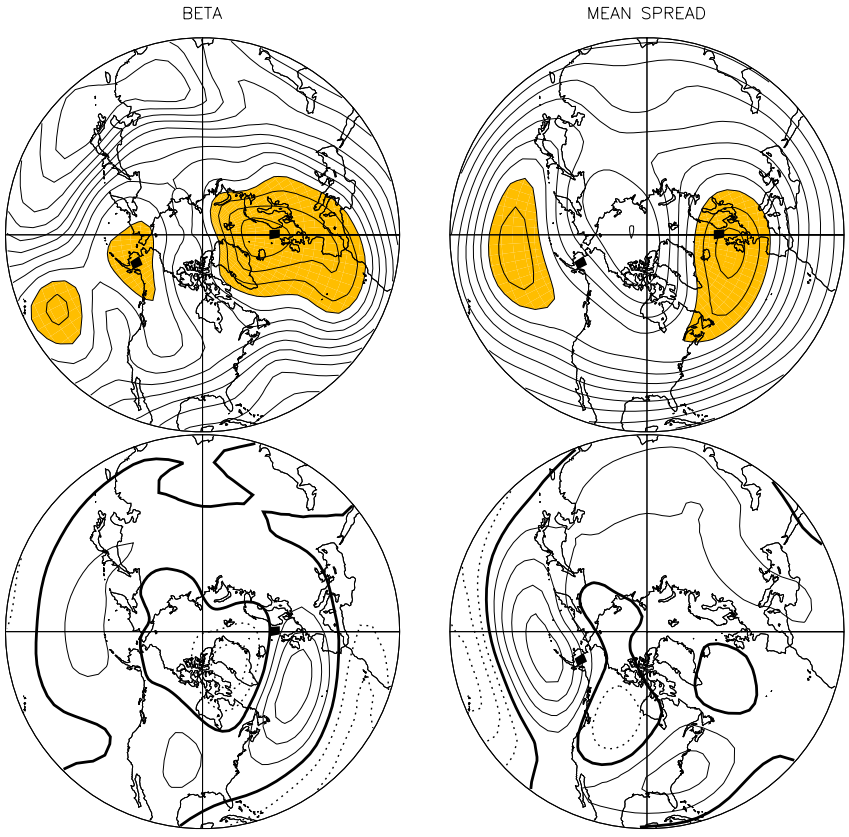

Fig. 3.10: Upper panels: 21 winter mean 300 hPa streamfunction spread (S) and standard deviation of lnS (=β), estimated from 3-day integrations of the five-level linear QG model. S is normalized by the mean amplitude of the initial perturbations used in the ensemble integrations. Contour interval for β is 0.01, with values greater than 0.28 shaded. Contour interval for normalized S is 0.25, with values greater than 4 shaded. Lower Panels: Map of correlations between time series of lnS at points indicated by the black rectangles and three-day averaged 300 hPa streamfunction. Contour interval is 0.1, negative values are dashed, and the zero line is thick solid.

3.5 Experimental week 2 forecasts of extreme events using the operational NCEP ensemble

The existence of a significant spread-skill relationship (at relatively short forecast ranges) means that changes of both the mean and width of the forecast probability distribution from their climatological values can be used to estimate the probability that the verification will lie in the tails of the climatological probability distribution (see **Fig. 2.6**). The statistical models discussed earlier assume that the spread is constant, and that only shifts of the mean are important in altering the probability that the verification will be an "extreme event".

Unfortunately, this advantage of ensemble forecasts, which is modest but significant in Week 1, is lost by the middle of Week 2. The main reason is that by Week 2 the forecast ensemble spread nearly saturates to its climatological mean value, so that there are no significant spread variations from case to case. In other words, most of the predictable variation of forecast skill in Week 2 is associated with predictable variations of the signal, not of noise. For several years CDC has exploited this fact in producing an experimental real-time Week 2 forecast product based on the NCEP ensemble (http://www.cdc.noaa.gov/~jsw/week2/). Tercile probability forecasts of 500 mb height, 850 mb temperature, 250 mb zonal wind, sea-level pressure and precipitation are provided. Only the signal, not noise, is used to construct these probability forecasts. The procedure involves converting maps of the predicted standardized anomalies into maps of extreme quantile (in this case, tercile) probabilities. This calibration is done empirically, using the available historical record of ensemble forecasts and verifying analyses. The procedure is as follows: 1) for a positive standardized forecast anomaly α, all instances in which a forecast *exceeded* this value in the data record are found, and the probability β that the verifying analysis fell in the upper tercile of the climatological distribution is computed, 2) the standardized anomaly contour α is relabeled as a probability of above-normal equal to β. If α is negative, the probability that the verifying analysis fell into the lower tercile is computed, and the contour is relabeled "probability of below-normal". If the model has systematic errors, these probabilities need not be symmetric, i.e. the probability of below-normal for a negative α need not be the same as the probability of above-normal for a positive α. Our calibration thus provides one simple way of accounting for model error in probabilistic predictions.

Figure 3.11 shows an example of such a probability forecast. Note that the interpretation of this map is slightly different from that for a conventional probability forecast. If all the points on the map inside the yellow contour (as opposed to those inside the yellow *band*) are counted over a large sample of forecasts, 50–60% of these points will verify in the upper tercile of the climatological distribution. Similarly, for points falling in the darkest red regions on the map, over 90% will verify in the upper tercile. The conventional interpretation would be that points

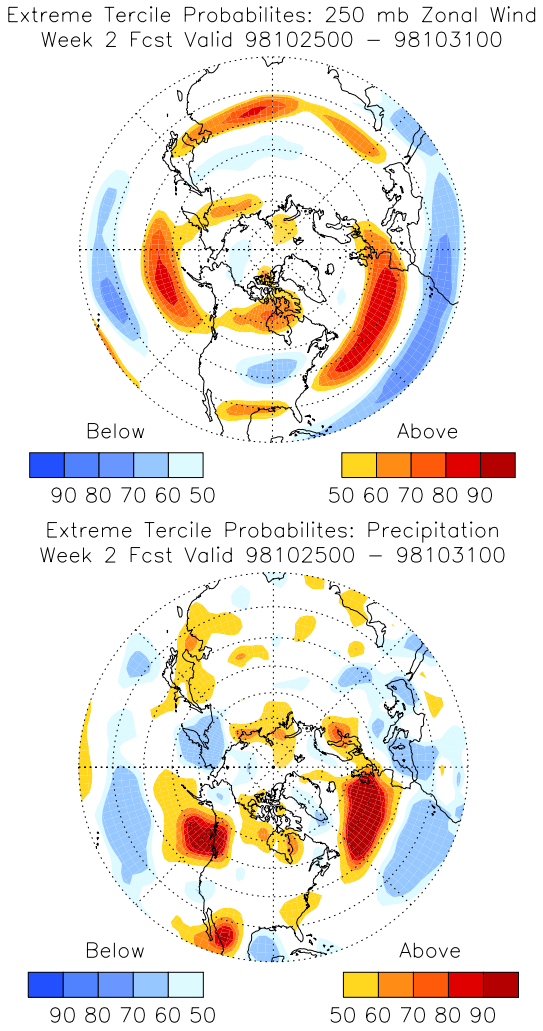

Fig. 3.11: Example of an experimental week 2 forecast verifying the last week of October 1998.

in the yellow *band* would have a 50–60% chance of verifying in the upper tercile. Such a calibration would require a lot more forecasts to compute reliably, since there are far fewer points inside the yellow band than there are inside the yellow contour.

Since we assume that the signal, not the noise, contains all of the useful predictive information, the useful subspace of the ensemble can be isolated through an EOF analysis of the correlation matrix of the ensemble-mean predictions. (The idea here is similar to that in **Fig 2.8**). The right panels of **Fig. 3.12** show the three leading EOFs thus obtained. For comparison, the three leading EOFs of the correlation matrix of observed 7-day averages is also shown, in the left panels. There are two notable aspects to **Fig. 3.12**: 1) the signal and observed EOF patterns are similar, and 2) the three leading EOFs explain considerably more variance of the ensemble-mean forecasts than they do of the observed variability (36% vs. 22%). To understand this better, note that the total forecast covariance can be decomposed into a part due to the predictable signal ($\mathbf{C}_{signal}$) and a part due to unpredictable noise ($\mathbf{C}_{noise}$). If the forecast model is unbiased and the noise is uncorrelated with the signal, the observed variance ($\mathbf{C}_{obs}$) is approximately the sum of the two. This relationship is exact for the LIM discussed in section 3.1. The fact that the signal variation occurs in a lower dimensional subspace than the observational 7-day averages then simply means that the variance contained in the noise is non-trivial. The similarity of the observed and signal EOF patterns has a subtler interpretation: it implies that the noise component of the covariance is nearly white, and that the ensemble-mean does indeed capture most of the extractable signal with coherent spatial structure.

The product shown in **Fig. 3.11** has been quite popular with operational forecasters. A similar method has been adopted in operations by NCEP/CPC. A detailed analysis of the performance of this

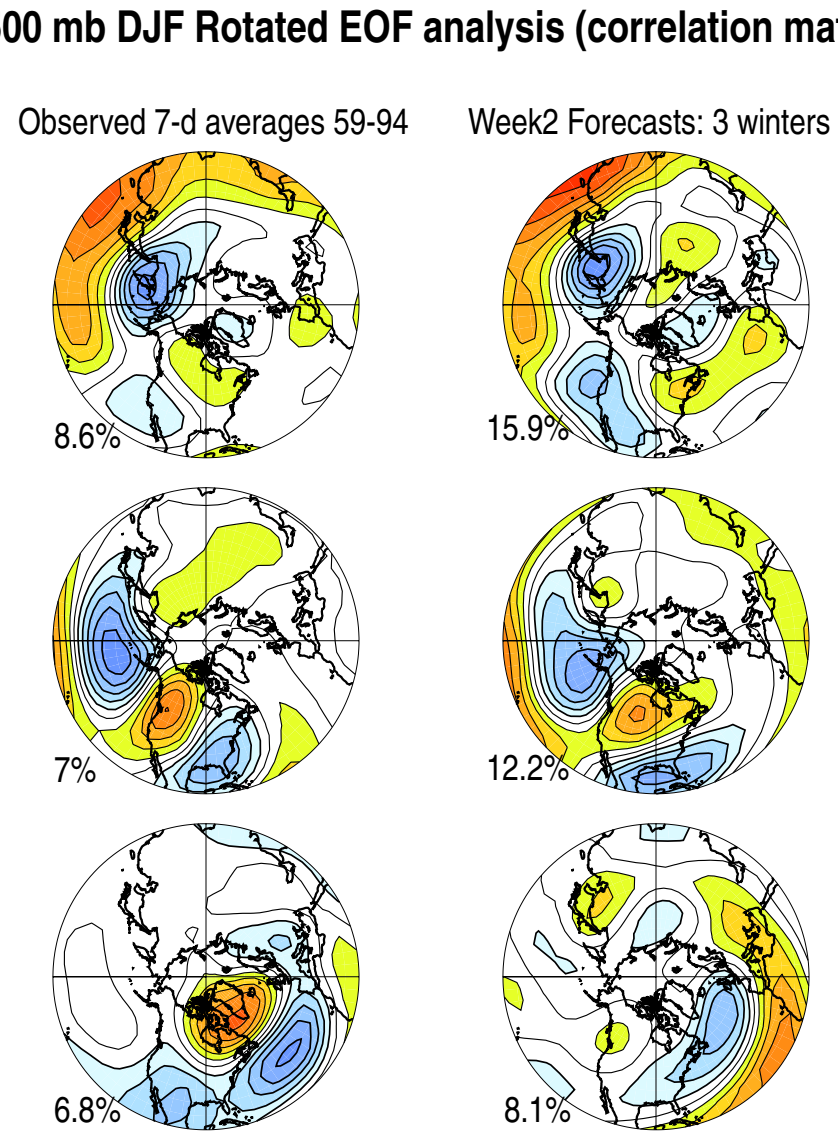

Fig. 3.12: Rotated EOFs of weekly average 500 mb height computed using the correlation matrix for DJF 1958-1994 (left panels) and the correlation matrix of week 2 operational ensemble mean forecasts for DJF 1995/96 to 1997/98.

scheme, and its implications for Week 2 predictability, is underway.

3.6 Unifying ensemble forecasting and data assimilation.

The fundamental goal in subseasonal prediction, just as in seasonal prediction, is to predict the forecast probability distribution function (PDF) accurately. In the previous sections, we have discussed research efforts at CDC toward this goal. It is hoped that statistical methods like the LIM or CCA, when combined with an NWP ensemble, will improve the mean of the forecast PDF. The spread-

skill relationship discussed in section 3.4 shows that useful information can be extracted at short forecast ranges from the second moment of the NWP ensemble. One obvious way to improve the accuracy of the forecast PDF is to improve the accuracy of the initial PDF. Currently, all operational centers construct an ensemble of initial conditions by perturbing a single control analysis, obtained from a three-dimensional (as at NCEP) or a simplified four-dimensional (as at ECMWF) data assimilation system. The methods used to generate the perturbations to the control analysis, breeding vectors at NCEP and singular vectors at ECMWF, are fundamentally ad-hoc and not representative of analysis uncertainty. CDC scientists have been investigating new ways of coupling the ensemble forecast and data assimilation steps, in order to improve both the initial and forecast PDFs.

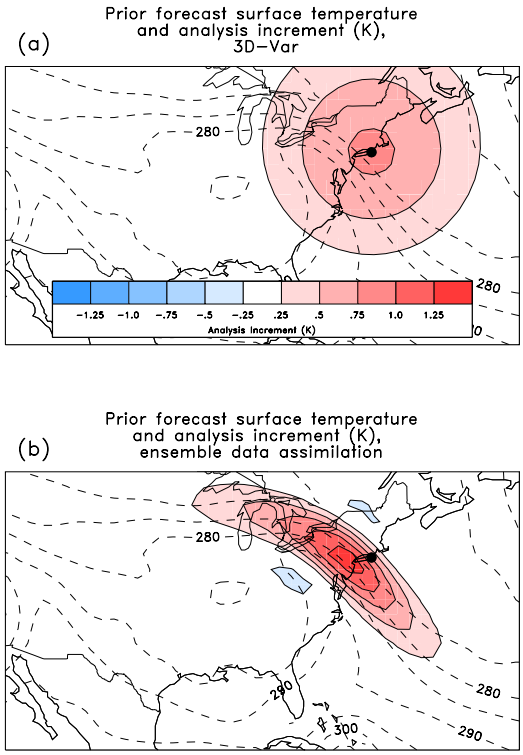

Fig. 3.13: Examination of the structure of the "analysis increment" (the initial condition minus the prior "first guess" forecast) for the traditional method of doing data assimilation, where error statistics do not change from location to location or day-to-day. In this experiment, an observation that is 1 K warmer than the prior forecast is found at the location denoted by the dot. (a) Analysis increments using the "3D-Var" data assimilation methodology. The "one size fits all" increments are a simple decreasing function of increasing distance from the observation location. (b) Analysis increments using the new ensemble data assimilation methodology. Changes to the prior forecast are now stretched out along the frontal zone, so that the entire position of the warm front is changed by the one observation.

The coupling of ensemble forecasting and data assimilation is natural. The essence of data assimilation is statistical, in that it amounts to blending "first guess" forecasts with new observations using weights determined by their respective error statistics. Carefully constructed forecast ensembles can provide such statistics. Currently, operational methods make rather simplistic assumptions about the error statistics, assuming, for example, that the correlation of forecast errors at two locations depends only on the distance between them and not on the location or whether the atmosphere has recently been quiescent or stormy (**Fig 3.13a**). Results from simple model experiments using sophisticated "Ensemble Kalman Filter" techniques suggest that the quality of initial conditions can be dramatically improved by using forecast error statistics estimated from a specially constructed ensemble. For example, error statistics from the ensemble permits a single observation at a fixed location to make very different corrections to the first-guess depending on the

flow of the day (**Fig 3.13b**). By estimating the analysis increment to the first guess in this flow-dependent manner, ensembles of initial conditions can be dramatically improved, perhaps even to the point that they are more accurate than analyses based on four-dimensional variational methods.

Recent CDC efforts in this area have focused on algorithmic details of ensemble-based data assimilation experiments. We have sought to understand how the statistics of forecast errors estimated from an ensemble depend on the size of the ensemble, and how one might extract useful information from smaller ensembles—an important issue, since larger ensembles make heavier demands on computational resources. This research has demonstrated that with an accurate specification of forecast error statistics, new problems can be tackled in a theoretically justifiable manner, including problems such as determining where supplementary observations would be most beneficial for reducing analysis or forecast error (the problem of "targeting" observations). In addition, since ensemble-based data assimilation techniques are particularly useful when observations are sparse, CDC scientists are planning to adapt such techniques to extend the NCEP reanalysis back into the pre-radiosonde era (pre-1948).

EPILOGUE

The problem of how to make useful forecasts at lead times between a week and a month is a challenging and often neglected one. Forecast information on these time scales is in great demand from users. This is an area that NOAA has traditionally not focused on in the past. CDC researchers have been addressing the problem on two fronts; 1) by trying to extract the maximum information from ensemble NWP model forecasts, and 2) by investigating statistical forecast methods that complement the NWP ensembles by exploiting predictable signals not well represented in current models. Our research thus far suggests that the NWP and statistical approaches are complementary, and provide information that is independent to some degree. The challenge is to combine the two in an optimal manner, yielding forecasts that are superior to either individually. Due to the low-frequency nature of the phenomena at these forecast ranges, determining the optimal combination would require generating a long (20+ year) dataset of ensemble forecasts with a fixed model to estimate the forecast error statistics with the necessary accuracy. Work is currently underway at CDC to create such a dataset, which will also be useful in several other applications not discussed here.

Contributed by: *J. Barsugli, T. Hamill, H. Hendon, B. Liebmann, M. Newman, P. Sardeshmukh, and J. Whitaker.*

CHAPTER 4

Empirical and Process Studies

CDC conducts diverse research activities that span time scales from intraseasonal to decadal. Whereas other chapters focus on specific time bands, this chapter considers basic physical processes important in climate variability that occur across time scales. Moist atmospheric convection, clouds and climate, atmospheric angular momentum, and air-sea interaction are topics of active research. CDC scientists integrate modeling and observations to better understand physical processes, and to overcome limitations in either observational or modeling analyses alone. Coherent phenomena such as ENSO, the Madden-Julian oscillation (MJO) and the seasonal cycle provide specific case studies and important examples of scale interactions.

Moist atmospheric convection is central to all climate phenomena studied at CDC and epitomizes the complexity of the climate system. At CDC, we use observations and hierarchical modeling to conduct fundamental studies of moist convection in various environments. A key objective is to evaluate the assumptions at the heart of present day cumulus parameterization schemes. Cloud-resolving models are used to develop, test and refine parameterizations in a simplified and tractable context.

Clouds also profoundly impact climate variability. CDC research shows that stratocumulus decks over the east Pacific influence the seasonal cycle of sea surface temperature (SST). The three-dimensional structure of clouds helps determine the heating that drives such ocean-atmosphere interactions, and must be properly represented in climate models. CDC scientists have developed a simple cloud overlap scheme for GCMs, and are working on a higher order statistical cloud scheme to better represent the subgrid scale distribution of cloud properties.

A key feature of tropical variability is the MJO, which produces strong air-sea interactions over the warm pool and may influence the ENSO cycle, particularly the onset and decay phases. CDC scientists determined that SST anomalies within the MJO are driven mainly through surface energy fluxes, especially shortwave and latent heat fluxes. MJOs were also shown to play a prominent role at the onset of the 1997–98 El Niño event. MJO events initiated cooling of SSTs in the west Pacific via surface fluxes and warming in the central Pacific via Kelvin wave currents. In the first link identified with interannual SSTs, CDC scientists found that strong MJO activity during the northern winter was correlated with positive SSTA in the western Pacific during the preceding northern fall.

Most prediction models systematically lose atmospheric angular momentum (AAM) during the forecast cycle, a serious concern for such a fundamental quantity. CDC scientists used studies of the AAM budget to demonstrate the negative impact of gravity wave drag, including its role in local and global systematic forecast errors. CDC scientists also constructed a linear model of global AAM anomalies that replicated much of the observed intraseasonal variability and clarified the role of the mountain and friction torque in AAM variations. Composite studies were used to illustrate the regional patterns that produce the torques and helped identify a mid-latitude mode with a time scale similar to the MJO.

The diverse range of activities described in this chapter illustrates the breadth of CDC diagnostics research, provides insight and understanding of different physical processes, and provides a foundation for assessment of climate models.

4.1. Moist atmospheric convection

Understanding moist atmospheric convection and its influence on climate variability is central to empirical and process studies at CDC. It links small-scale turbulent motions to global circulations through cloud formation and precipita-

tion. It connects the slowly varying conditions at the Earth's surface to the faster atmospheric responses, providing much of the long-term predictability of atmospheric circulations. Furthermore, it is the proximate cause of many climate impacts on humanity (e.g., drought, flood, and severe weather) and contributes significantly to systematic errors in climate and forecast models. In light of the complexity of convective processes and the wide range of space and time scales involved, a diverse and opportunistic research strategy has been adopted. This research draws on a wide range of models and observations, from cloud-resolving to planet-spanning, from highly idealized to highly realistic.

CDC scientists have developed a new analysis technique called cylindrical binning that facilitates statistical studies using large Doppler radar data sets. Making effective use of existing data, the relationship between rainrate and horizontal wind divergence (**Fig. 4.1**), which is fundamental to the interaction of mesoscale convection and large-scale circulations, is explored. Here, wind divergence (the line integral of Doppler velocity around a circle centered on the radar) at every level in the atmosphere is regressed onto hourly area-averaged surface rain rate (estimated from reflectivity). Color indicates the size of the circle over which averages are considered. All the profiles exhibit the expected low-level convergence and upper-level divergence. Other interesting features are present that indicate, among other things, the spatial scale of the convective systems. However, the statistical significance and physical interpretation of those features remains uncertain and is a subject of further study.

A more detailed and quantitative, if synthetic, source of data about convection is cloud-resolving models. With increasing computer power, ambitious computations are being performed around the world, and some of the resulting data sets are being analyzed at CDC. For example, **Fig.4.2** shows a vertical velocity field at 1500m altitude in a 1064x32 doubly-periodic cloud-resolving model Convec-

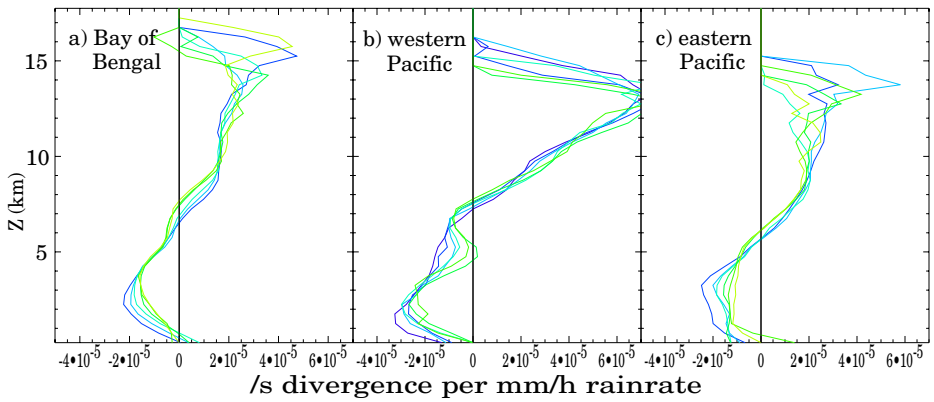

Fig. 4.1. Profiles of the regression coefficient between horizontal wind divergence estimates from Doppler velocity data and near-surface rainrate estimated from radar reflectivity, for 3 month-long radar deployments at sea. Profiles are shown from three approximately month-long deployments of shipborne Doppler radars in the Indian ocean (May 1999), west Pacific (Dec. 1992–Jan. 1993), and east Pacific ITCZ (July 1997).

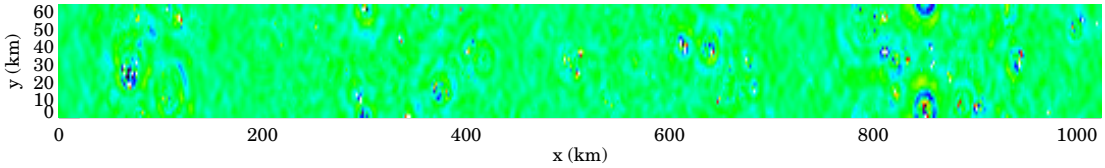

Fig. 4.2. Vertical velocity at 1500 m altitude in a doubly-periodic cloud-resolving model run. White patches (off the ends of the color scale) are convective updrafts (inside red regions) and downdrafts (inside blue regions).

tive updrafts and downdrafts (white patches) are clustered in certain preferred areas, all embedded in the context of a complex gravity wave field. Complete quantitative data about thermodynamics and microphysics as well as motion fields are available—far beyond the capabilities of observations. The simplified context of statistically steady states, periodic domains, and known governing equations allows parameterization hypotheses to be developed, tested, and refined in a tractable context.

More realistic model studies of convection are being pursued with a nested-grid strategy in a mesoscale model (the MM5). The finest grid can resolve convection, while coarser grids require a cumulus parameterization scheme, so this project spans the interface between resolved and parameterized convection. The information flow in the model is very complex, rendering interpretation challenging, but the influence of complex, realistic lower boundary conditions on convection can be studied in detail.

Figure 4.3 shows simulated 3-hour rain accumulations over western Colombia and the adjacent eastern Pacific ocean on 3–4 September, 1998. This region is particularly interesting because it has both steep topography and a strong sea surface temperature gradient offshore, north of the equatorial cold tongue.

In the afternoon/evening, convection occurs over land, fueled by the accumulated moisture from many hours of strong surface fluxes and locally forced by a well-defined sea breeze front near longitude –76.5. In the late night and morning, by contrast, convection erupts in a mesoscale region offshore. Runs without topography suggest that this is due to a

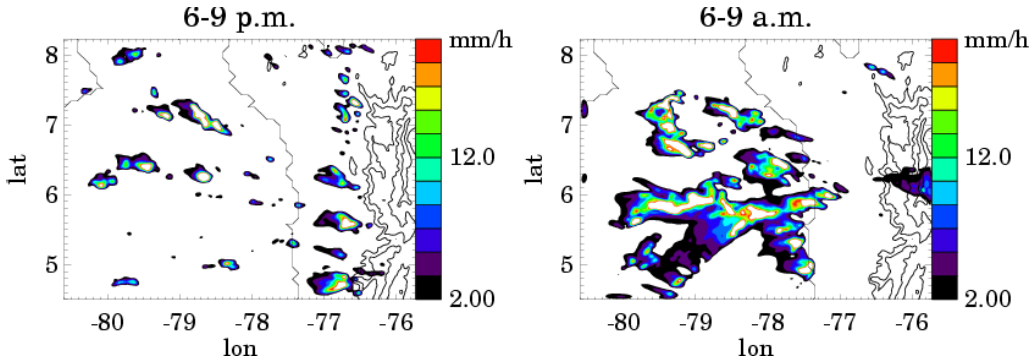

Fig. 4.3. Rainfall rate on 3–4 September 1998 in a nested domain of the MM5 model at 2 km grid spacing. The coasts of Colombia and Panama and 1 km and 2 km terrain elevations are indicated with open contours.

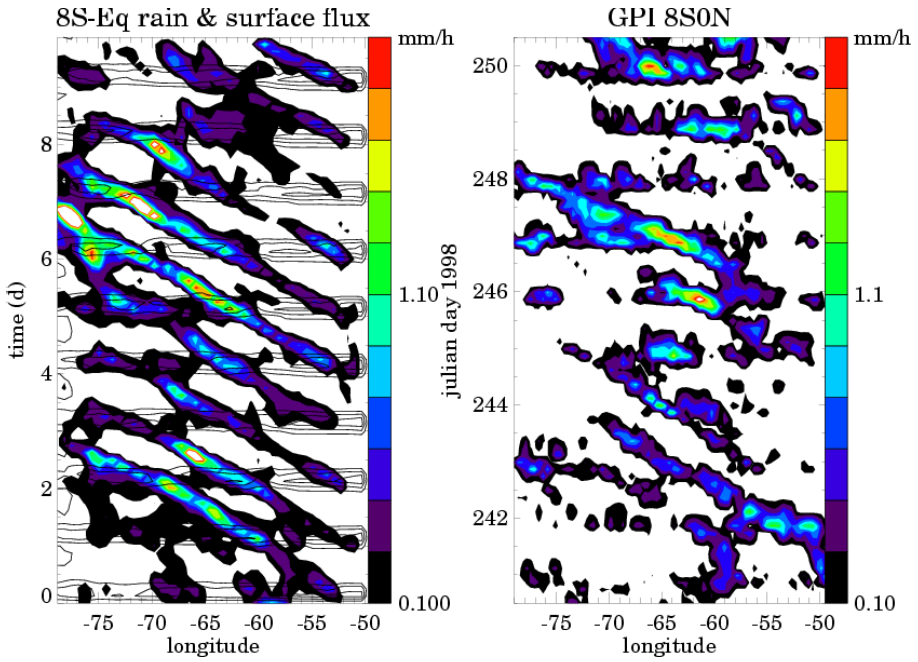

Fig. 4.4. Model (left) and satellite-observed (right) rainbands over the Amazon. Open contours are model surface flux, with contours at 200, 400, and 600 W m^{-2}.

mountain-lowland breeze, not a thermal land breeze *per se*.

The larger, coarser domains of the same model illustrate the interaction of parameterized convection, atmospheric dynamics, and a state-of-the-art land surface model of the Amazon basin at a 72 km grid spacing. Figure 4 shows time-longitude sections of rainfall (color) over the Amazon basin (8°S–Equator) during 28 August–7 September, 1998, from the MM5 (left) and satellite observations (right). Rainbands sweep across the basin, from eastern Brazil to the Andes, at 10 degrees per day.

While the surface fluxes are spatially coherent across the basin (driven by the solar input), the convection occurs in traveling bands, exhibiting some enhancement in the afternoon. The result of this is that the long-term climatology of convection has a striped structure. If we think of the ultimate driver of convection as being the heating of the atmosphere from below, **Fig. 4.4** suggests that convection may be out of equilibrium with this driving by at least half a day, even over a hot moist continent.

These findings suggest that equilibrium parameterizations of convection, as are used in many prediction models, may be inadequate. To explore the consequences of cumulus parameterization assumptions, it is helpful to first consider more idealized large-scale models with parameterized convection. **Figure 4.5** shows rainfall patterns from one run of an idealized model on an earth-sized planet. A warm sea-surface temperature anomaly is specified in the middle of the picture, and the time-mean rainfall enhancement

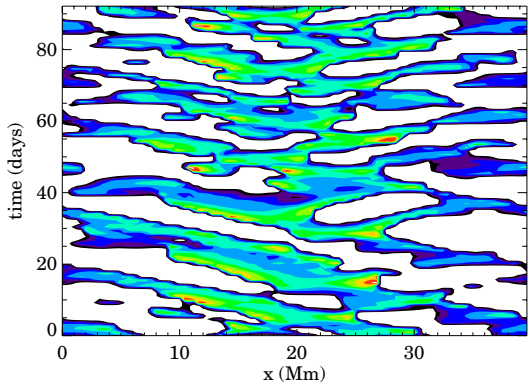

Fig. 4.5. Rainfall rate in an idealized model (Mapes 2000) with a sea surface temperature anomaly in domain center.

depends on the dynamics of the propagating transient activity, which in turn depends on aspects of the cumulus parameterization.

The broad perspective on convective variability afforded by the multi-model approach outlined above is being used to develop convective parameterization schemes whose behavior in models and whose spatial correlation statistics more closely mimic the observations. Models on the various spatial scales can then be used as testbeds for different cumulus parametrization schemes and hypotheses.

4.2 Clouds and Climate

Clouds have a large impact on radiative fluxes, impacting the net energy budget of the climate system, atmospheric heating rates, and energy exchange between the Earth's surface and the atmosphere. Cloud formation is organized by the large-scale atmospheric circulation and, in concert, cloud radiative forcing (CRF) is organized on large-scales. This makes clouds important both for dynamic circulations within the climate system and for model errors that degrade climate simulations, weather forecasts, and reanalysis data. CDC has used observations of cloud variability (e.g., from ISCCP) in a variety of diagnostic and modeling studies in order to improve our understanding of the role of clouds in the climate system.

4.2.1 A high order statistical cloud scheme for GCMs

Large scale models such as those used for weather and climate prediction represent the state of the atmosphere at a discrete set of grid points. These values are used to determine the rates of various processes occurring within the grid cell (how much cloud water is converted to rain, for example). But atmospheric properties vary at all spatial scales, so the properties within a grid cell are better represented by some distribution instead of a single value. If process rates depend non-linearly on the quantity in question, the rate averaged over each grid cell may be different than the rate computed from the grid cell average. The problem is most acute in clouds, especially when computing precipitation rates, as these processes are strongly non-linear in the amount of condensate. The sub-grid scale homogeneity bias in process rates can easily be a factor of two, and is likely the reason models need to be arbitrarily re-tuned at each change in spatial resolution.

CDC and GFDL scientists are working on a statistical cloud scheme that will account for unresolved spatial variability

in the computation of process rates. Cloud resolving model simulations of convection over a mid-latitude land site are being used in two ways: to determine the distributions and parameters that best describe the variability in thermodynamic quantities that would not be resolved by a large-scale model, and to assess how these parameters change according to each physical process. **Figure 4.6**, for example, shows a time-height image of the standard deviation of total water content that would be computed from a model with 512 km grid size and 1 hour time step. Overlaid on this are contours of the detrainment from convective updrafts, which can be seen to increase the amount of variability.

The eventual goal of this work, funded by the Department of Energy through the Atmospheric Radiation Measurement program, is to implement a statistical cloud in the GFDL Flexible Modeling System that predicts higher order moments of one or more thermodynamic quantities at each grid cell. Such a scheme should require substantially less arbitrary tuning than current models, and should be insensitive to changes in spatial and temporal resolution.

4.2.2 A parameterization of cloud overlap for general circulation models

How cloud overlap is specified in a general circulation model can have a large

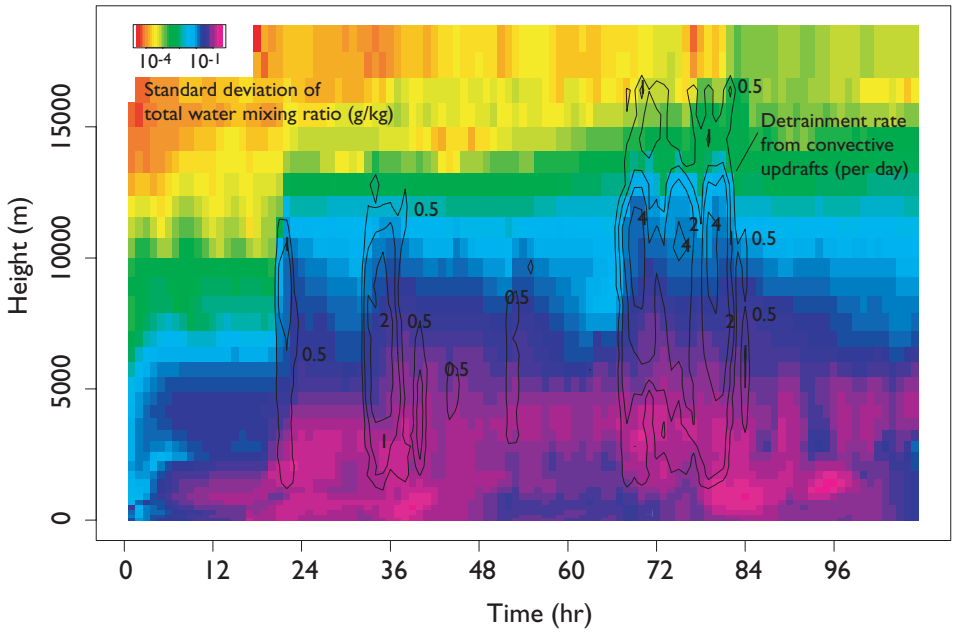

Fig. 4.6. Time-height image of the variability in total water content that would not be resolved by a GCM. The standard deviation of total water (vapor, liquid, and ice) is computed from cloud resolving model simulations of vigorous convection over a continental land site with 2 km resolution sampled every 5 minutes. The small scale values are aggregated to 512 km and 1 hour time step at every level. Variability is in principle produced by turbulence, advection, microphysical process, and convection. The contribution of the latter is clear: the contours show detrainment from convective updrafts, which typically increase the amount of variability.

impact on radiative fluxes and heating rates. Current parameterizations of cloud overlap are also strongly sensitive to changes of vertical resolution. We have recently developed an overlap parameterization that is insensitive to changes of vertical resolution. In our scheme cloud overlap is described in terms of the correlation between horizontal cloudiness functions at different vertical levels. That correlation is assumed to decay exponentially with the separation distance between levels. This allows cloud overlap to be specified in terms of a single parameter, the decorrelation depth. While all pair-wise overlap fractions among cloudy levels can be calculated from the cloudiness correlation, those fractions can over-constrain the determination of the cloud distribution. It is found that cloud fraction in each level along with the overlap fraction among nearest neighbor cloudy levels is sufficient to specify the full cloud distribution. Our overlap parameterization has other desirable features that allow one to interpret the properties of complex cloud distributions in a simplified framework.

4.2.3 The seasonal cycle of cloud radiative forcing in the tropical Pacific

The radiative transfer model from NCAR's general circulation model CCM3 was modified to calculate monthly radiative fluxes and heating rates from monthly observations of cloud properties from ISCCP and temperature and humidity from ECMWF analysis. The modified model was efficient enough to allow a wide range of sensitivity tests. Seasonal variations of cloud radiative forcing were then investigated over the tropical Pacific. This quantifies the impact of clouds on atmospheric heating and on surface energy fluxes. The impact of CRF on surface winds, which also affect energy and momentum transfer at the surface, was then estimated in a linearized calculation of the tropical circulation forced by diabatic heating rates.

Typically, over the tropics, CRF represents approximately 20% of the annual variations of diabatic heating rates over convective locations and 50% or better at nonconvective locations. Seasonal variations of atmospheric CRF, when strong, tend to be in phase with those of total diabatic heating rates, indicating that clouds reinforce tropical circulations driven by latent heating. Cloud radiative forcing tends to have a stronger influence in the lower troposphere than at upper levels. It influences local circulations more than remote ones.

In the tropical east Pacific (85°W to 105°W), we investigated two mechanisms through which seasonal variations of CRF can impact seasonal variations of SST. The first is the 'direct' impact of CRF at the surface, which acts as an energy source for the upper ocean. The second is the 'indirect' impact of atmospheric CRF, which affects meridional surface winds that impact SST through coastal Ekman pumping that brings cool subsurface waters to the surface in the tropical east Pacific. CRF is a major contributor to the energy budget at the surface and in the atmosphere, particularly near and just south of the equator where seasonal variations of SST are strongest

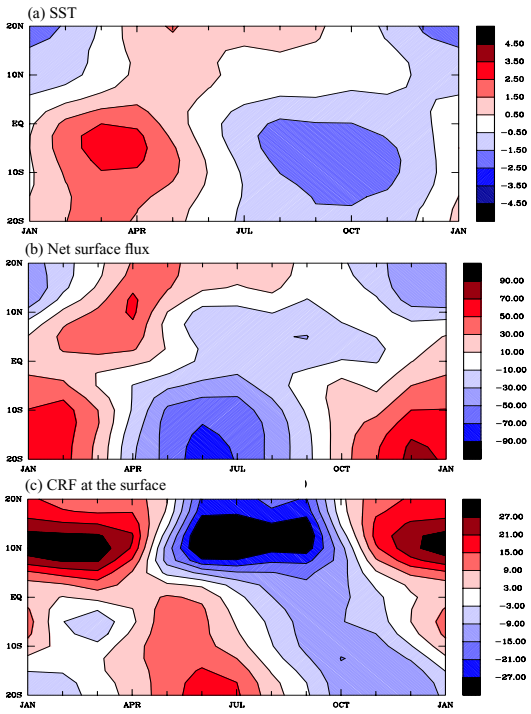

Fig. 4.7. The annual cycle of (a) SST, (b) net surface flux (W m^{-2}), and (c) cloud radiative forcing at the surface in the east Pacific.

(**Fig. 4.7a**). The amplitudes of seasonal variations of surface CRF (**Fig. 4.7c**) are 20–30% as large as those of the net surface flux (**Fig. 4.7b**). However, while the phase relationship between net surface flux and SST is consistent with the surface flux acting to force SST changes (i.e., surface fluxes lead SST by about 3 months), the phase of CRF is not consistent with it forcing SST changes. In fact, over locations where the seasonal cycle of SST is strongest, CRF tends to be out of phase with net surface fluxes, indicating that, if anything, the seasonal cycle of CRF damps SST variability. In contrast, the impact of CRF on meridional winds (relative to latent heating) is strong over the cold tongue (**Fig. 4.8**). Winds driven by CRF also have the correct phase to force the observed seasonal cycle of SST. So, to the extent that surface energy fluxes force the seasonal cycle of SST in the east Pacific, clouds are either unimportant or act to dampen SST variations. To the extent that upwelling driven by meridional winds is important, CRF, principally from season-

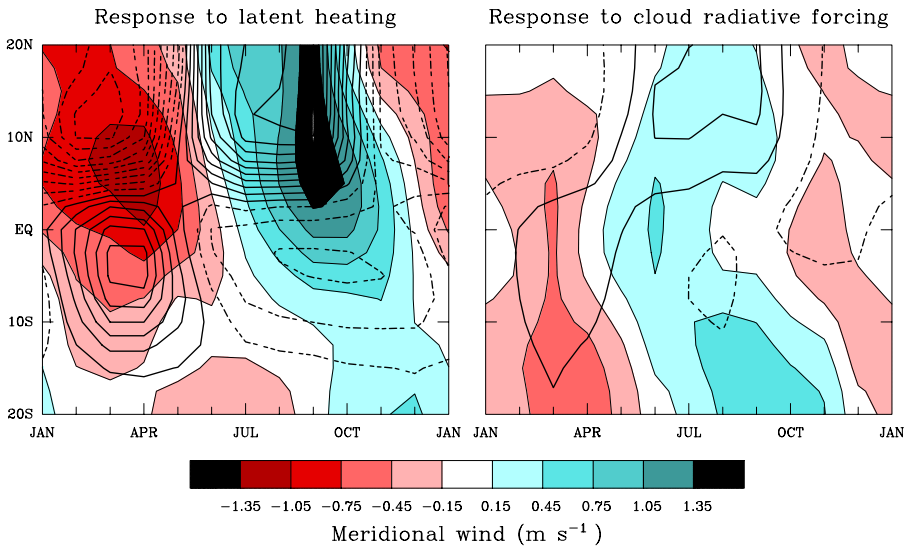

Fig. 4.8. The annual cycle of meridional surface winds calculated in a linearized atmospheric model from (a) latent heating and from (b) atmospheric cloud radiative forcing.

ally varying stratocumulus, is very important.

4.3 Studies of atmospheric angular momentum

Atmospheric angular momentum (AAM) provides a convenient framework to study the role of mountains, surface wind stresses and various transport mechanisms in variability ranging from intraseasonal to interdecadal and beyond. Quantitative studies are feasible with current global assimilated datasets which show a good budget balance for global integrals, intraseasonal variations and during northern winter/spring. The budgets get much worse when gravity wave drag is included, if zonal integrals are considered or during summer/fall seasons. AAM is useful as an index of the large scale zonal flow since it is highly correlated with independent length-of-day measurements and with phenomena such as the QBO, ENSO, the MJO and possibly global warming. CDC scientists have examined several aspects of AAM variability, including: the link to MJO tropical convection, a linear model of global AAM and its torques, the global AAM budget imbalances due to gravity wave drag, the forcing for the semiannual seasonal component of AAM and the AAM response to global warming in an ensemble of coupled ocean-atmosphere model runs. CDC also monitors in real time the complete vertically integrated budget as part of its web-based maproom activities and distributes AAM and torque data to other researchers.

4.3.1 The Madden-Julian oscillation

A composite study of the MJO AAM signal was performed using 30–70 day filtered data and global AAM tendency as a linear regression "predictor". Large-scale eddies forced by tropical convection were found to play a dominant role in forcing the AAM response during northern winter (November-March). As these eddies move eastward within the asymmetric basic state, they produce a poleward movement of momentum transports. When this upper tropospheric momentum source reaches the subtropics, it induces a vertically deep mass circulation and a subtropical friction torque anomaly, which causes AAM to change. For the mountain torque, a combination of equatorial Kelvin waves, forced by convection over Indonesia and then impinging on the Andes and mass exchanges along the east slopes of the Himalayas and Rockies were found. The former is more directly linked with the MJO while the latter is a residual of large amplitude, ubiquitous torques induced by mid-latitude synoptic wavetrains. In fact, a case study of an individual MJO, where the mountain torque was 3x larger than the frictional torque, prompted a linear model investigation of the torques and their role in forcing intraseasonal AAM anomalies.

4.3.2 A linear model of global AAM

A simple Markov model of the three-component system comprised of total AAM, friction and mountain torque was developed. Statistical analysis of the observed data suggested AAM anomalies

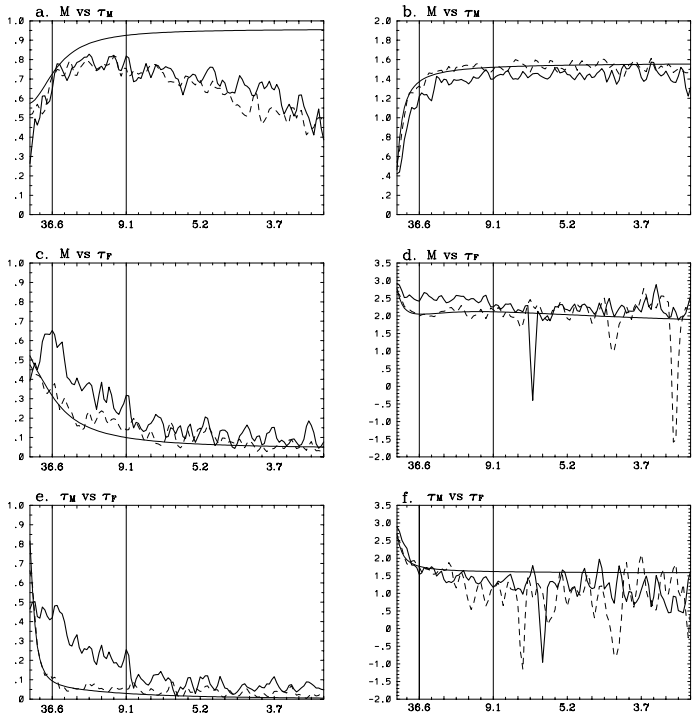

Fig. 4.9. Coherence squared (left column) and phase (right column) between the variables labeled at the top of each panel. Three curves are shown in each panel: the thick solid lines are for the observations, the smooth curves are the theoretical cross spectra and the dashed lines are based on output from a red noise model. The coherence squared and phase (in radians) are plotted as a function of Fourier frequency (cycles/366 days) with selected labels along the abscissa showing the corresponding period in days. A positive phase means the first variable labeled above each panel lags the second variable

are damped on a 30 day time scale by the friction torque and forced stochastically by a "white" mountain torque and a "red" friction torque. The resulting Markov model has variances and lagged covariances that compare favorably to the observations, although systematic differences representing approximately 20–30% of the variance also emerge (see **Fig. 4.9**). The most prominent differences are the greater coherence between the mountain and friction torque for 10–90 day periods in the observations (see **Fig. 4.9e**) and the excessive AAM variance at ~2π*30 days (the AAM decay time scale) in the modeled spectrum (not shown).

About 30% of the torques' variance in the 10–90 day band is coherent in the observed data versus <10% in the Markov model. In both the observations and the model, the friction torque leads the mountain torque. Physically the relation reflects primary forcing of AAM by the mountain torque and primary damping by the friction torque. It occurs weakly in the Markov model because the 30 day damping on AAM is "assigned to" the friction torque. For the MJO the same relation accounts for ~45% of the variance. The increase appears related to the timing of the torques' response to tropical convective forcing and adds to a background coherence, as given by the

Markov model. When linear inverse modeling is performed that accounts for feedback among the variables, the modeled AAM spectrum is improved somewhat and the skillful prediction of AAM is extended by 2 days.

The differences that remain after accounting for the linear feedbacks may be tied to limitations imposed by analyzing the global integrals. This naturally leads to three degrees-of-freedom for the simple Markov model which may be insufficient to describe the system accurately over a broad frequency range. In particular, the 30-day decay time scale for AAM blends interannual and intraseasonal variations that include both oscillatory and damped modes. Further improvement in the linear model requires analysis of a more complete set of variables that include deviations from the global mean.

4.3.3. Global torques and regional synoptics

The synoptic features associated with global mountain and frictional torques were also studied. The primary synoptic structure producing the mountain torque during northern winter is seen in **Fig. 4.10**. Growth of quasi-geostrophic disturbances upstream of the mountains is followed by downstream dispersion of energy across the mountains. At the surface, mass anomalies propagate southward, likely reflecting topographic Rossby wave activity forced by low level flow impinging on the mountain slopes. Zonal mean momentum anomalies produced by the torque are transported out of the latitude band of the mountain. This is accomplished partially by the quasi-geostrophic wave activity. The momentum is dissipated in adjacent latitude bands by the friction torque which responds to the upper level momentum source produced by the transports. The mass anomalies are consistent with quasi-geostrophic balance of the surface flow. The decay time scale of the global mountain torque is ~1.5 days, i.e., it is nearly white for daily data.

Synoptic developments are more complicated with the global friction torque which has a slower, 6 day decay time scale. Such low frequency forcing implies larger AAM anomalies and possibly enhanced predictability. Regression, using the global friction torque as a "predictor", reveals zonal mean momentum transports across 35°N during northern winter can initiate intraseasonal growth and decay of AAM anomalies. **Fig. 4.11** shows the composite evolution of 250 mb streamfunction and SLP anomalies when regressed on the friction torque. The streamfunction pattern at day –10 (**Fig. 4.11a**) has a ring of anticyclonic centers along 30–40°N, consistent with northward momentum transports across 35°N. The sequence which follows (**Figs. 4.11b-d**) shows wavetrains amplifying over east Asian and then North American orography, low pressure moving equatorward east of these mountains and pre-existing zonal mean easterly wind anomalies south of 35°N intensifying (**Fig. 4.11c**, mountain torque < 0) and then weakening (**Fig. 4.11d**, friction torque > 0).

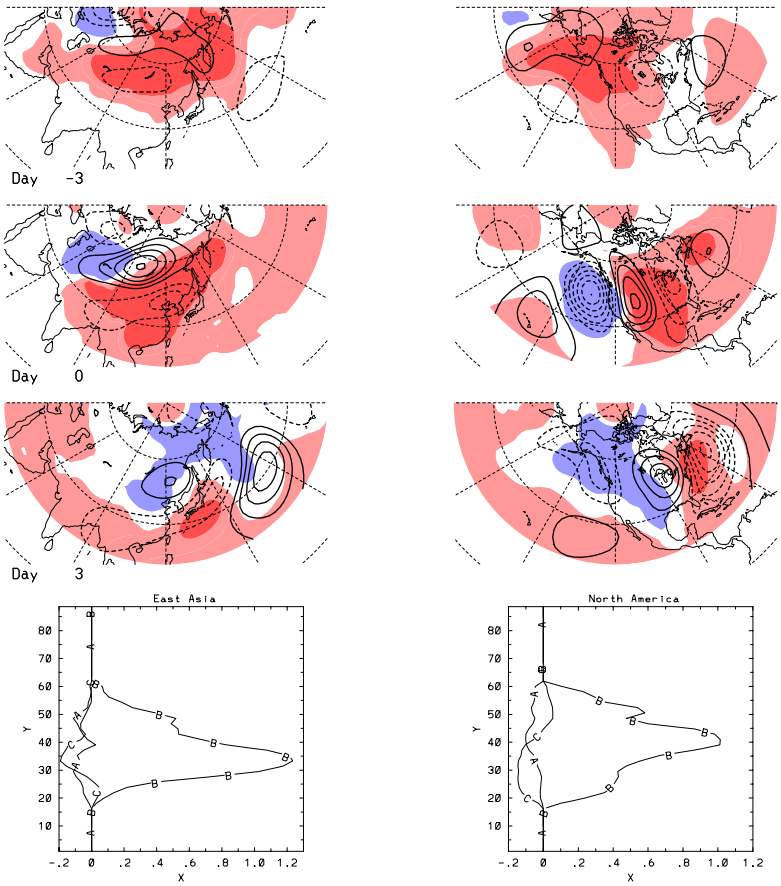

Fig. 4.10. The 250 mb streamfunction (contours) and sea level pressure (shading) anomalies that accompany a mountain torque over Asia (left column) and North America (right column) at days –3, 0, +3. The fourth panel in each column shows the mountain torque (Hadleys) as a function of latitude for each day. The curves labeled A, B and C correspond to days –3, 0 and 3 respectively.

The negative zonal mean mountain torque at days –2 to –6 is balanced by momentum transports that produce a momentum source in the orographic regions and a momentum sink in adjacent regions (or latitude bands). The atmosphere responds with easterly surface wind anomalies as it adjusts to the momentum sinks and these are supported geostrophically by lower pressure in the tropics and higher pressure in the extratropics (e.g., **Fig. 4.11c**). The mass and wind fields are especially strong over the Pacific sector where the 250 mb pattern projects onto the PNA. The positive friction torque counteracts the negative AAM tendency produced by the mountain torque leading eventually to a weak positive AAM anomaly. The 6-day decay time scale for the friction torque translates to a typical life cycle of an event lasting ~30–40 days. The close proximity to the MJO oscillatory time scale of 30–60 days suggests a good chance for interaction and feedback, both through the tropical convection and through the momentum and heat transports.

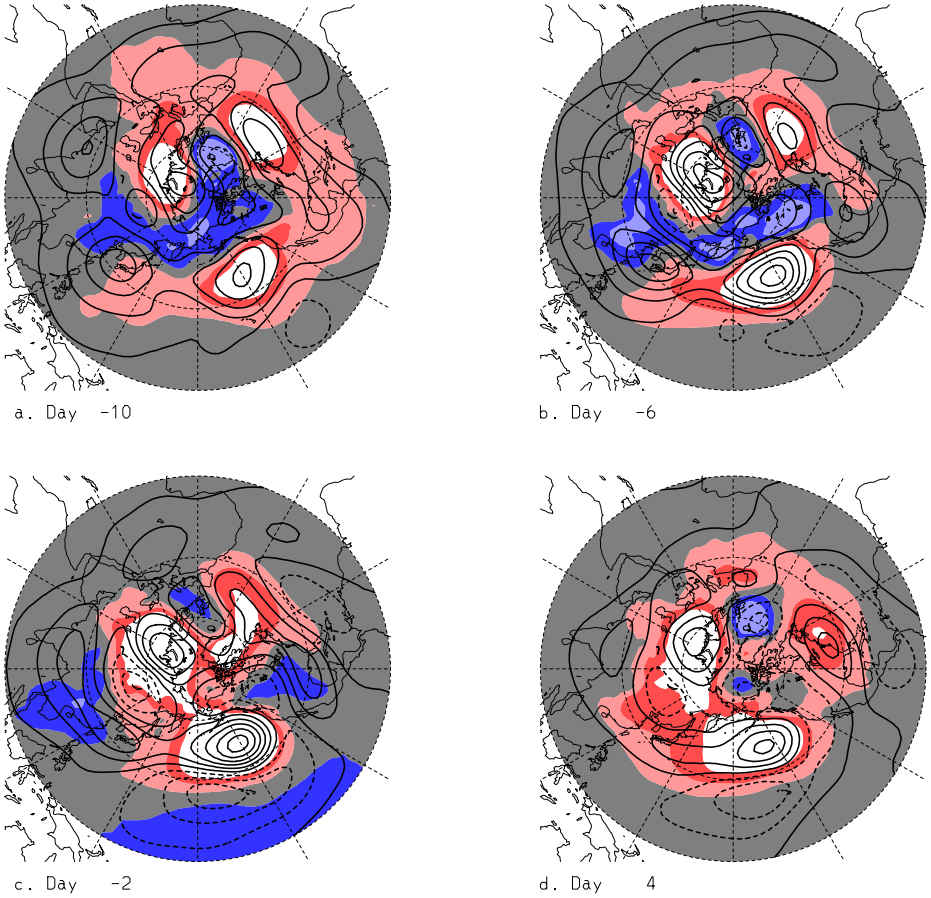

Fig. 4.11. The evolution of 250 mb streamfunction (contours) and sea level pressure (shading) anomalies that accompany the global frictional torque: a) Day –10, b) Day –6, c) Day –2 and d) Day +4. The red and white shading highlights positive SLP anomalies while the blue and gray shading highlights negative SLP anomalies.

4.3.4 Balance of global angular momentum in reanalysis data sets

The long-term balance of global angular momentum was examined in the NCEP reanalysis data set. In a perfect balance, the tendency of global atmospheric angular momentum should equal the total surface torque that comprises the three components of the mountain (T_M), friction (T_F), and gravity wave (T_G) torques. The gravity wave torque arises from the parameterization of subgrid-scale orographic gravity wave drag in the NCEP reanalysis model. Because T_F and T_G are not constrained by observation, a budget imbalance in the reanalysis data may exist. The extent of this imbalance reflects the realism of the assimilated data set. An extensive budget analysis of the NCEP data revealed a significant imbalance of angular momentum, on the order of −10 hadleys (negative value indicates that the torque is less than the tendency of angular momentum) for the annual mean. This imbalance is caused mainly by the gravity wave torque, as a removal of T_G reduced the annual-mean

budget imbalance to –2 Hadleys. Moreover, the greatest imbalance occurs in winter, when the magnitude of T_G reaches its maximum. **Figure 4.12** shows the seasonal and annual mean budget imbalance with (red) and without (blue) T_G. The budget imbalance in the reanalysis data strongly suggests deficiencies in the T_G parameterization scheme that may cause a loss of global angular momentum in real forecasts made with the NCEP GCM. This point was immediately confirmed by examining an extensive set of 8-day forecasts made with the NCEP reanalysis model. The rate of loss of global angular momentum in these medium-range forecasts is on the same order of magnitude as the budget imbalance deduced from the reanalysis data. These results constitute a critical examination of the realism of the NCEP reanalysis data. They also point to the potential negative impact of the gravity wave drag on numerical weather/climate prediction. Finally, the T_G in the ECMWF reanalysis data is very similar to its counterpart in the NCEP reanalysis in its magnitude and temporal variability. It is very likely

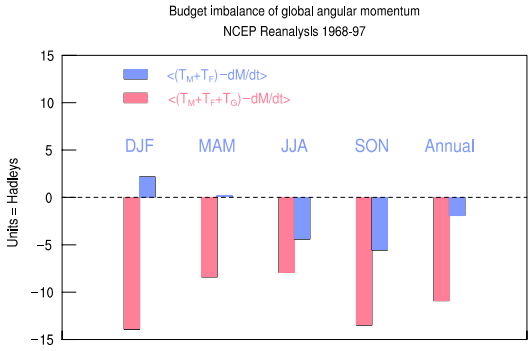

Fig. 4.12. The budget imbalance of global angular momentum for seasonal and annual means, based on NCEP reanalysis data from 1968–1997. The imbalance estimated with and without gravity wave drag are shown in red and blue. Units in hadleys.

that the same problem of budget imbalance of angular momentum, caused by T_G, also exists in the ECMWF reanalysis data and the ECMWF GCM.

4.3.5 Impact of parameterized gravity wave drag on GCM weather/climate prediction

This study was inspired by the budget analysis of global angular momentum described above. After finding the potential problem with the orographic gravity wave drag (GWD) in degrading the balance of global angular momentum, the impact of GWD on weather/climate prediction was examined by performing a series of extensive GCM simulations with varied strength of GWD. The GCM used was a recent version of the NCEP global forecast model. The numerical experiments comprised 9 sets of medium-range (2 week) forecasts, each using a different value of the surface GWD parameter ranging from 0 (no GWD) to 2 x GWD (twice the standard value used in the original NCEP model). Each set of forecasts, in turn, consisted of 20 runs from a series of initial conditions 5 days apart from the 1997–98 winter. The results showed a clear degradation of the forecasted global angular momentum as the strength of GWD increases, consistent with our previous budget analysis. At the same time, GWD did provide some improvement in the forecast of the local zonal mean angular momentum in the midlatitude of the Northern Hemisphere, a characteristic that has been emphasized by proponents of GWD parameterization.

Thus, increasing the GWD in the model introduces opposite effects in the errors of the global and local angular momentum. This is most clearly illustrated in **Fig. 4.13a**, the forecast error of global angular momentum (filled circles) and the area-weighted RMS forecast error of local angular momentum (open circles) for the Northern Hemisphere as functions of the GWD parameter. Each circle represents the error at day 10 averaged over 20 forecasts. **Figure 4.13b** is similar to **Fig. 4.13a**, but with the error normalized by the grand average across the nine parameter values of GWD. The robustness of the result is demonstrated by the smallness of the difference between the 20- (black) and 10- (red) forecast averages. The detailed structure of the local forecast error of zonal mean zonal wind as a function of the GWD parameter was

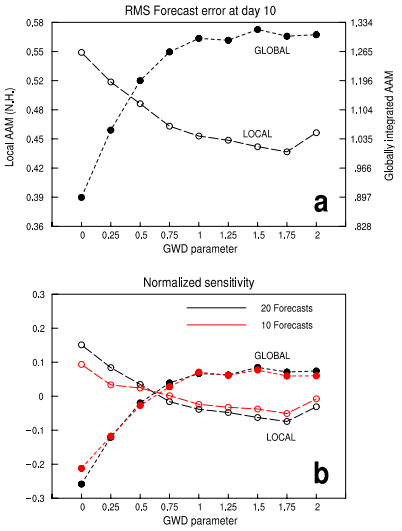

Fig. 4.13. (a) The forecast errors of global relative angular momentum (filled circles) and local angular momentum (open circles) at day 10, averaged over 20 forecasts, as functions of the GWD parameter. Units in AMU (1 AMU = 10^{25} kg m^2 s^{-1}). (b) Same as (a), but normalized by the average of all nine points in each curve. Red curves are the errors deduced from 10 forecasts.

investigated. It is found that in the absence of GWD the forecasted zonal wind is too strong in the midlatitude but too weak in the subtropics of the Northern Hemisphere. The two local errors partially cancel each other such that the error in the global angular momentum appears to be small. The effect of GWD is to partially reduce the local error in the N.H. midlatitudes without affecting other areas. Thus, the stronger the GWD, the greater the negative bias in the forecasted global angular momentum. These results indicate that the GWD parameterization scheme is not consistent with the balance of global angular momentum. Research into alternative parameterization schemes for the mechanical dissipation in the GCM that is capable of correcting both local and global errors of angular momentum in the same direction is warranted.

4.3.6 Annual and semiannual cycles of atmospheric angular momentum

The mechanism for the semiannual oscillation of atmospheric angular momentum was examined. Upper-tropospheric winds, whose angular momentum is an excellent proxy of the vertically-integrated angular momentum, were used. The observed seasonal cycle of the zonal wind or angular momentum is dominated by its first two (annual and semiannual) harmonic components (**Fig. 4.14, top panel**). The seasonal variation of the rotational component (the part that contributes to global angular momentum) of the upper-level winds was diagnosed in a nonlinear upper-tropospheric vorticity-equation model with specified diver-

gence (Rossby wave source) and transient eddy forcing. The divergence forcing is the more important of the two, especially in the Tropics and subtropics, where it is associated with tropical heating and cooling. Given the harmonics of the forcing, the model predicted the harmonics of the response, that is, the vorticity, from which the harmonics of angular momentum can be calculated. This procedure itself is an innovative way of diagnosing a temporally periodic phenomenon. It can, in principle, be generalized to the three-dimensional atmosphere or a coupled atmosphere-ocean system. The surprising but clear conclusion from our diagnosis is that the semiannual harmonic of atmospheric angular momentum arises more as a nonlinear response to the first (annual) harmonic of divergence forcing than as a linear response to the second harmonic of divergence forcing. To illustrate, the bottom panel of **Fig. 4.14** shows the response of global relative angular momentum (first three harmonics) to a specified divergence forcing that contained only the annual mean plus the first harmonic. In this case, in the complete absence of a second-harmonic forcing, the second harmonic response resembles that observed in both amplitude and phase. Another case with specified second harmonic (but not first harmonic) forcing failed to produce a realistic response in the angular momentum. Thus, the semiannual harmonic of solar radiative forcing arising from the sun crossing the equator twice a year may not be as important as previously thought in generating the semiannual cycle of atmospheric angular momentum. The result is a clear demonstration that external forcing at one frequency can produce primary atmospheric response at a different frequency. Since it has been shown previously that significant errors exist in the semiannual harmonic of angular momentum or zonal wind in GCM simulations, the findings point to the possibility that these errors may be related to the first harmonic of the radiative/diabatic forcing as well as the detailed treatment of the interaction between this forcing and the annual harmonic of the tropical circulation.

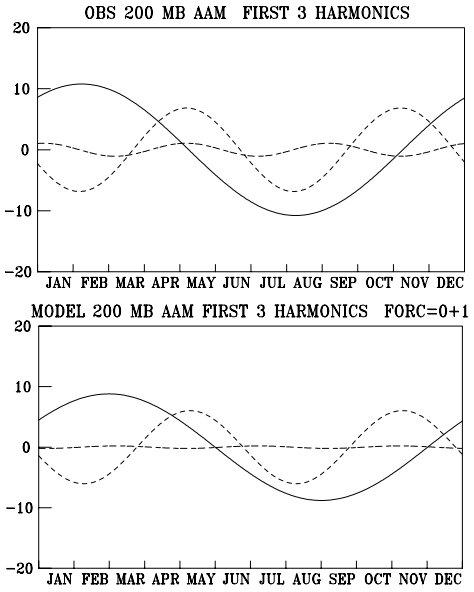

Fig. 4.14. The observed (upper) and model simulated (lower panel) first three harmonics of relative angular momentum at 200 mb. In the simulation only the annual mean and first harmonic of divergence forcing are applied to the vorticity equation model.

4.4 Air-sea interaction related to the MJO

There is growing interest in the role that air-sea interaction may play for the dynamics of the Madden-Julian oscilla-

tion. Such interest has been motivated by the poor performance of GCMs in simulating and forecasting the MJO. Models with prescribed SST typically produce MJOs that move eastward too fast, are too weak, and have incorrect seasonality. Field programs, such as TOGA COARE, have revealed local swings in SST in excess of 1°C in association with passage of the MJO across the warm pool of the Indian and western Pacific Oceans. The forcing and importance of these anomalies both within the MJO cycle itself and as a link with low frequency variations are subjects of CDC research.

4.4.1 The MJO cycle

Comparison of the observed SST tendency and the net surface heat flux into the equatorial western Pacific indicates that surface heat flux forcing by the MJO is likely responsible for the observed intraseasonal SST variations. A detailed study of the surface heat fluxes associated with the MJO indicates the dominance of short wave radiation and latent heat flux. The structure of the MJO is such that minimum surface short wave radiation occurs just prior to maximum latent heat flux. Thus these two fluxes act in concert to cool the ocean after the passage of the convective-windy phase of the MJO. Similarly, increased short wave radiation and reduced latent heat flux act to warm the ocean during the clear-calm phase of the MJO.

The dominance of one dimensional processes for controlling the SST variations associated with the MJO has been demonstrated using a grid of one-dimensional mixed layer models. Each grid was forced with observed surface fluxes for 10 well-defined MJO events. The composite of model output (not shown) indicates that surface heat flux forcing is responsible for the observed intraseasonal SST variations across the equatorial Indian and western Pacific Oceans. This result is at odds with point measurements made during TOGA COARE, which suggests a significant role for horizontal advection. This issue was addressed by repeating the mixed layer model experiments using an Ocean GCM. Again, the observed intraseasonal SST variation produced by the composite MJO was simulated. But, analysis of the role of horizontal advection (**Fig. 4.15**) emphasizes the dominance of surface heat flux forcing. While horizontal advection is locally large (as in TOGA COARE), it is incoherent on the scale of the MJO.

The potential impact of intraseasonal SST anomalies, induced by the MJO, on the dynamics of the MJO was investi-

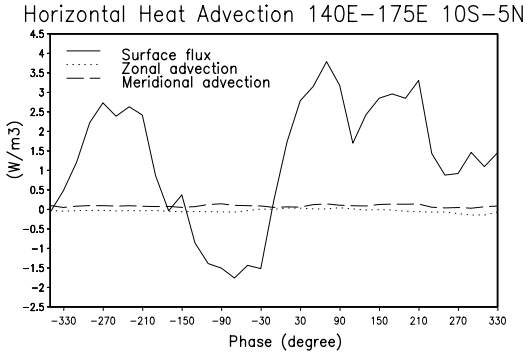

Fig. 4.15. Composite area average (140°E–175°E, 10°S–5°N) zonal (dotted line) and meridional (dashed line) heat advection (W m^{-3}) of upper 10 m and the surface heat flux divided by 10 m (thick line). Positive values indicate warming.

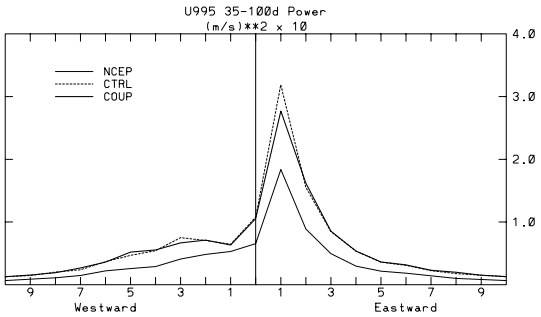

Fig. 4.16. Wavenumber spectra for the surface zonal wind from the NCEP-NCAR reanalysis (thin curve), the control run (dashed curve), and the coupled run (heavy curve). Power was integrated for periods 35–90 days and averaged for each latitude between 15°N and 15°S.

gated in a GCM coupled to a grid of one dimensional mixed layer models. Simulating the ocean with a mixed layer model is appropriate for this study, as indicated by the above heat budget studies. In the particular GCM used for this study, coupling to an active mixed layer had very little impact on the model's MJO (**Fig. 4.16**). Unfortunately, due to a poor simulation of the surface structure of the MJO, the model was unable to reproduce the observed coherent eastward propagation of SST. The poor simulation of the surface structure of the MJO stems from both a poor simulation of the mean climate of the warm pool and an improper phasing of short wave radiation and latent heat flux. Thus, it remains an interesting question as to the role of intraseasonal SST anomalies for the dynamics of the MJO, and, for instance, whether prediction of intraseasonal SST is necessary for successful prediction and simulation of the MJO.

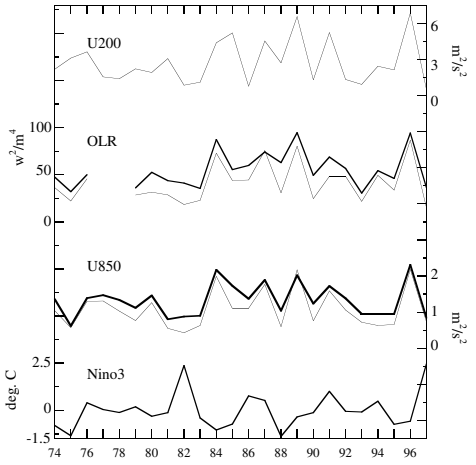

Fig. 4.17. Time series of (top to bottom) $[u_{30\text{-}90d}]^2$, $[OLR^2_{EOF}]$ (dark curve) and $[OLR^2_{EWVS}]$, $[U^2_{EOF}]$ (dark curve) and $[U^2_{EWVS}]$, and Niño3 SST averaged during Nov.–Mar. The units for OLR variance (on left) are $W^2\ m^{-4}$, for zonal wind variance (on right) are $m^2\ s^{-2}$, and for Niño3 SST (on left) are °C.

4.4.2 Interannual variation of MJO activity

The level of MJO activity in the Tropics is observed to vary widely from year to year. Understanding this interannual variability is of practical importance because of the role the MJO plays in the Australian and Indian summer monsoons, in forcing oceanic Kelvin waves that dominate the variability of the thermocline in the equatorial eastern Pacific, and the possible role that the MJO may play in the onset and evolution of ENSO. A detailed analysis of the interannual variability of the MJO during winter reveals little relationship between the overall level of activity and SST, including the state of ENSO (**Fig. 4.17**). Recent analyses of ensembles of GCM experiments have arrived at the same conclusion: most of the year-to-year variability of the level of MJO activity during win-

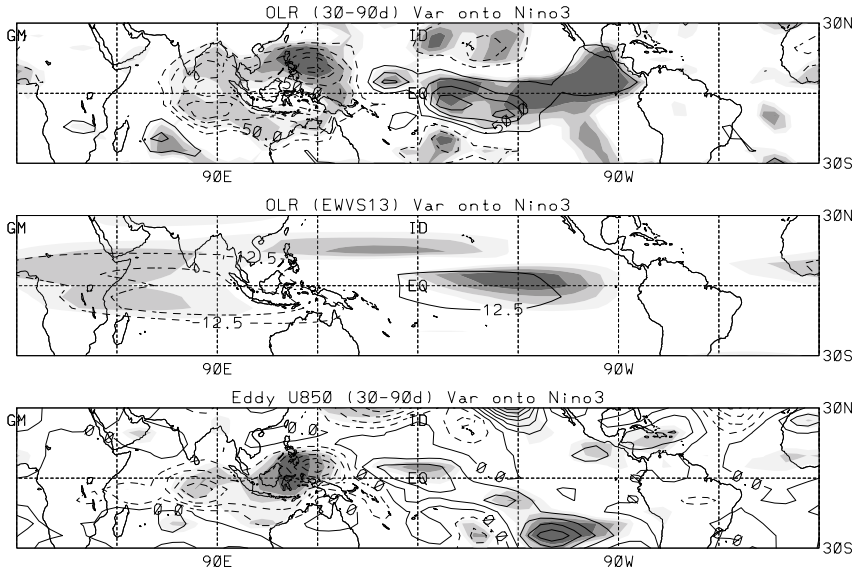

Fig. 4.18. (a) Regression of Nov.–Mar mean 30–90 day filtered OLR variance onto Niño3 SST. (b) Regression of OLR_{EWVS} onto Niño3 SST. (c) Regression of 30–90 day filtered 850-mb zonal wind variance on Niño3 SST.

ter is unrelated to boundary forcing and is thus unpredictable.

On the other hand, MJO activity is observed to shift eastward during El Niño (**Fig. 4.18**). This eastward shift may have important dynamical consequences, especially at the onset of warm events. Furthermore, while the contemporaneous correlation between wintertime (DJFM) west Pacific SST and wintertime global MJO activity is small, there is a strong correlation when west Pacific SST leads MJO activity by 1 season. **Figure 4.19** shows a scatter plot of MJO activity in winter versus SST anomaly averaged over the west Pacific in the northern fall (SON). The lag correlation depicted is consistent with the synoptic observation that an expanded warm pool promotes strong MJO activity. The weak contemporaneous correlation in winter reflects the cooling effect of enhanced MJO activity on local SSTs. Warm west Pacific SSTs also precede the onset of El

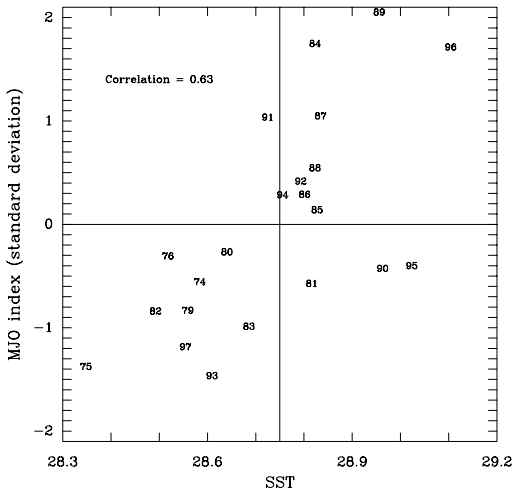

Fig. 4.19. Northern fall mean SST (°C) plotted against MJO variance averaged over the following winter. Values have been averaged over 130°E–180°E, 15°S–15°N. MJO variance is calculated from the spectral power of eastward propagating zonal wavenumbers 1–6 and periods 35–90 days. The variance of each season has been normalized by the standard deviation of wintertime variances between 1974 and 1997.

Niño, which might lead one to infer a relationship between strong MJO activity and the onset of El Niño. However, of the three winters with the strongest MJO activity, only the winter of 1996–97 (year 96 in the figure) preceded a strong El Niño.

4.4.3 MJO and ENSO

Previous studies have suggested that intraseasonal variations of convection contribute to interannual variations in the tropical Pacific by acting as a triggering mechanism for El Niño. This speculation has increased recently because the 1997–98 El Niño, arguably the strongest of the century, followed exceptionally strong MJO activity during the winter of 1996–97. During the winter of 1996–97 there were two strong MJO events that could have contributed to the evolution of the 1997–98 El Niño. The first occurred during December 1996 and was accompanied by substantial cooling of the west Pacific, initiating a long-term cold anomaly there. The second occurred during February–March 1997 and was accompanied both by cooling in the west Pacific and warming in the central Pacific. The warming in the central Pacific was particularly important. After that warming, central Pacific SSTs remained warm for the next year and convective activity migrated to the central Pacific, signaling the onset of a very strong and rapidly developing El Niño. To help elucidate the potential role of MJO activity for the onset of El Niño, dynamical interactions were examined in the upper ocean that led to the important SST changes in the winter of 1996–97.

SST fluctuations that occurred in the west Pacific (**Fig. 4.20a**) during convective episodes in December 1996 and February 1997 (shaded periods) were, for the most part, forced by surface flux variations (**Fig. 4.20b**). Surface cooling was initiated by the reduction of SW surface fluxes due to enhanced cloud cover. Later, evaporative cooling during eastward wind anomalies reinforced that cooling. In February 1997, temperature advection (**Fig. 4.20c**) by ocean currents was also important for the SST perturbation; off-equatorial upwelling, through an anomalously large vertical temperature gradient, contributed substantially to west Pacific cooling.

During late March and early April 1997, central Pacific SSTs (**Fig. 4.20d**) warmed in response to an oceanic Kelvin wave that was forced during the February MJO. That warming was primarily due to zonal temperature advection (**Fig. 4.20e**), promoted by strong eastward currents along with an east-west temperature gradient. After the passage of the Kelvin wave, zonal currents remained slightly eastward because trade winds (**Fig. 4.20f**) did not resume their pre-Kelvin wave strength. In addition, the east-west SST gradient was reduced after the Kelvin wave. As a result, temperature advection was negligible after the Kelvin wave, and SST continued to warm due to the positive surface heat flux that is typical for the region. The zonal current variation that is responsible for the temperature advection is forced, in part, by a local wind-stress fluctuation. So, if the MJO did contribute to this important SST warming through nonlinear interac-

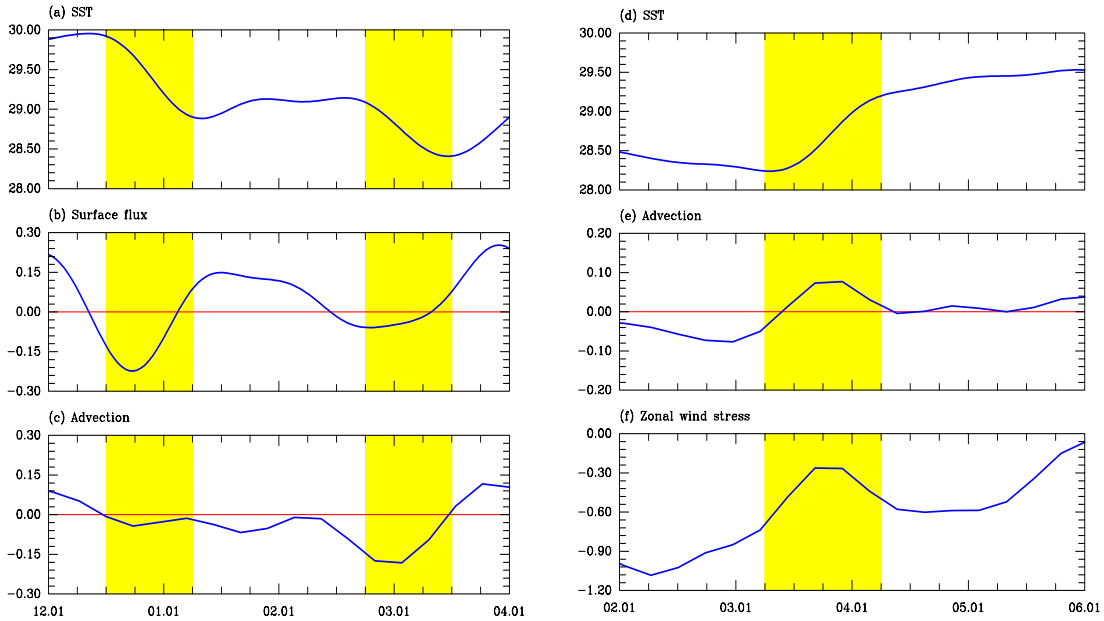

Fig. 4.20. SST and upper-ocean quantities averaged over the top 50 m. On the left are shown values in the west Pacific (10°S–10°N; 130°E–150°E) for December 1996 through March 1997 of: (a) SST (K), (b) net surface heat flux (K week^{-1}), and (c) temperature advection by ocean currents (K week^{-1}). On the right are shown values in the central Pacific (10°S–10°N; 160°W–180°W) for February through May 1997 of: (d) SST, (e) temperature advection by ocean currents (K week^{-1}), and (f) zonal wind stress (dyne cm^{-1}). Shaded regions indicate time periods of rapid SST changes.

tions, then those interactions involve the coupling of atmospheric and oceanic dynamics.

4.5 The South American Program

A large dataset of daily rainfall observations over South America culled from sources in several countries has allowed an examination of precipitation patterns on that continent with unprecedented spatial and temporal resolution. A comparison with rainfall estimates from other datasets that employ a combination of satellite and some gauge data has shown that the two estimates generally are within 10% of the rain gauge only estimates at 2.5° resolution for climatologies of a season or more. On the other hand, at some locations within the Amazon, estimates of the annual cycle of rainfall from gauge observations and outgoing longwave radiation are several months out of phase.

4.5.1 Seasonal rainfall relation with SST

Interannual variability of seasonal rainfall in the Brazilian Amazon basin has been studied in the context of its relationship to sea surface temperatures in the tropical Pacific and Atlantic oceans. Simultaneous linear correlations reveal strong relationships, but the rainfall patterns are of regional scale.

With a few exceptions, the largest (absolute) correlations between 3-month seasonal rainfall and SST are found during the season of transition between wet and

dry or between dry and wet regimes. In a few cases there are large simultaneous correlations entirely within the dry season, but large correlations are never found entirely during the wet season. In the Pacific, large correlations are always confined to the eastern equatorial region, and warm SSTs are always associated with a deficit of rainfall. In the Atlantic, correlations are usually positive, and centered in the near-equatorial southern ocean.

It is hypothesized that during the transition seasons an important contributor to the SST control on seasonal totals is its influence on the timing of the rainy season onset or end. That influence appears to be stronger than the SST influence on the rainy season rain rate. This is illustrated by **Fig. 4.21**. **Figure 4.21a** shows the simultaneous correlation between April-June rainfall in the eastern equatorial Amazon and SST. The area chosen for the rainfall average is somewhat unusual in that it exhibits large correlations with both proximate oceans. When the ending date of the same area average of rainfall (with a climatological ending date of 13 June) is correlated with SST (**Fig. 4.21b**) the pattern that emerges is similar and of the same sign, suggesting that in this region the SST role in the timing of onset plays a role in the SST relationship with seasonal total rainfall. Further, when SST is correlated with the rainy season rate of rainfall (defined as the average daily rainfall from 1 April to the annually varying end of the rainy season), only weak correlations are evident (**Fig. 4.21c**). Thus it appears that the most important influence of SST in

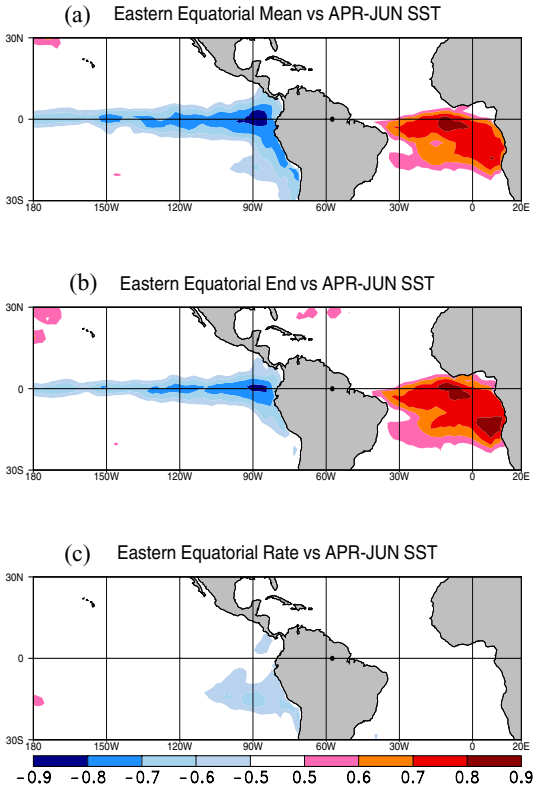

Fig. 4.21. Correlation between April-June SST and (a) April-June mean rainfall in eastern equatorial (average of 20 stations from 2.5°S–2.5°N, 60°W–55°W) Amazon, (b) eastern equatorial rainy season ending date, and (c) far eastern rain rate calculated from 1 April through end of rainy season. Included are years 1976–1997.

determining calendar season total rainfall is through its influence on the timing of the rainy season, rather than on the intensity of rainfall during the rainy season itself.

A battery of atmospheric general circulation models presently are being tested to determine whether these models produce a realistic onset over monsoonal South America when forced by realistic and evolving SSTs. The observed skill these models exhibit in simulating seasonal anomalies over equatorial South America also is being evaluated to determine

the role of model onset in contributing to that skill.

4.5.2 Intraseasonal variations in the SACZ

Mechanisms associated with subseasonal rainfall variability in the South Atlantic convergence zone (SACZ) have been examined. The SACZ arguably is the most important meteorological feature of South America, because it exhibits large variability at many time scales and its mean position passes over the most densely populated Brazilian states of São Paulo and Rio de Janeiro.

Correlations between submonthly (2–30 day band-pass filtered) OLR in the vicinity of the SACZ and 200 mb streamfunction reveal the preferred path of wave energy impinging on the SACZ to be Rossby waves from the midlatitudes of the Southern Hemisphere. Episodes of enhanced convection within the SACZ, indicated by negative OLR anomalies, occur at the leading edge of upper-level troughs propagating into the region. The corresponding pattern at 850 mb reveals that the disturbances are nearly equivalent barotropic west of South America, but tilt westward with height in the region of the SACZ. Negative low-level temperature anomalies lie to the southwest of the convection. The results are consistent with baroclinic development along an associated cold front. It also appears that the SACZ forms when the northwesterly flow associated with a low-level trough is able to tap moisture from the Amazon.

4.5.3 Climatology of extreme precipitation events

The climatology and interannual variability of heavy, or 'extreme', precipitation events in the state of São Paulo, Brazil were studied. An extreme event is counted at each station when daily rainfall exceeds a certain percent of its seasonal or annual mean. It is found that they occur mainly from November–March (the season during which the SACZ is most active) and that there is a distinct interannual variation in their number. The count of extreme events is not well correlated with total seasonal precipitation. The relationship between extreme events and activity in the SACZ is therefore not obvious. From October–

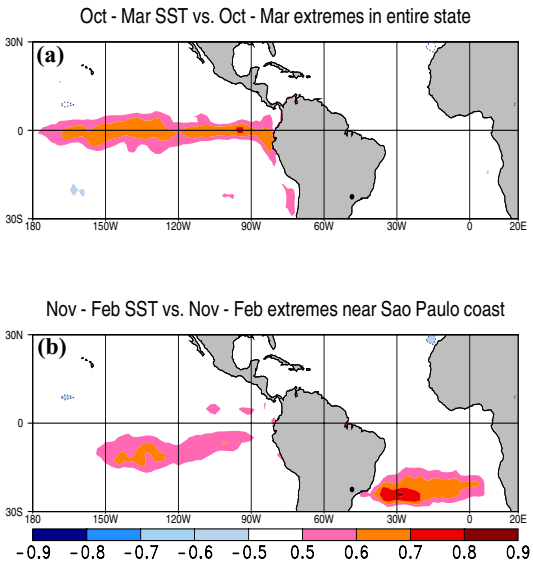

Fig. 4.22. (a) Simultaneous correlation between October–March SST and count of extreme events for during same period in state of São Paulo. An extreme event is counted at each station when daily precipitation exceeds 12% of October–March climatological total. Calculations are for period 1976–1977 to 1994–1995. (b) As in (a) except that correlation is from November–February, stations from which extreme events are counted are in coastal São Paulo, and the 16% level is used as threshold.

March, the interannual count of extreme events in the entire state is correlated positively with sea surface temperature anomalies in the equatorial Pacific from near the dateline to the west coast of South America (**Fig. 4.22a**). The interannual count at stations near the Atlantic coast from November–February is correlated positively with SST anomalies in the Atlantic Ocean near the latitude of São Paulo (**Fig. 4.22b**). In both cases the relationship between SST and mean precipitation is weak. The associations are confirmed with composites and rank correlations.

4.6 Use and evaluation of the NCEP/NCAR reanalysis

4.6.1 Diurnal modes of variability in reanalysis datasets

The diurnal variability of the diabatic forcing terms and thermodynamic variables in the NCEP and ECMWF reanalysis data sets was investigated. This study aimed to examine the realism of the reanalysis data on very short time scales. Diurnal variability is expected to reveal differences between the two reanalysis data sets because of differences in the physical parameterizations in the two reanalysis models. To narrow the scope of the investigation, we focused on the diurnal (24-hour period) mode of variability in both data sets. **Figure 4.23** shows the amplitude (contours) and phase (arrows, pointing to the maximum; upward = midnight, downward = noon local time) of the diurnal mode of precipitation rate for the NCEP (top) and ECMWF (bottom) reanalyses. The diurnal mode of precipitation was found to be significantly different in the two data sets, especially over the central and western Pacific Ocean. The NCEP precipitation has a higher amplitude over the Pacific Ocean. Further analysis of the diurnal cycle (including all harmonics) of precipitation showed that the NCEP precipitation in the western Pacific possesses an early morning maximum (visible in the **top panel of Fig. 4.23**), consistent with in situ observation from TOGA COARE. This characteristic is not well represented in the ECMWF reanalysis data. The diurnal components of all the terms in the column-integrated thermodynamic equation was analyzed for the NCEP reanalysis. Over the ocean, the diurnal tendency of temperature is balanced mainly by the nearly-uniform net (short wave plus long wave) radiative forcing, latent heating (which possesses a similar pattern as precipitation), and adiabatic cooling/heating due to vertical motion. Thus, the diurnal tendency of temperature is substantially influenced by the physical parameterization pertinent to the generation of diurnal precipitation. An important implication of this project is that the error in the short-term variability of a model variable could be rectified into a bias in the long-term climatology. Since the diurnal precipitations in the NCEP and ECMWF reanalyses are significantly different, such a possibility deserves further investigation.

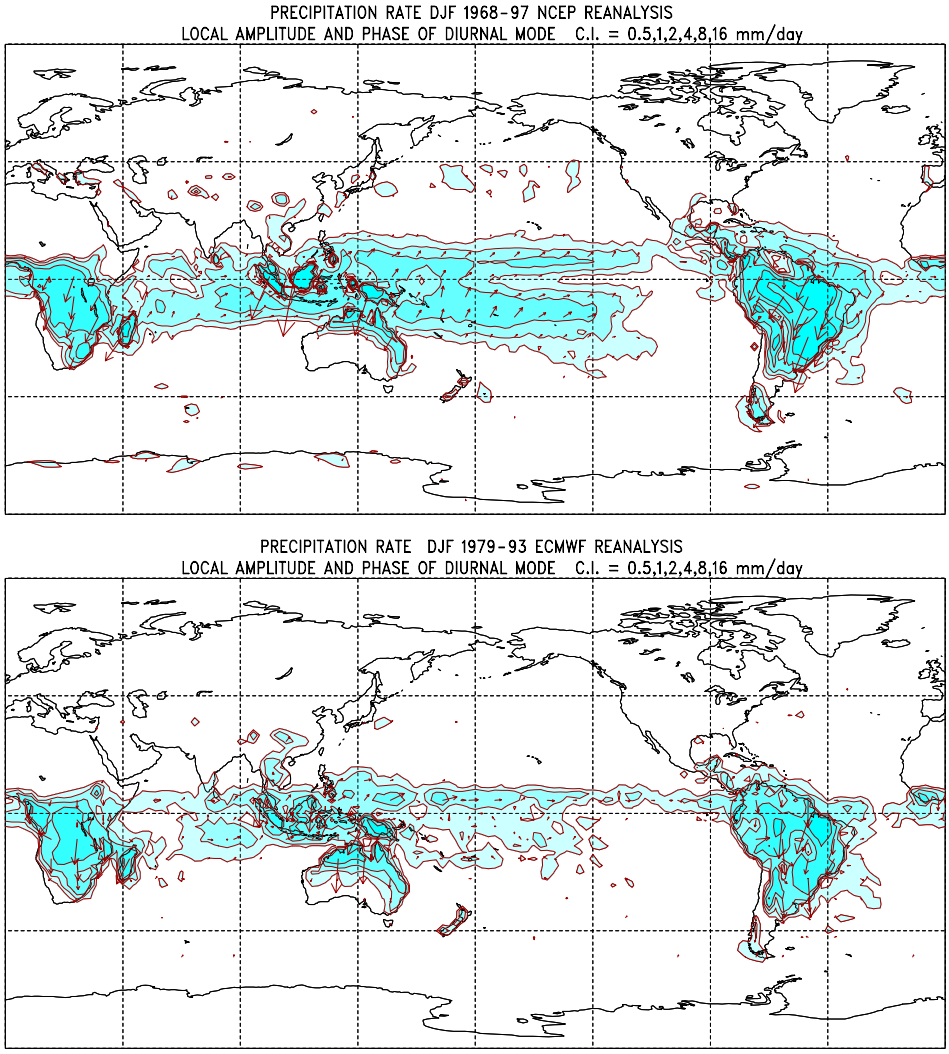

Fig. 4.23. The diurnal (12-hour period) component of precipitation estimated from the NCEP (top) and ECMWF (bottom) reanalyses. The amplitude of precipitation rate is shown in contours, with contour levels 0.5, 1, 2, 4, and 8 mm/day. Areas with amplitude greater than 0.5 mm/day are colored. The phase of the diurnal harmonic is indicated by an arrow pointing to the time of the maximum, upward = 12 AM, downward = 12 PM local time. The analysis is based on winter (Dec.–Feb.) data.

4.6.2 Tropical heating and the chi-problem

To understand the interactions between the tropics and the extratropics, it is important to determine accurately both the climatology and variability of atmospheric heating in the tropics. However, since there are no "heating meters" that may be employed for this purpose, heating is often estimated as a residual in the thermodynamic budget. This means that the vertical profile of horizontal wind divergence must be well specified. To gauge the accuracy of this critical field, we carried out an assessment of the mean

structure and variability of deep convection over the tropical eastern Indian and western Pacific oceans as provided by three different reanalysis datasets for northern winter (DJF) 1980–93. The datasets were generated at the National Centers for Environmental Prediction (NCEP), NASA's Goddard Laboratory for Atmospheres, and the European Center for Medium-range Weather Forecasts (ECMWF). Rainfall, Outgoing Longwave Radiation (OLR), and 200 mb wind divergence fields from the three datasets were compared with one another and with satellite observations.

The internal consistency of the datasets is high, in the sense that the geographical extrema of the rainfall, OLR and divergence fields correspond closely to one another. On the other hand the external consistency, i.e. the agreement between the datasets, is so low as to defy a simple summary. Indeed, the differences are such as to raise fundamental questions concerning: (1) whether there is a single or a split ITCZ over the western Pacific ocean with a strong northern branch, (2) whether there is more convection to the west or the east of Sumatra over the equatorial Indian ocean, and (3) whether there is a relative minimum of convection near New Guinea. Geographical maps of interannual and intraseasonal variances also show similar Order 1 uncertainties, as do regressions against the principal component time series of the Madden-Julian Oscillation (MJO). The annual cycle of convection is also different in each reanalysis. Overall, the ECMWF reanalysis compares best with observations in this region, but it too has important errors.

Finally, we showed that although the 200 mb divergence fields in the three datasets are highly inconsistent with one another, the 200 mb vorticity fields are highly consistent. This reaffirmed the relevance of diagnosing divergence from knowledge of the vorticity using the method described in Sardeshmukh (1993). This would yield divergence fields from the three datasets that are not only more consistent with each other, but also more consistent with the 200 mb vorticity balance. This iterative procedure was applied to the NCEP/NCAR Reanalysis wind fields (1969–1999) to minimize the vorticity budget residual, and the divergent circulation was further constrained to satisfy the large-scale mass budget. Enforcing dynamical consistency on the divergent circulation had a noticeable effect on the strength, position, and variability of the diagnosed heating extrema. Sub-tropical cooling was also stronger in the chi-corrected dataset. In the tropics, the chi-corrected heating fields showed substantially greater variability, on time scales ranging from daily to seasonal, than the unmodified fields. Vertical profiles of chi-corrected diabatic heating and moistening for the northern winter of 1992–93 compared better with the profiles from observational COARE data than did the profiles from the original reanalyses. Monthly averages of this data have also been made available in atlas form on a CDC web page, http://www.cdc.noaa.gov/chi/.

4.6.3 Tropical surface fluxes

As a by-product of work on the MJO-induced surface fluxes, the reliability of the surface fluxes depicted by the NCEP/NCAR Reanalyses was assessed. On intraseasonal time-scales, fluxes that depend primarily on surface wind variations (e.g., stress and latent heat flux) agree more favorably with direct observations than fluxes that are largely dependent on fluctuations of convection (e.g., surface shortwave radiation and freshwater flux). This is demonstrated for a composite MJO (**Fig 4.24**). While the coherent eastward propagation of stress and latent heat flux are well depicted in the reanalyses, the composite short wave radiation exhibits less than half of the observed amplitude. The direct use of the reanalysis fluxes in studies of the heat budget of the warm pool is thus discouraged. Composite variations of wind stress and latent heat flux from the reanalyses agree better with observations such as during TOGA-COARE.

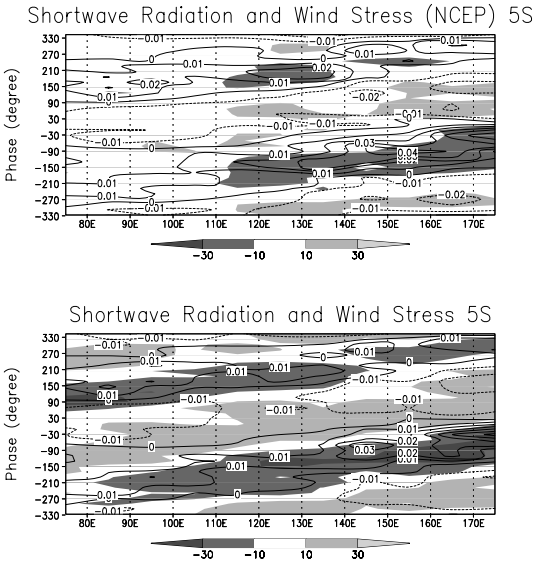

Fig. 4.24. Composite shortwave radiation anomaly (shading) and zonal stress (contours) from NCEP reanalyses (upper panel) and estimates from Shinoda et al. (1998) (lower panel) for the 10 MJO events defined by Shinoda et al. (1998). The vertical axis indicates the phase based on the EOFs of OLR. One cycle is approximately 50 days. The contour interval for stress is 0.01 N m^2 and the shading levels for shortwave radiation are 20 W m^2 with the first shade at +10 and –10 W m^2. Linear trends along the vertical axis are removed.

EPILOGUE

Identifying the role of different physical processes in evolving climate anomalies is a basic component of CDC's research, and is complementary to research to ascertain that physical processes are properly represented in climate models. All five areas of physical process research (Sections 4.1–4.6) will continue to emphasize physical connections and their variations across a broad range of time scales. For example, the linear AAM model does a good job with intraseasonal variations but not with interannual variability. Stochastic (El Niño) and oscillatory (the QBO) interannual modes can be included in the model and their interactions with intraseasonal variations examined. Indeed, synoptic analyses indicate a link between the transport of momentum across 35N by an interannual mode such as ENSO and excitation of an intraseasonal mid-latitude mode linked with the mountains. Such potential scale interactions of the large scale circulation are of interest both scientifically and for monitoring and prediction purposes.

Air-sea interactions studies related to the MJO will continue with a range of cou-

pled models. One focus will be on proper simulation of the seasonal cycle in the tropics, especially over the Indian Ocean. Model experiments will be designed to test the role of air-sea interaction on the character of monsoonal precipitation fluctuations over South America, including its potential predictability.

Parameterizations of subgrid scale processes in clouds will be implemented in the GFDL Flexible Modeling System, making it more usable for diagnostic studies, and possibly improving its climate. Moist convective parameterizations will be developed and tested to account for the observed variations found across a broad range of time scales and physical environments. Issues of continued interest for parameterization schemes include: the role of cumulus friction simulated in cloud-resolving models, the non-equilibrium behavior of the diurnal cycle of convection over tropical land masses (**Fig. 4.4**), and the convective organization on relatively small scales (e.g., **Fig. 4.2**) by gravity waves.

Future research in these areas will benefit from new global datasets, from observations made during field projects, and from new climate model datasets. Improving the understanding of basic physical processes will remain essential for diagnosing current climate events, and for evaluating predictions of atmosphere and coupled ocean-atmosphere phenomena.

C*ontributed by: J. Bergman, H. Hendon, H.-P. Huang, B. Liebmann, B. Mapes, M. Newman, R. Pincus, P. D. Sardeshmukh, T. Shinoda, and K. Weickmann.*

CHAPTER 5

Decadal Climate and Global Change Research

The Climate Diagnostics Center contributes to understanding the variations in Earth's climate system on decadal to centennial time scales. Research includes process and model simulation studies to elucidate the relation between changes in the atmosphere and those in the ocean. CDC scientists seek to provide physical and dynamical understanding of observed long term climate variations and change through analysis of hierarchies of designed GCM experiments. These include atmospheric models forced by SSTs, ocean models forced by wind stress, and coupled ocean-atmosphere GCMs, including runs forced by greenhouse gases.

*Our investigations have focused on determining fundamental processes responsible for decadal climate variability and change, and assessing whether the latter are due to human influences or natural variability. According to the Third Assessment Report of the IPCC, it is now very likely that global temperatures during the 1990s were the highest since 1861. The same appears to be true for tropical sea surface temperatures, and the areal coverage of the so-called oceanic warm pool (SSTs>28.5°C) (**Fig. 5.1, top**). CDC scientists are diagnosing relationships between this tropical ocean warming, the global atmospheric circulation and recent climate change.*

*CDC is engaged in understanding how slow changes in climate affect interannual variability. One key question is determining whether the warm pool change over the equatorial west Pacific impacts the statistics of El Niño/Southern Oscillation (ENSO) in the eastern Pacific. It is evident that the strongest El Niño events in the instrumental record have occurred in recent decades (**Fig. 5.1, middle**); we are assessing if this is a signature of climate change or merely random fluctuations. The global impacts of ENSO have also changed in recent decades. A fundamental question being pursued at CDC is whether the ENSO teleconnections diagnosed from historical data of the 19th and 20th centuries will be accurate depictions of ENSO impacts in this new, unique century of human induced climate change.*

*CDC scientists are also studying the origin and climatic impact of midlatitude ocean changes. Most dramatic among these is the multi-decadal variability in SSTs over the Pacific poleward of 30°N (**Fig. 5.1, bottom**), an index of which has been termed the Pacific-Decadal Oscillation (PDO). The apparent long time scale of this oceanic behavior is quite different from that of the ENSO time series. Nonetheless, our analysis shows a strong relation between the two on interannual time scales, and an intriguing question is the extent of their coupling on multi-decadal scales. Likewise, the low frequency variations of North Pacific SSTs since 1950 have atmospheric counterparts, including changes in the oceanic storm track and the strength of the upper tropospheric westerly jet. CDC scientists are studying the nature of air-sea interaction over the North Pacific, and assessing to what extent the diagnostic relations mentioned above entail predictability.*

5.1 Modeling studies of low frequency atmospheric variability and climate change

5.1.1 Atmospheric circulation change and the role of tropical SST warming

A significant component of global surface temperature trend since 1950 is linked with planetary scale changes in atmospheric wind and pressure patterns, and our analysis based on atmospheric GCM experiments indicates that the latter have been forced by changes in tropical SSTs. During northern winter, the trend in 500-mb heights since 1950 consists of a uniform tropical and subtropical height increase, and a wavy pattern of

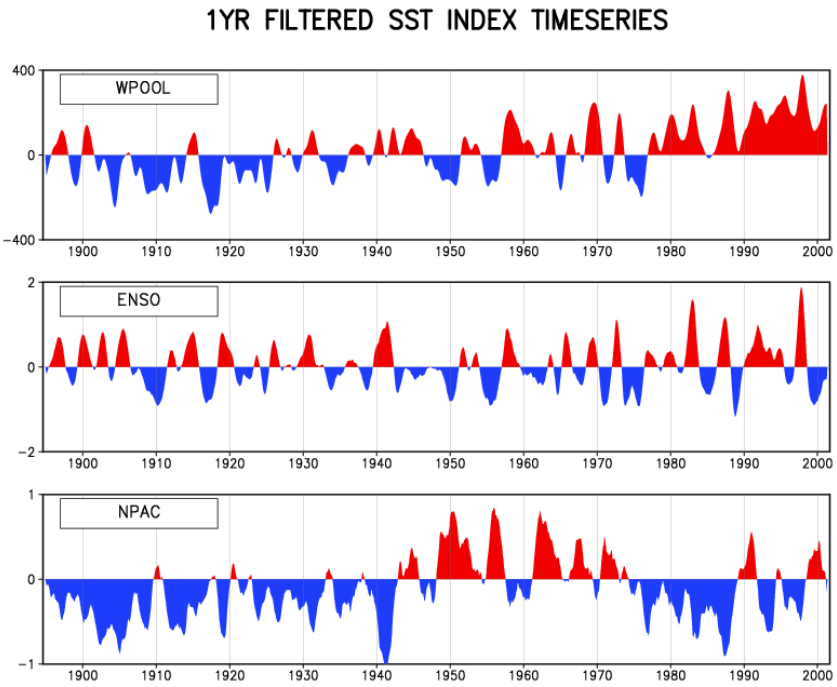

Fig. 5.1. (a) Warm pool index that describes the time series of areal coverage (expressed as the number of 2° by 2° grid boxes) of SST>28.5°C within the region (30°N–30°S, 50°E–120°W). (b) Cold tongue index of ENSO that described the time series of area-averaged SST anomalies within the region (5°N–5°S, 160°E–80°W). (c) North Pacific SST index for the area average within the region (30°N–50°N, 150°E–150°W). All time series are for January 1895–April 2001, and have been smoothed with a 13-month running mean. The warm pool index is derived from GISST 2.3b data. The ENSO and North Pacific SST indices use the Kaplan data for 1895–1949, Smith and Reynolds reconstructed SST data from 1950–1981, and the Reynolds OI data after 1982. Anomalies are computed relative to the entire 107 year period.

stationary wave change in higher latitudes highlighted by lower pressure over the North Pacific and North Atlantic (**Fig. 5.2, top**). The change in the latter region projects strongly on the North Atlantic Oscillation (NAO) structure of monthly variability. Recent hypotheses for the North Atlantic climate change include a positive feedback resulting from coupling with North Atlantic SSTs, and the possibility that the slow variations are nothing more than sampling artifacts of a random stationary process. Earlier studies of North Pacific climate change have also argued for forcing from the slow variations in extratropical (North Pacific) SSTs (see **Fig. 5.1**), together with forcing from changes in the tropical Pacific ocean. We have analyzed data from a 12-member ensemble of atmospheric simulations with NCAR's CCM3, using global SST variations since 1950, and these confirm that the observed circulation pattern trends are consistent with global air-sea interactions (**Fig. 5.2, middle**). The role of tropical SSTs is revealed from another GCM ensemble in which monthly SST variations are prescribed over only the 30°N–30°S band. That the observed trend is captured by the tropically forced simulations (**Fig. 5.2, bottom**) alone suggests that the gradual warming of those waters since 1950 is forcing NH climate change.

In fact, further analysis suggests that the secular warming within the oceanic warm pool region itself is most relevant for the simulated climate change, particularly over the distant North Atlantic sector.

Tropical SST warming since 1950 has altered tropical rainfall, the likely immediate cause for the simulated atmospheric circulation changes. The modeled rainfall trend is consistent with that of the underlying SSTs, with increased precipitation throughout the entire equatorial Indo-Pacific region (**Fig. 5.3, top**). This leads to the question of the origin of the tropical SST change itself (**Fig. 5.3, bottom**). Analysis of coupled ocean-atmosphere experiments indicate that the warming trend is beyond the range of natural variability. The changes do appear consistent with anomalous greenhouse forcing, however, insofar as the pattern and amplitude of warming during the past half century is similar to that predicted by such models when forced by observed greenhouse gas changes. Our current working hypothesis is that the spatial pattern of NH winter climate change, and the regional change over the North Atlantic/European sector especially, is being forced by a tropical ocean warming, and implicitly reflects an emergent anthropogenic signal.

5.1.2 Global warming and atmospheric angular momentum

The recent trends in wintertime NH height are strongly annular from the surface to the lower stratosphere. Heights have been increasing in the tropics but

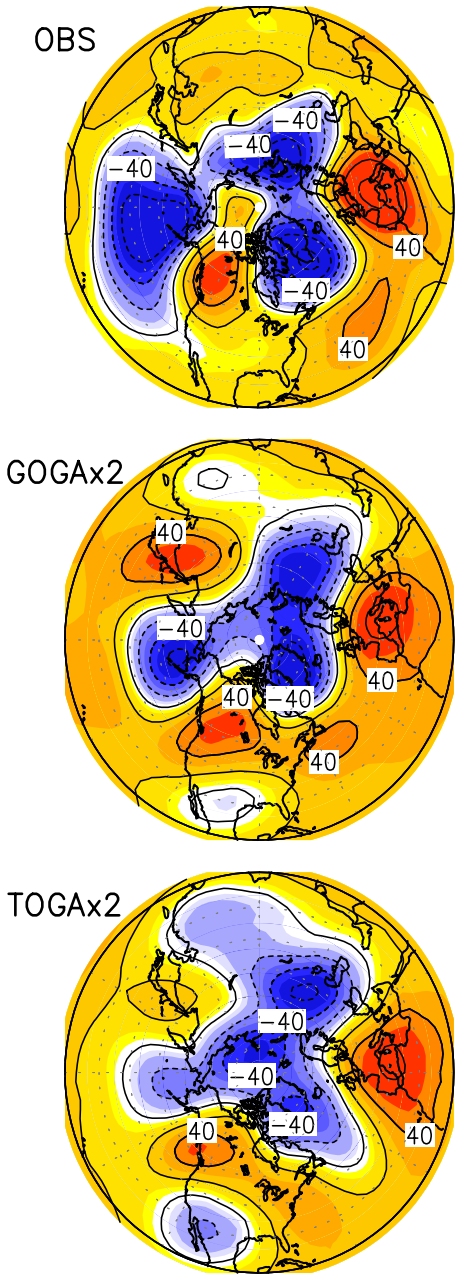

Fig. 5.2. The linear trend of the winter season (December to February) 500-mb height field based on observations (top), 12-member CCM3 ensemble forced by global SST variations (middle), and 12-member CCM3 ensemble forced by tropical SST variations over 1950-1999 (bottom). The model results have been multiplied by a factor of 2. Height increases (decreases) are indicated by solid (dashed) contours, and the contour increment is 20 m per 50 years. (Based on results of Hoerling, Hurrell and Xu, 2001, *Science*).

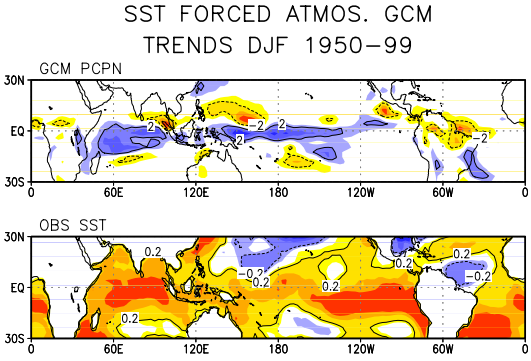

Fig. 5.3. The linear trend of the winter season (December to February) total precipitation from the 12-member CCM3 ensemble forced by tropical SST variations (top), and the observed sea surface temperatures (bottom). (Based on results of Hoerling, Hurrell and Xu, 2001, *Science*).

decreasing near the poles, and associated with this has been an increase in the atmospheric angular momentum (AAM) (**Fig. 5.4**). Much of the increase reflects a change in relative angular momentum that is due to a broad westerly wind increase within 30°N–30°S. We have been seeking an explanation for this change using GCM simulations subjected to various forcings. First, the change of AAM was investigated in a three-member ensemble of coupled ocean-atmosphere model simulations with increasing atmospheric greenhouse gases and sulfate aerosol loading for the period 1900–2100. A highly significant increase in total AAM was found to occur in those runs, with an indication that the forced change emerges above the noise of natural variability by the late 20th Century.

We hypothesize that the AAM is responding to SST changes and accompanying tropical convection, rather than to direct changes in radiative forcing. In the model, the AAM is found to accompany an increase in tropical SST with a sensitivity of ~1 AMU/°C (1 AMU = 10^{25} kg m^2 s^{-1}). A similar sensitivity is found in the observed AAM response to Niño 3.4 SSTs during El Niño. To further examine the role of SST changes only, we analyzed a 12-member ensemble of NCAR CCM3 simulations forced with the history of global SSTs during 1950–99. The simulated AAM from these runs compares well with the time history of the (single realization) observed AAM, and with the observed trend in Niño 3.4 SSTs (see **Fig. 5.4**). The AAM time

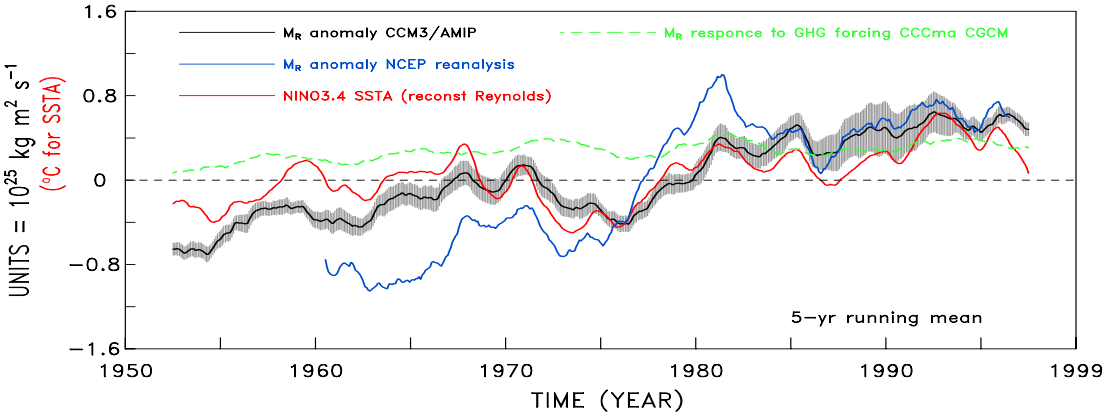

Fig. 5.4. Time series of global angular momentum from 1950–1999 based on NCEP/NCAR reanalysis (blue), 12-member CCM3 ensemble forced with global SST variations (black), Canadian Centre for Climate Modeling coupled GCM forced by greenhouse gases and aerosols (green). The standard deviation among the CCM3 ensemble members shown in shading. The time series of Niño 3.4 SSTs is shown in red. All curves smoothed with a 5-yr running mean. (Based on results of Huang, Weickmann and Hsu, 2001, *J. Climate*, in press).

series in the greenhouse forced experiment also shows an increasing trend, though it appears to underestimate the observed low frequency variability. All four curves show a trend during 1950–99 of approximately the same magnitude, although the coupled run has the smallest and the observed AAM has the largest trend. The curves cluster together after 1980, while before that time the AMIP ensemble lies between the coupled ensemble and the observed curve. The implication is that the observed AAM trend is partially the result of global warming, through its effect on the tropical heat sources, although natural variability (and NCEP reanalysis errors) probably also contribute. In any case, the anthropogenic forced change through 1999 is as yet modest, especially compared to the AAM change predicted to occur by this model over the next 100 years (~ 4 AMU).

5.1.3 Decadal variations in ENSO and its global impact

Observations reveal that the global impacts of ENSO vary substantially on decadal time scales. One example is the breakdown in the ENSO-Indian monsoon relationship in the last quarter century. In addition to such changes in tropical teleconnections, ENSO's extratropical impacts have also shown strong decadal variations. For example, ENSO has explained a much higher fraction of the seasonal atmospheric variability in the PNA-sector since 1977 compared to the prior quarter century. The February-April seasonal correlation of 500-mb heights with a SST index of ENSO has roughly

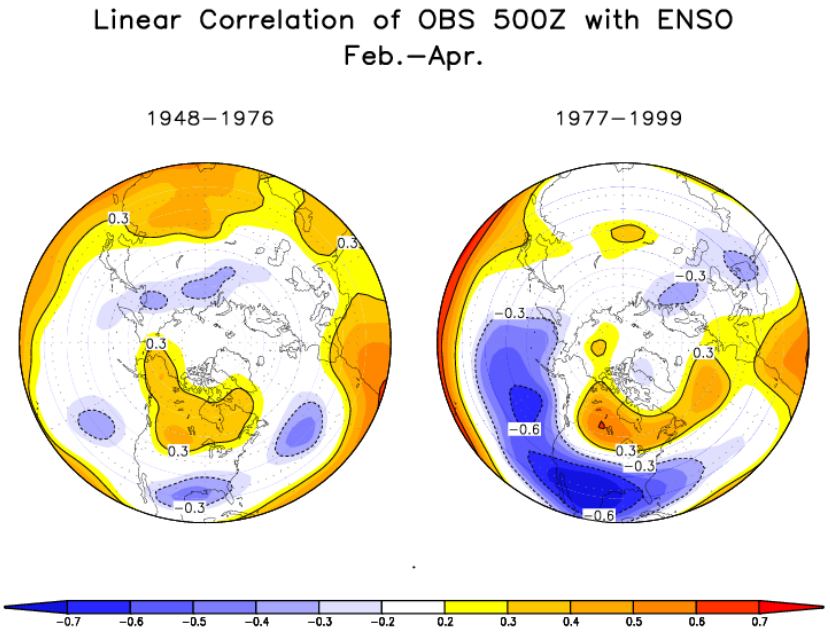

Fig. 5.5. Correlation pattern of seasonally averaged February–April 500 hPa geopotential height with the ENSO index of the middle panel of Fig. 5.1 calculated for two sub-periods: 1948–1976 (left panel), and 1977–1999 (right panel). Results are shown for the Northern Hemisphere for the area extending north of 20 degrees latitude. (Based on results of Diaz, Hoerling and Eischeid, 2001, *Int. J. Climat.*, in press).

doubled during 1977–99 compared to 1948–76 (**Fig. 5.5**). The correlation, averaged across the southern US between 120°W–70°W, increases from roughly –0.2 to –0.6 in the recent period, and points to a substantial increase in the late-winter potential predictability.

One might suppose that this change in predictability is due to the stronger ENSO forcing as measured by the increased interannual variance of tropical Pacific SSTs since 1977 (see **Fig. 5.1**). Yet, this increase is only about 20 percent, and it is not reconcilable with the much greater fractional increase in variance of the remote ENSO signal. Recent changes in the life cycle of tropical Pacific SST anomalies during warm events may be a key factor. The so-called canonical warm event evolution prior to 1977, using the cases of Rasmusson and Carpenter, had peak warming in December, followed by rapid decay (**Fig. 5.6, left panel contours**). We have calculated the difference in SST lifecycles between the post-1977 and pre-1977 warm events (**Fig. 5.6, left panel shading**), and found that recent cases prolong their warming into spring of year+1, and also defer South American coastal warming until spring of year (+1). This change is relevant for the teleconnections because the recent warm events peak closer to the peak in climatological warming of the east equatorial Pacific ocean, so that the total SST is actually now maximized in spring of year+1 rather than in early win-

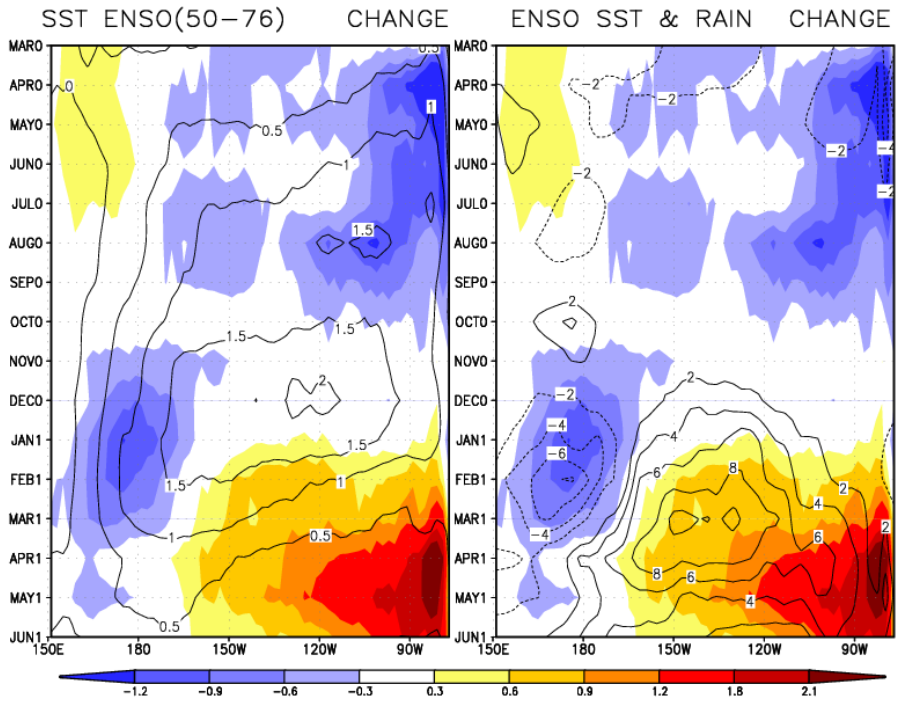

Fig. 5.6. Hovmuller diagrams illustrating the change in the composite life cycle of SST and rainfall anomalies along the equatorial Pacific during 1948–1999. In the left panel, contours illustrate the composite El Niño SST anomaly based on pre-1976 events, whereas the shading illustrates the difference in El Niño SST composites for events occurring after versus before 1976. In the right side panel, the contours illustrate the change in El Niño rainfall anomaly composites for events occurring after versus before 1976, as derived from climate simulations. The shading repeats the SST change of the left panel. (Based on results of Diaz, Hoerling and Eischeid, 2001, *Int. J. Climat*., in press).

ter. Using output from AMIP-style simulations spanning 1950–99, we have found a large increase in rainfall for the post-1977 events relative to the pre-1977 events (**Fig. 5.6, right panel contours**) that corresponds closely with the change in SSTs. The change in composite rainfall represents a doubling relative to the pre-1977 cases, suggesting that the recent teleconnection strength is at least qualitatively consistent with a secular change in tropical forcing, though other factors may also be involved.

5.2 Modeling studies of fundamental ocean processes

From the various atmospheric GCM experiments described above, two aspects of tropical ocean change in the 20th Century have been implicated as forcing observed atmospheric change; *i)* the warming of the warm pool region and *ii)* the nonstationarity of the ENSO time series. Our research on fundamental ocean processes leads to the hypothesis that these two oceanic changes are themselves coupled, and in particular that the recent increase in El Niño amplitude is consistent with the increase in warm pool temperature.

5.2.1 Decadal ENSO variability and the role of warm pool SST

From detailed analysis of the 1986–87 El Niño event, we find that El Niño represents a mechanism by which the equatorial Pacific transports heat poleward, a result subsequently confirmed from a more extended study using NCEP data for the last 20 years. In particular, a systematic relationship between the ocean heat content in the western Pacific and the magnitude of El Niño warming was diagnosed for six events since 1980—the higher the heat content in the western Pacific, the stronger the subsequent El Niño warming (**Fig. 5.7, top**). The occurrence of warm pool heat content maxima,

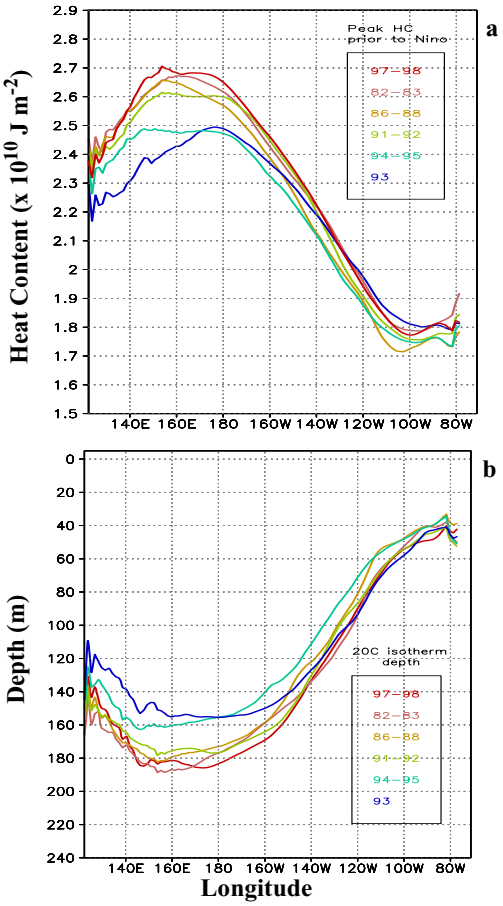

Fig. 5.7. (a) Zonal distribution of upper ocean heat content (0–260 m) in the equatorial belt (5°S–5°N) when the western Pacific heat content reaches its pre-El Niño peak. Upper ocean heat content used for this figure was smoothed in time using a Hanning window with a width of 13 months. (b) The corresponding depth of the 20°C isotherm. The ocean temperature used for calculating the 20°C isotherm depth was smoothed in time using a Hanning window with a width of 13 months. (Based on results from Sun 2001, *J. Climate*, submitted).

at which time the zonal cross sections of **Fig. 5.7** were made, precede the maxima in Niño 3 SST anomalies by 12–24 months.

Our interpretation is that higher heat content in the western Pacific is achieved through a deepening of the local thermocline, thus linking the heat content in the western Pacific to the potential energy of the ocean and thereby with the stability of the coupled ocean-atmosphere system (**Fig. 5.7, bottom**). As warm-pool SST initially increases, the zonal SST contrast also increases, strengthening the trade winds. The stronger Walker circulation then interacts with clouds and water vapor, allowing more solar radiation to reach the ocean's surface over the east Pacific equatorial cold-tongue, and at the same time, reducing the surface evaporative cooling over that region. This is so because the impact of change in the gradient term of the latent heat flux formula exceeds the impact of increased wind speed. Through non-local ocean wave dynamics and transports, heat content increases in the equatorial upper ocean of the western Pacific warm pool. The resulting steeper tilt of the equatorial thermocline is hypothesized to destabilize the coupled system which is followed by energy release through a stronger El Niño.

To test this hypothesis, we constructed a coupled model. The atmospheric model is statistical, with the equatorial surface winds proportional to the zonal SST gradients. The ocean component is a primitive equation model and therefore explicitly calculates the heat budget of the entire equatorial upper ocean. The model produces ENSO-like variations. The evolution of the subsurface ocean temperature over the life cycle of the model El Niño resembles that of observations (**Fig. 5.8**). In response to an increase in warm pool SST, the model has a stronger El Niño. Similar to the observational results, this simple model shows that an increase in warm pool SST strengthens the zonal SST contrast during ENSO's cold phase, which leads to an effective increase in the upper ocean heat content in the warm pool. Stronger El Niño warming then follows, which acts as a poleward heat pump. Of course, other processes can operate to increase warm pool SSTs. In regard to the observed recent climate change (see **Fig. 5.1**), it is reasonable that the warm pool has increased due to local radiative forcing related to the increase in anthropogenic gases. It is hypothesized that this externally forced change may be influencing the statistics of ENSO through the mechanisms described above.

5.2.2 North Pacific decadal ocean variability and the role of the tropics

As mentioned earlier, the time series of the ENSO index is correlated with that of North Pacific SSTs (see **Fig. 5.1**), despite their different time scales of variation. This reflects in part the well-known fact that ENSO influences the North Pacific circulation, which in turn forces North Pacific SSTs, on interannual time scales. The question we have pursued is to what extent this atmospheric bridge between the tropics and extratropics contributes to the decadal variability over the North Pacific, including the Pacific Decadal Oscillation? We have addressed this

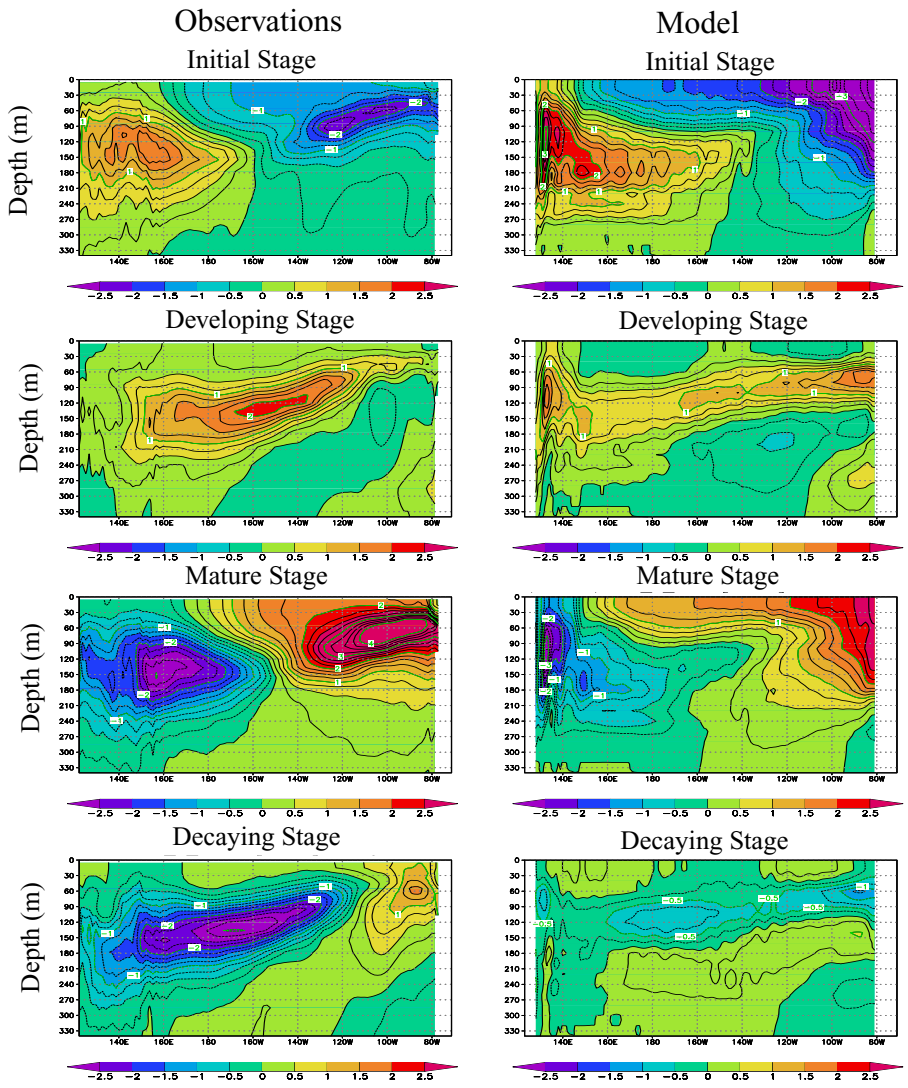

Fig. 5.8. The observed (left panels) and coupled model simulated (right panels) ocean temperature anomalies during an El Niño event's life cycle. Vertical sections are from surface to 330 m. Warm (cold) anomalies in red (blue). Observations based on El Niño composite during 1980–1999 based on NCEP ocean analysis. (Based on results from Sun 2001, *J. Climate*, submitted)

question by comparing the observed and simulated leading pattern (EOF 1) and associated principal component time series (PC) of wintertime North Pacific decadal SST variability (**Fig. 5.9**). The model results are obtained from the ensemble average of 16 50-year GFDL R30 AGCM simulations in which observed SSTs are specified in the tropical Pacific over the period 1950–1999 and a mixed layer model (MLM) is coupled to the AGCM elsewhere over the global oceans. The EOFs are based on the monthly SST anomalies that were first low-pass filtered to retain periods greater than ~10 years and then the fil-

tered values from November to March were averaged together. The observed and MLM EOFs resemble each other in several respects: they both explain about half of the variance, and they are relatively well correlated in space and time, with a spatial (temporal) correlation of 0.71 (0.69). The patterns in **Fig. 5.9** are very similar to those based on unfiltered data which has conventionally been used to define the PDO. The observed and simulated PCs are well correlated with the filtered ENSO index time series, with correlation values of 0.77 and 0.90, respectively. In addition, maps of SST differences centered on 1976 (e.g., 1977-1988 minus 1970–1976, and 1977-1998 minus 1951-1976; not shown) indicate that the "abrupt climate transition" in the model and observations are similar and resemble the leading EOF but the amplitude of the differences is approximately half as large in the MLM. Overall, our model results suggest that a significant fraction of the variance of the dominant pattern of low frequency SST variability in the North Pacific is associated with the atmospheric bridge.

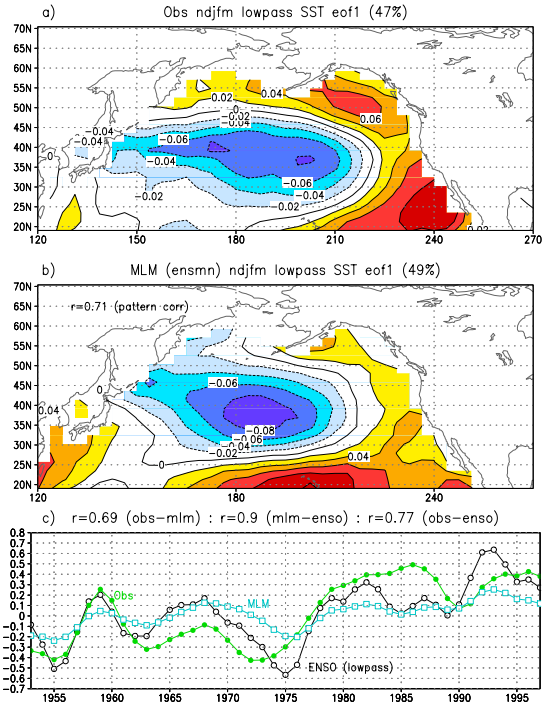

Fig. 5.9. EOF 1 of the low-pass filtered (> ~10 years) SST anomalies during November–March from (a) observations and (b) the MLM. (c) The first principal component (time series associated with EOF 1) of the low-pass SST anomalies from observations (green line), the MLM (blue line) and low-pass ENSO index (black line). The correlations (r) between the three time series are given above (c). (Based on the results of Alexander, Blade, Newman, Lau, and Lanzante, 2001, *J. Climate*, submitted).

5.2.3 Subduction and Rossby wave dynamics: mechanisms for decadal ocean variability

Dynamic ocean processes likely play a fundamental role in climate variability on decadal timescales. Rossby wave propagation can introduce multi-year delays in the oceanic response to changes in the atmospheric forcing. Subduction, where surface waters enter and flow within the permanent pycnocline, provide a link between the extratropical and tropical oceans over an ~8 year period. It has been conjectured that when the subducted anomalies reach the equator, they alter the equatorial SSTs and affect the North Pacific Ocean via the atmospheric bridge, completing a circuit that enables decadal oscillations. CDC has been involved in observational and modeling studies that examine subduction and Rossby waves in the Pacific Ocean.

The standard deviation of the depth of the 25.5 s_θ isopycnal surface, obtained from a global OGCM forced by observed surface fluxes, indicates that there are three major centers of variability, includ-

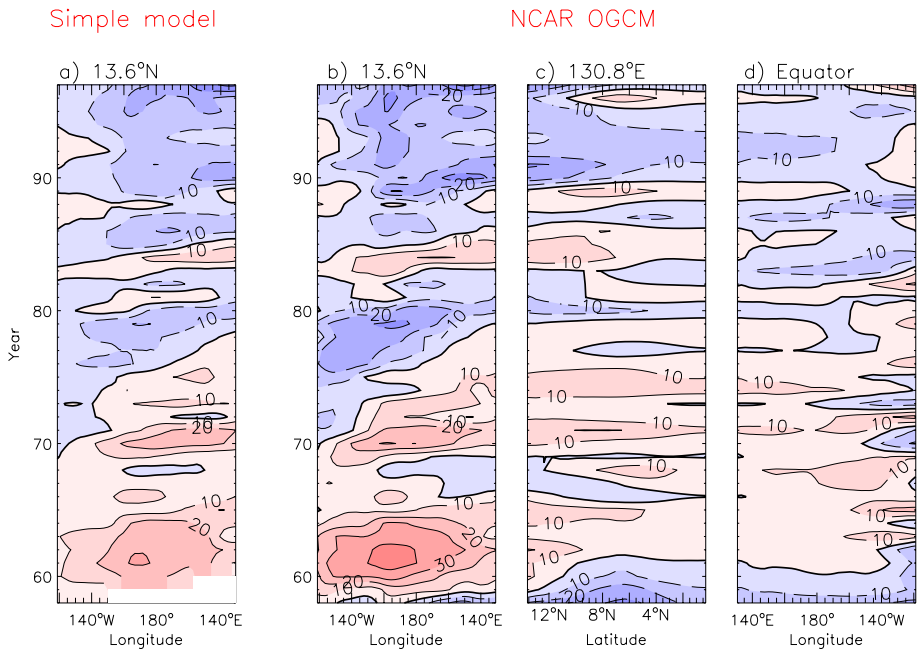

Fig. 5.10. (a) Evolution of the thermocline depth along 13.6°N (from east to west) as computed using a first-mode baroclinic Rossby wave equation forced with the Ekman pumping derived from the NCEP-NCAR reanalyses over the period 1958–1997. The equation was solved using the method of characteristics. Contour interval is 10 m. Negative values (shallower thermocline) are shaded in blue, while positive values (deeper thermocline) are shaded in red. (b) Same as in (a), but computed from the NCAR OGCM. The 25.5 isopycnal has been used as a proxy for thermocline depth. (c) Evolution of the depth of the 25.5 isopycnal along 130.8°W from 13.6°N to the equator. (d) Evolution of the depth of the 25.5 isopycnal along the equator, from east to west. In the OGCM anomalies originating along 13.6°N can be tracked all the way to the equator and along the equator. (Based on results of Capotondi and Alexander, 2001, *J. Phys. Oceanogr.*, in press).

ing: *i)* the Kuroshio region (30°N, 160°E), *ii)* along the outcrop line at 35°N between 180°–140°W, and *iii)* the tropics between 10°N–15°N. The variability in the Kuroshio region reflects changes in the ocean thermal structure resulting from the basin-wide changes in the strength of the westerly winds that occurred in the late 1970s and late 1980s. The thermocline changes lag changes in the basin-wide wind stress curl forcing by 4–5 years, consistent with the timescale of oceanic adjustment through Rossby wave propagation. The second center of variability is associated with subduction, where it has been proposed that thermal anomalies produced at the surface primarily by anomalous heat fluxes, propagate equatorward along isopycnals by the mean currents. Analyses of the OGCM and observations has allowed us to track thermal anomalies from their source region 25°N–35°N, 140°W–170°W southwestward to ~18°N over a period of ~8 years. South of this latitude thermocline variability appears to be driven by local wind forcing.

The isopycnal depth changes in the subtropics of both hemispheres are associated with large thermocline temperature variations in both the OGCM and obser-

vations. We have examined the variability at 10°N–15°N by comparing the OGCM results with those obtained from a simple Rossby wave model forced by the same winds used in the OGCM simulation. The evolution of thermocline depth is remarkably similar in the simple model and OGCM (**Fig. 5.10**), indicating that a substantial portion of the variability in the 10°–15°N latitude band results from wind-forced baroclinic Rossby waves. Spectra and Hövmoller diagrams based on low-pass filtered OGCM output indicate that most of the thermocline variability occurs at periods longer than ~7 years. East of the dateline, subtropical Ekman pumping anomalies exhibit variability over decadal periods and propagate westward at speeds close to the phase speed of first baroclinic mode Rossby waves. Thus, the spectral characteristics of the forcing may be responsible for the enhanced oceanic response at low frequencies. The thermocline signal that propagates across the basin at 13°N, moves southward along the western boundary and then eastward along the equator (see **Fig. 5.10**). The low-frequency variations of the thermocline depth along the equator may modulate the amplitude and period of ENSO events on decadal timescales, an outcome we plan to explore in the near future.

5.3. Empirical studies of decadal variability and climate change

5.3.1 Observed change in the global hydrologic system

Interest in the potential impacts of climatic change in high elevation regions has grown in the past decade, as information from glacial monitoring sites and from fieldwork has demonstrated that significant melting and glacial recession has been occurring. Fifty-year trends in near-surface temperature (1948–2000) averaged over 5 different mountainous

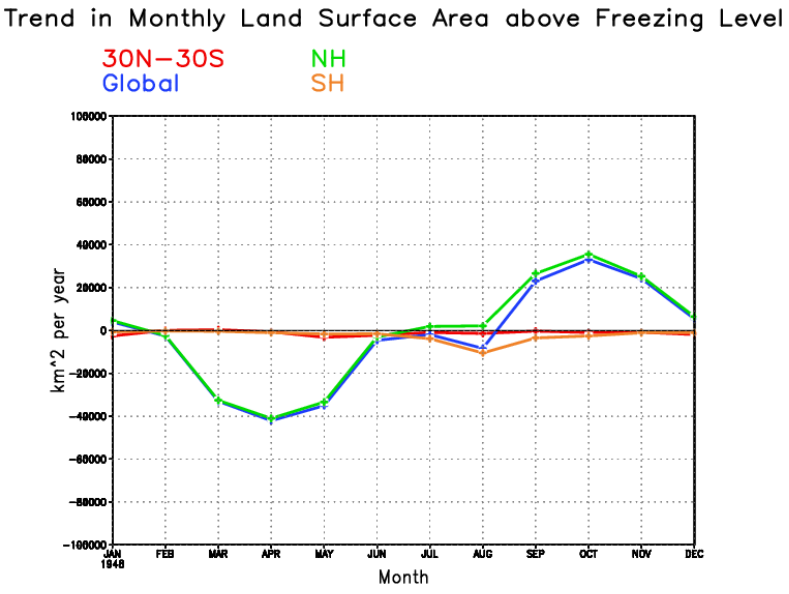

Fig. 5.11. The 1948–2000 linear trend in surface area above the freezing level surface (FLS) for the tropics, NH, SH, and globe for each calendar month. Data is the NCEP/NCAR reanalysis. (Based on a study by Diaz, Eischeid, Duncan and Bradley 2001).

regions are similar in magnitude to global temperature trends (+0.4–0.6 °C/50 yrs). We have been studying the relation between such behavior and changes in the land surface area located above the freezing level. The freezing level surface (FLS) is defined to be the 0°C isotherm, and the land area inside the roughly 2.5° lat/lon grid boxes of the NCEP/NCAR Reanalysis data that exceeds the FLS height was calculated monthly during 1948–2000. The most striking result is the strong seasonal dependency of trend in the land surface area above the freezing level, with largest decreases in spring consistent with a warming, but nearly equal increases in fall indicative of cooling (**Fig. 5.11**). Overall, the annual change reveals a small net decrease.

We are studying the impacts of climate change on a number of natural systems, including alpine hydrology and ecology, and the relevance for water resources management. A prominent feature of low frequency variability in streamflow has been the systematic change in timing of peak runoff over most of the globe since 1945 (**Fig. 5.12**). Peak flows are occurring earlier now than a half-century ago. This is particularly pronounced in river basins with a high fraction of their streamflow supplied by snowmelt, and reflects the springtime warming trend in these regions.

5.3.2 Secular change in North Pacific cyclone activity

The picture emerging from our GCM analyses of wintertime atmospheric trends since 1950 is of a relationship between changes in tropical SSTs and trend patterns in zonally averaged flow and planetary waves, in the sense that the former is forcing the latter. Given that the large scale circulation controls the statistics of sub-seasonal variations, such phenomena as the storm tracks and the transients that define them should also exhibit secular change. As one example, we have documented an increase in the frequency and strength of intense winter cyclones (minimum central pressure lower than 975 hPa) in the North Pacific Ocean since 1948 (**Fig. 5.13**). The time

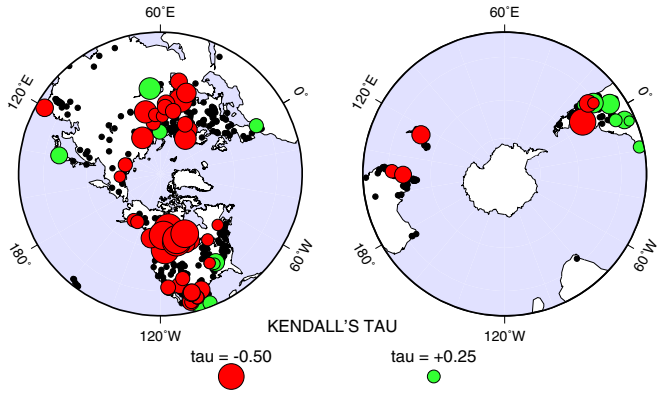

Fig. 5.12. Global trends in the time of streamflow during 1945–1993 as measured by the flow-weighted average day of flows in extratropical rivers. Red circles denote retrogression of the annual hydrograph. (Based on a study by Dettinger and Diaz, 2001).

series of December-March averaged counts of cyclones having a minimum pressure below 975 mb shows a substantial increase since 1948.

Associated with these changes are upward trends in extreme surface wind speeds between 25°–40°N, and an increase in significant wave heights. It is surmised that the cooling trend of North Pacific SSTs since 1950 (see **Fig. 5.1**) has in part been driven by the anomalous latent heat fluxes associated with this enhanced storminess. We also postulate that increasing sea surface temperatures in the western Pacific warm pool region (see **Fig. 5.1**) is a cause of the observed cyclone changes. The NCAR CCM3 simulations give some support for this premise, insofar as changes in the western Pacific warm pool and ENSO amplitude on decadal-scales impact the midlatitude stationary waves via teleconnection processes.

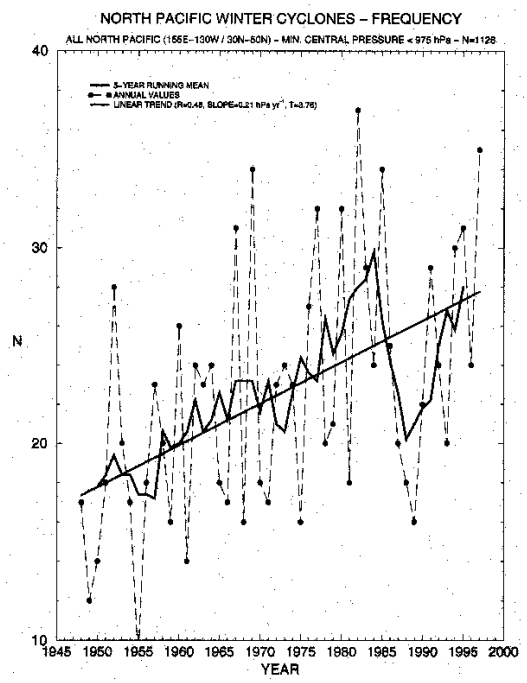

Fig. 5.13. Time series of the frequency of North Pacific winter cyclones having minimum sea level pressure < 975 mb during 1948–1997. The dark curve is the smoothed 5-yr point average, and the dark line is the linear trend. Data is the NCEP/NCAR reanalysis. (Based on results from Graham and Diaz, 2001, *Bull. Amer. Meteor. Soc.*, in press).

5.3.3 Decadal variations in summertime monsoons

Large summertime changes have occurred in tropical monsoon circulations since 1948 that are no less dramatic than the aforementioned low frequency variations in the wintertime ocean/atmosphere system. We already alluded to the secular change in ENSO's interannual impacts on Indian summertime monsoon rainfall. We have examined the mean change in the summertime monsoons since 1948 using the NCAR/NCEP reanalysis circulation data, together with station rainfall data where available. A prominent change has occurred in the divergent mass circulation describing the summer monsoons of both western and eastern hemispheres (**Fig. 5.14, top**). The maxima in the change map represent roughly 20 percent of the climatological mean. Station rainfall data allow us to verify that drying has indeed occurred over the Sahel in recent decades, consistent with the trend toward strong low level divergence (red shading) and implied sinking motion in the re-analysis data. We have yet to establish the realism of the re-analysis changes in the other summertime monsoons of Asia and the Americas, and a key hurdle in making sense of this picture is determining the fidelity in the re-analysis data itself, which is known to be biased by some spurious trends during 1948–2000.

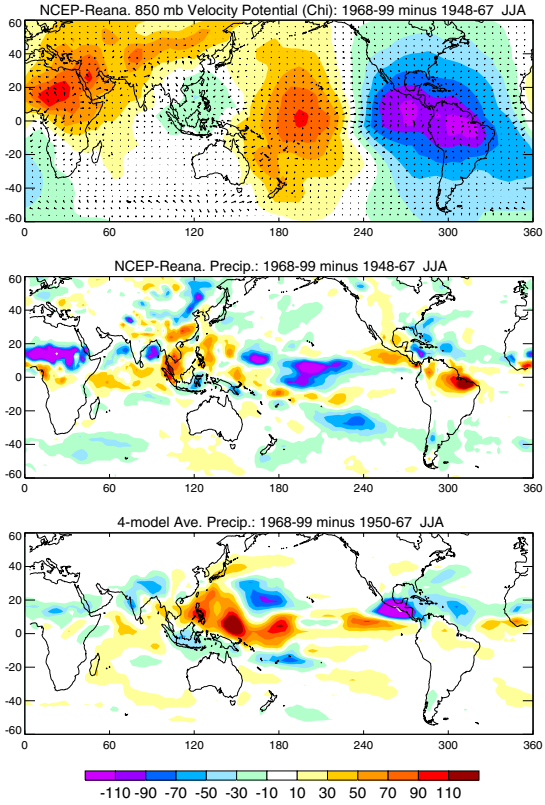

Fig. 5.14. Interdecadal change in the (top) 850mb velocity-potential (5 x 10^6 m^2 s^{-1}), (middle) precipitation (mm $month^{-1}$) of the NCEP/NCAR reanalysis, and (bottom) precipitation of the average of four atmospheric general circulation models (0.3 mm $month^{-1}$). (Based on results of Quan, Diaz, and Fu, 2001, *J. Climate,* submitted).

To be sure, the re-analysis mass circulation changes are consistent with the re-analysis rainfall changes (compare top and middle panels of **Fig. 5.14**), and it is the origin of the latter which requires an explanation. We have begun to pursue the possibility that such apparent tropical-wide, low frequency changes in the atmosphere are reacting to a lower boundary SST change, perhaps akin to the wintertime change in tropical forcing discussed in earlier sections. The lower panel of **Fig. 5.14** shows the change in rainfall as derived from a multi-GCM ensemble of AMIP-style simulations of 1950–1999. Rainfall has increased in the simulations over oceanic regions (red shading), especially the warm pool of the western Pacific and the Indian Ocean. This is in broad agreement with the re-analysis. Note also that the general drying (blue shading) over North Africa, Indonesia, and the Caribbean in re-analysis data emerges as a response pattern to SST. Our assessment is not complete, and we are pursuing various hypotheses motivated from our empirical study.

EPILOGUE

It has become increasingly important to provide attribution for low frequency variations and change in Earth's climate. Whether this is for improved scientific understanding, predictability assessment, or to better inform societal planning and decision making, CDC is dedicating increasing resources to climate change research. At CDC, we seek to offer *dynamical explanations* for observed low frequency variations and change, thereby drawing strongly upon our expertise on seasonal to interannual variability, especially regarding air-sea interactions and teleconnective influences.

A key challenge that we will pursue in CDC is to understand and anticipate the *regional characteristics of climate change*. While there is now little question that the climate has changed in a globally and annually averaged sense, it is unclear what the local manifestations of this are, nor do we appreciate their seasonal dependencies. Beyond its relevancy to

long term planning, this problem is of high relevance to seasonal climate predictions. The fact is that the leading source of US winter temperature skill in the 1990's is due to the so-called optimal climate normals (OCN) tool, which we understand to be essentially a trend prediction. It is necessary that a physical explanation for such trends be given, and that they be clearly distinguished from low frequency climatic variations. Most apparent of these trends is the US wintertime surface warming, but other seasons show a more complicated pattern for temperature and rainfall change. We believe that progress can be made by improving our understanding of the regional responses to the slow, systematic changes in tropical oceans such as illustrated in **Fig. 5.1**, and we expect that much is to be gained from our existing knowledge of the interannual impacts of tropical forcing.

The change in the oceans itself is a problem that will focus future CDC decadal climate research. The mean change in ocean temperatures is a question that will require increased analysis of coupled ocean-atmosphere models. We expect to partner with GFDL, NCAR and other interested scientists to diagnose and understand the variability in coupled model simulations, both natural and forced. We are especially interested in the sensitivity of ENSO to climate change, both its statistical properties and its interannual global impacts. A related challenge is to understand whether the year-to-year predictability of climate will change appreciably under the influence of human-induced mean change. Will ENSO as an oceanic phenomena become more predictable? Is it possible also that new regions will begin to have useful ENSO-related climate predictability? Likewise, we would like to understand whether the seasonal cycle of predictability will change due to an altered mean climate. These questions, among others, cut across time scales, and the greatest payoff in solving them may in fact be to advance key problems on shorter time scales, such as interannual prediction.

Contributed by: *M. Alexander, A. Capotondi, H. Diaz, M. Hoerling, H. Huang, X. Quan, D. Sun, and K. Weickmann.*

CHAPTER 6

Experimental Climate Services

In addition to its basic climate research, CDC provides an extensive range of experimental climate services. Climate services require sustained and systematic communication of climate information to a broad spectrum of users, and interactions with users to determine their priorities and needs. A common objective of our experimental climate services is to address NOAA's goal of improving mechanisms for dissemination of climate and weather products. Enhancing access to climate information also facilitates basic climate research and expands the scientific basis for informed public planning and policy decisions.

Research at CDC and elsewhere indicates that there are currently substantial barriers to the effective use of climate information (e.g., requirements for better and more timely access to data, improved visualization, user-specific needs, and organizational obstacles to factoring climate information into decisions). CDC employs various approaches to overcome such barriers, in order to develop improved NOAA climate products that address both research scientist and non-traditional user needs. Experimental climate services activities in CDC fall into five categories: 1) enhanced weather and climate monitoring products and experimental climate forecasts; 2) WWW based value-added access, analysis, and visualization tools for climate data; 3) user studies and societal interactions; 4) Western Water Assessment activities; and 5) public health and climate research.

6.1 Experimental monitoring products and climate forecasts

CDC research has lead to the development of a number of experimental climate monitoring and forecasts products, which are systematically updated and evaluated along with operational products. Collectively these efforts provide the scientific research community and non-traditional users access to enhanced climate information, current climate conditions, and climate forecasts.

6.1.1 Value Added Diagnostics and Visualization Products for Weather and Climate Monitoring

The CDC WWW-based maproom (http://www.cdc.noaa.gov/map/) provides a focal point for monitoring and prediction products on climate variability, climate impacts and climate-weather connections. The CDC maproom encompasses a broad range of diagnostic products and enhanced visualization tools for weather and climate monitoring. A vast majority of these diagnostic and value-added visualization products were designed initially to support in-house research. These are now active research areas themselves, with goals being to develop enhanced climate and weather monitoring products and to evaluate operational and experimental climate and weather forecasts. The core of the maproom consists of analyzed and predicted fields of climate variables that are updated on a daily basis, and that provide the raw data for both conventional and experimental products. The maproom is also a host site to enable a similar scope of studies by non-CDC scientists.

The maproom supports CDC's research, diagnostic and assessment activities by serving as: a) a testbed for new products related to climate monitoring and prediction; b) a means to interact with users of climate and weather information; c) a way to familiarize climate researchers with ongoing climate anomalies; and d) a tool to interpret the current state of the climate with emphasis on coherent modes of variability such as ENSO, MJO, NAO, etc. Weekly maproom briefings provide a forum to discuss the maproom products and to monitor the performance of new products.

Several maproom improvements have been undertaken since 1997. Some of these have involved streamlining scripts, consolidating products, and ensuring timely access to data streams. Specific improvements and additions related to maproom content include:

1) Applying Java animation scripts to climate variables for time averages from daily to seasonal,

2) Use of the NCEP reanalyses as the basis for global atmospheric products rather than the NCEP operational data,

3) Monitoring coherent modes of tropical OLR variability, including the MJO,

4) Monitoring storm tracks based on a sea level pressure algorithm (storm track data from 1958–present also available),

5) Prediction of seasonal anomalies based on the historical response to SSTs in an ensemble of AMIP runs,

6) Monitoring atmospheric angular momentum budget for intraseasonal and longer term variations,

7) Monitoring the states and ensemble predictions of Northern Hemisphere teleconnection patterns,

8) Implementing 500 mb height anomalies and regional plots over North America from the NCEP ensemble predictions,

9) Implementing probabilistic Week 2 predictions from the NCEP MRF/AVN ensemble.

CDC's interest in attribution of climate anomalies, and comments from users of climate information (including EMC and CPC), helped drive the development of many of these products. Development of new methods in climate prediction within CDC, on both weekly and seasonal time scales, has resulted in an increase in experimental prediction products for the maproom.

Web usage statistics for the maproom show that the NCEP MRF ensemble predictions to 15 days are among the most popular products. CDC displays both conventional variables (e.g., 500 mb geopotential height) and experimental products (e.g., forecast probability of a 1 or 2 standard deviation anomalies in 850 mb temperature) in the maproom. There is substantial interest in these products from national energy companies which monitor long-range weekly forecasts. In the future, CDC will continue to develop new products that will help identify the variability and trends in the earth's climate. User interactions will help CDC

identify existing products and how they may be improved.

6.1.2 Multivariate ENSO Index (MEI)

In addition to providing easy access to interannual indices and maps of climate variability, CDC provides a near-real time monthly updated Multivariate ENSO Index (MEI) based on six COADS atmosphere-ocean variables over the entire tropical Pacific basin: sea-level pressure (P), zonal (U) and meridional (V) components of the surface wind, sea surface temperature (S), surface air temperature (A), and total cloudiness fraction of the sky (C). One week after the end of each month, the MEI is extended based on near-real time NCEP marine ship and buoy observations summarized into COADS-compatible 2-degree monthly statistics. During the summer of 1997, the MEI was put on the WWW and quickly gained popularity as a monitoring product with monthly updates on the 1997–1998 El Niño (**Fig. 6.1**). In the past five years, the time series of the MEI has been distributed to hundreds of scientists and many other interested parties, and included in many publications, both scientific and popular.

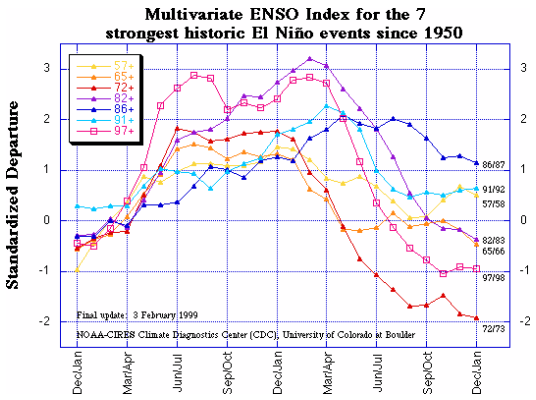

Fig. 6.1. The seasonally normalized MEI documents the evolution of individual El Niño (shown here) and La Niña events, allowing for direct intercomparison of the relative strength of ENSO events since 1950 (http://www.cdc.noaa.gov/~kew/MEI/).

6.1.3 Linear Inverse Modeling Forecasts of Tropical Sea Surface Temperatures

The development of a linear inverse modeling (LIM) approach to generate low-frequency climate forecasts is a prime example of CDC basic climate research directly contributing to the NOAA goal of providing new and improved climate forecasts. As a service to the scientific community, since the mid 1990's CDC has produced LIM tropical SST forecasts and made the forecasts available on the WWW and in the *EFFLB* along with appropriate verification statistics. CDC provides monthly predictions of tropical Indo-Pacific sea surface temperature anomalies (SSTAs) with 3, 6, 9, and 12 month lead times using a linear inverse modeling procedure with tropical Indo-Pacific SSTAs as predictors (**Fig. 6.2**). Anomalies are calculated relative to the standard 1950–1979 COADS climatology. CDC also produces similar LIM monthly predictions of northern tropical Atlantic Ocean and Caribbean sea surface temperature anomalies (SSTAs) with 3, 6, 9, and 12 month lead times. In contrast with tropical Indo-Pacific forecasts, these predictions are generated using global tropical SSTAs as predictors and anomalies are calculated relative to the COADS 1950–1993 climatology.

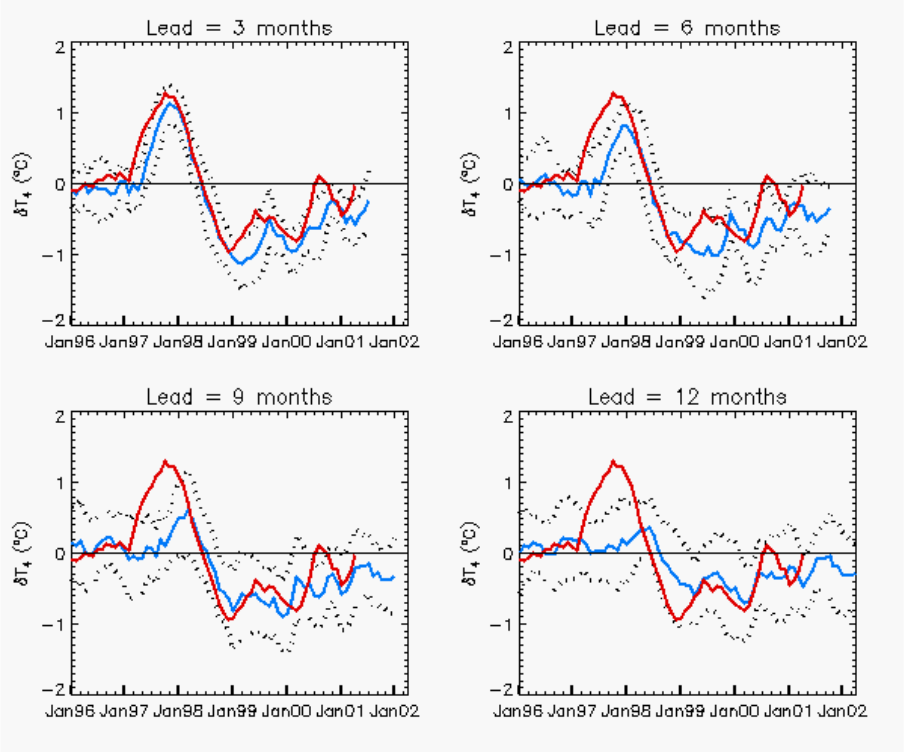

Fig. 6.2. Predictions of Niño 4 SSTA (solid blue line) and verification (solid red line). Dashed lines indicate one standard deviation confidence intervals appropriate for the LIM forecast (as opposed to those based on the history of standard deviation of previous forecast errors).

6.1.4. Subseasonal LIM forecasts of Tropical heating and extratropical circulations

For over a year, CDC scientists have used LIM to make medium and extended range (Weeks 2 to 6) forecasts of weekly average anomalous 250 and 750 mb streamfunction and tropical diabatic heating (**Fig. 6.3**). The procedure (described in Chapter 2) is similar to the method used to predict tropical Indo-Pacific and Atlantic/Caribbean sea surface temperature anomalies, except that streamfunction and diabatic heating are the model variables and the time-scale is weeks instead of months. NCEP MRF model forecasts at Week 2 and current verifications are provided for comparison when available (**Fig. 6.3**). The CDC wintertime and summertime forecasts are currently made out as far as six weeks ahead. A second forecast, the Combined forecast, is made by combining the LIM technique with the NCEP MRF ensemble mean Week 1 streamfunction forecast. Throughout the winter (Dec. 1–Feb. 28) and summer (Jun. 1–Aug. 31) these forecasts are updated daily. Much of the skill in these LIM forecasts, particularly at the extended range, is not only due to anomalous tropical convection related to ENSO but also to the extratropical response to the MJO. Advances in this experimental climate services forecast product will depend both on continued model development and evaluation and

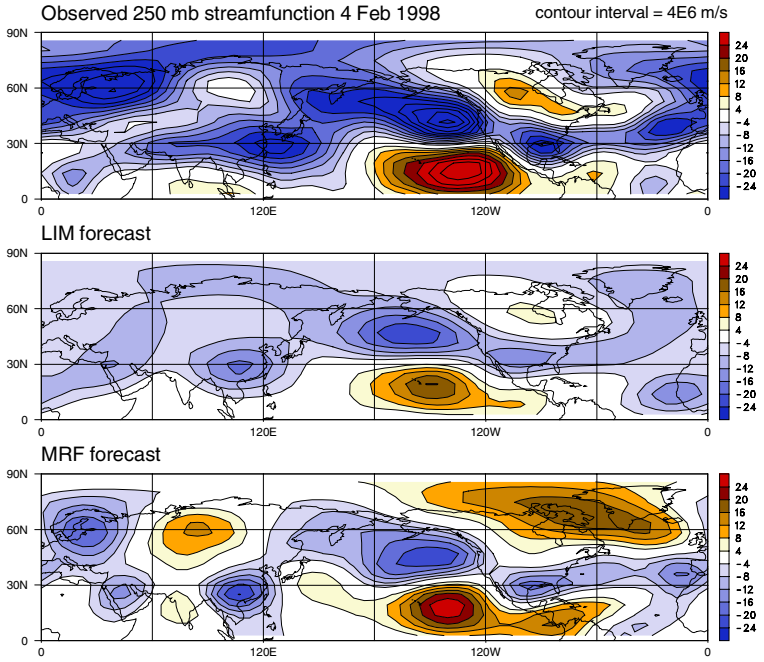

Fig. 6.3. Top: Observed 7-day running mean 250 mb streamfunction pattern for February 4, 1998. Middle: Week 2 linear inverse model forecast of 7-day running mean 250 mb streamfunction verifying against top panel. Bottom: Week 2 MRF forecast verifying against top panel.

on enhanced monitoring and prediction of MJO activity.

6.1.5 Other experimental forecast products

CDC provides monthly experimental CCA forecasts of tropical SSTs, precipitation, 500mb height, and surface temperature for the subsequent 4 overlapping 3-month season (**Fig. 6.4**, http://www.cdc.noaa.gov/~gtb/seasonal/). Predictions of tropical SSTs are derived from 4 different sources: (1) an inhouse CDC canonical correlation analysis (CCA) model, (2) the NCEP's Climate Modeling Branch (CMB) SST forecast, (3) the International Research Institute's (IRI) forecast of tropical SSTs, and (4) the CDC LIM Indo-Pacific SST forecast. Each tropical SST forecast, plus their linear average, are used as boundary conditions for predicting seasonal climate anomalies. A second CCA model relates the first 28 EOFs of tropical SSTs to a similar 28 EOF basis of an atmospheric predictand. The predictands are seasonal tropical precipitation anomalies, Pacific-North American seasonal temperature and precipitation anomalies, and Pacific-North American seasonal 500-mb height. The predictand data are derived from ensemble simulations from four atmospheric GCMs (NCEP MRF9, ECHAM3, CCM3, GFDL-R30) run for 1950–99 and forced with the monthly varying global SSTs. The atmospheric prediction is made by first projecting the predicted tropical SST anomalies onto the 28 EOF SST basis set for 1950–1999. The CCA model, based on zero-lag relations of this SST and the individual

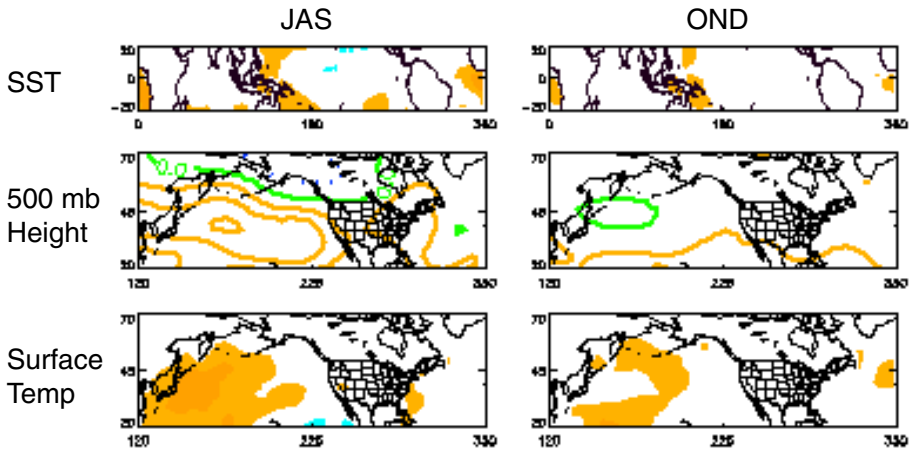

Fig. 6.4. CDC experimental June 2001 forecasts for July-August-September 2001 and October-November-December 2001.

atmospheric predictands derived from the GCMs, is then used to predict seasonal precipitation anomalies and atmospheric circulation.

6.1.6 Week 2 predictions and the atmospheric angular momentum budget

CDC is working with the Dodge City (KS) NWS Office to link weather and climate phenomena, and to anticipate errors in Week 2 predictions in various forecast models. This collaborative effort contributes directly to the "Special 2 week weather outlook" (http://www.crh.noaa.gov/ddc/wx/2week.txt) issued routinely by the Dodge City NWS Office. These Week 2 outlooks are produced using probability distributions of atmospheric circulation and other variables from Week 2 ensemble model forecasts to develop initial discussions of Week 2 conditions. The initial discussions are then diagnosed and modified to account for model biases using a suite of WWW-based products, including CDC maproom atmosphere angular momentum (AAM) and outgoing longwave radiation (OLR) products, that provide additional information on antecedent and existing conditions.

Synoptic experience indicates that low and high global AAM influences the variability of blocking and Rossby wave dispersion over the Pacific basin region.The Week 2 discussions use such synoptic insights to interpret the ensemble predictions and to determine the likelihood for systematic errors during particular regimes. Cases of good or bad Week 2 forecasts over the Pacific basin region are selected for more intensive study and diagnosis, always within the context of the phase of ENSO, the MJO, the seasonal cycle and Rossby wave dispersion. Additionally, in the last two winters Week 2 predictions of the Pacific basin circulation anomalies by the linear model discussed in Section 6.1.3 have provided unique insights into the role of tropical convection in forcing the extratropics. Aspects from an interesting case of this past northern winter are discussed below.

Figure 6.5 shows that during the last year ~50–70 day oscillations in global relative AAM have been prominent. These oscillations started in July 2000 and continue to the present (July 2001). They are superimposed on a persistent negative AAM anomaly (–1.5 sigma), reflecting weakened subtropical westerlies. The weakened westerlies coincide with cool (warm) sea surface temperatures in the tropical eastern Pacific (Indonesian region) and all have been present since ~August 1998. This easing of the subtropical westerly flow during the last 2 years opposes the observed trend in the NCEP/NCAR reanalysis during the last 30–40 years. The intraseasonal oscillations are closely related to the tropical convective forcing of the Madden-Julian oscillation, although not exclusively. Mid-latitude processes related to momentum transports, eddy feedbacks and mountains also force anomalies in global and zonal AAM and produce additional variability in the time series.

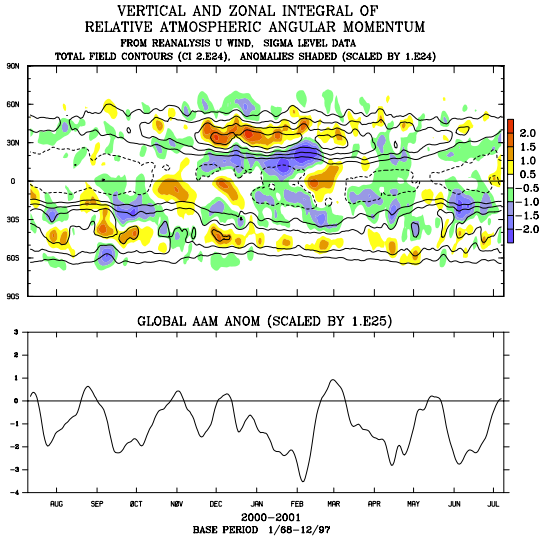

Fig. 6.5. (Top) Time series of the vertically and zonally integrated relative atmospheric angular momentum from July 2000–July 2001. (Bottom) Global atmospheric angular momentum anomalies since July 2000.

A prominent feature of the 2000–2001 northern winter, seen in the top panel of **Fig. 6.5**, is a large zonal mean anomaly pattern in the Northern Hemisphere. Starting in mid-November 2000, strong westerly flow develops in mid-latitudes (30°–50°N) with weaker than normal westerly flow in adjacent latitude bands. The easterly anomalies in the subtropics intensify and help drive global AAM to very low values during the winter period. Minimum values are reached in early February 2001, and are followed by a rapid rise to positive values during February 2001. Two physically significant events precede the rise.

In late January 2001, a strong MJO organized over the Indian Ocean and moved eastward reaching the dateline around 1 March 2001 (not shown). The evolution of the zonal AAM, seen in equatorial regions of **Fig. 6.5**, is consistent with the composite MJO. As positive convection anomalies move east across the ocean warm pool, zonal mean west wind anomalies develop on the equator and propagate poleward into the subtropics. MJO-related positive frictional and mountain torques contribute partially to the global AAM rise.

At about the same time (late January 2001) a subtle change occurs in the zonal mean flow at ~55°N as the easterly zonal wind anomalies transitioned to westerly anomalies. This subtle change initiates a chain of events that is represented synoptically by the composites in **Fig. 4.10**.

Stronger westerly flow over the mountains at 55°N produces topographic Rossby waves that move negative mass anomalies equatorward. Simultaneously upper level wavetrains amplify and disperse over the mountains and contribute to meridional momentum and heat transports. The resulting upper level momentum sinks in the subtropics tend to force easterly wind anomalies at the surface, i.e., a positive frictional torque, contributing another portion to the rise in global AAM. We suspect this is typical behavior for intraseasonal (20–90 days) AAM variations during northern winter, i.e., tropical MJO-induced forcing and extratropical transport-induced forcing both contributing to AAM changes.

6.2 Value added analyses and visualization tools

6.2.1 Climate Observations and Reanalysis

An important component of climate services is the development of visualization and analysis tools for the immediate synthesis and diagnosis of large operational climate datasets in near real time. CDC maintains a large and diverse collection of climate datasets in support of in-house research, which are also publicly available. Providing value-added access to high-quality, long-term records of observations is increasingly important to meaningfully evaluate climate system change, and to place such change in the context of natural variability. Outside users can download these data for further analysis; however, the amount of data available is often extremely large and not readily accessible without significant effort. CDC thus also provides a number of visualization and analysis tools that allow users to "test" out the data before going through the process of downloading. CDC's in-house scientific expertise provides insights into the types of questions climate researchers are investigating and the preferred WWW display and analysis tools to address these questions. A diverse number of visualization and analysis tools are available through the CDC Interactive Plotting and Analysis Pages (http://www.cdc.noaa.gov/PublicData/web_tools.html). A subset of these visualization and analysis tools plot data, or averages of data, over different times, allow users to specify the region, variable, type of plot (mean, anomaly, long-term mean, or time-by-latitude plots for example) and various other parameters. User-specified averaging over different intervals can be applied to study the average effects of phenomena such as ENSO (e.g., **Fig. 6.6**), or to examine possible decadal climate changes. On shorter time scales, users can systematically analyze synoptic variability or examine the current weather/climate in greater detail by

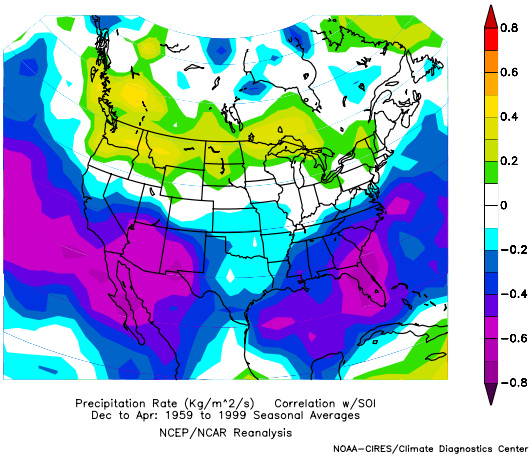

Fig. 6.6. WWW-based graphic generated using the correlation analysis tools to evaluate the relationship between NCEP Reanalysis precipitation and the SOI.

using a choice of the monthly mean compositing page, the daily compositing page, the US climate division dataset plotting page, the time section plotting page, the operational data plotting page, and the chi-corrected heating atlas. CDC also provides more sophisticated analysis tools such as a monthly correlation page, the US climate division correlation page, and a wavelet analysis page.

The correlation/regression analysis tools allow users to test (linear) relationships among the data and a suite of common indices of atmospheric or ocean variability (e.g., ENSO, PNA, or the AO), or a user-specified time series. The wavelet analysis tool allows users to examine the variability of some common atmospheric or user-provided time series. CDC also provides a WWW-based experimental climate services product that estimates the relative risks of extreme precipitation and temperature anomalies in relation to ENSO (e.g., the regional increased risk of extreme warm/cold or dry/wet, **Fig. 6.7**, http://www.cdc.noaa.gov/Climaterisks/).

All of these WWW tools are used extensively for research, for educational purposes by teachers, and to assess current or possible future weather and climate conditions by both public and private sector decision makers (e.g., energy companies, water managers). In addition, the plots and analyses generated by these pages have been presented at a wide variety of scientific meetings and have been incorporated in books and journal articles by both CDC and non-CDC scientists. The ideas generated by users able to quickly explore the data have made the CDC WWW-based visualization and analysis tools extremely useful and have saved much time and energy for researchers both outside and inside CDC.

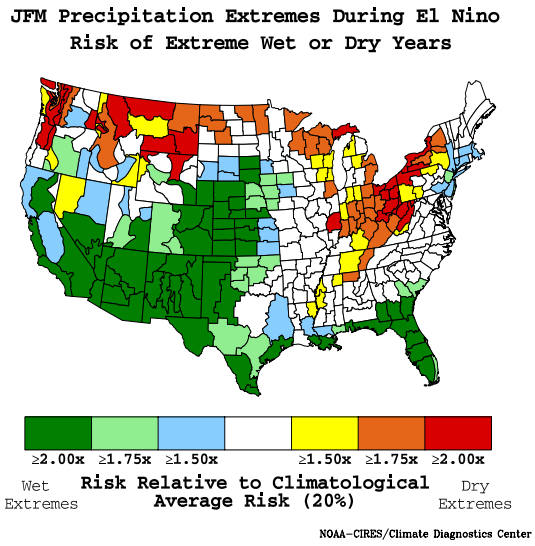

Fig. 6.7. Increased risks of precipitation extremes for Jan.-Mar La Niña conditions based on the SOI for 1896–1995. Relative risks at the 1.75x and 2.00x levels of either dry or wet extremes are significant at the 93.6% and 98.2% levels, respectively.

6.2.2 Climate Model Output

CDC has begun assembling large ensembles of climate model simulations of the 20th Century, many of which have been performed at other institutions, and making these data accessible to the research community for evaluation and intercomparisons. As part of this effort, CDC has developed a parallel set of WWW-based visualization and analysis tools to intercompare GCM simulations of climate, explore causal mechanisms for change in long-term observed records, and to establish the fidelity of model simulated climate. These WWW-based tools allow

considerable user interaction and manipulation of the data using CDC computing platforms. GFDL R30 resolution model climate simulations are currently available and may be intercompared with reanalysis climatologies (http://www.cdc.noaa.gov/gfdl). The GFDL data will be augmented to include AMIP-style simulations for 1950–1999, and runs using idealized SSTs. Also available on-line is the NCAR CCM3 AMIP climate model simulations spanning 1950–1999 with globally prescribed and tropically prescribed SSTs (http://www.cdc.noaa.gov/Composites/CCM). In addition to generating composites, the user can perform correlation analyses of the CCM3 response to various SST forcings (e.g., **Fig. 5.1**) at http://www.cdc.noaa.gov/Composites/CCM/Correlation/. Anticipated changes in computing infrastructure will permit an increasingly larger volume of climate model data to be made available on-line, and it is likely that CDC will increasingly host model data to support climate assessment research.

6.3 User Studies and Societal Interactions

CDC has conducted studies to evaluate the usefulness of climate information and products. This research is part of a broader effort to provide improved climate information to support more informed decision-making, and is designed to complement CDC climate diagnostics and modeling research. Initial studies have provided insights into how climate information and products are and could be used, while simultaneously identifying areas for research on experimental climate products (**Fig. 6.8**).

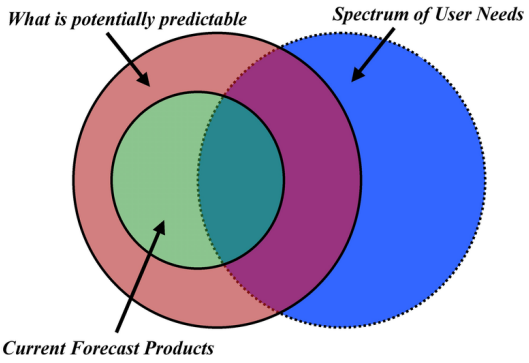

Fig. 6.8. Schematic showing the relationships among current products, potentially predictable climate information, and needed climate information. Directions for applied research are suggested by the purple overlap region.

6.3.1 Climate information and water management

CDC research has focused on the decision processes related to critical natural resource or society-relevant problems that are affected by climate. Goals are to learn what climate information is wanted and when, and how such information relates to specific decisions. In ongoing interactions with users, desired climate products are identified and the usefulness of prototype climate products is assessed.

One example of this strategy has been to focus on what is known about climate and integrate this information into our understanding of the annual cycle of reservoir management decisions (**Fig. 6.9**). In the Upper Colorado River Basin and Gunnison Basins, reservoirs that were originally built to provide reliable irrigation supply, hydropower, and recreation are now being operated to address addi-

tional concerns of maintaining appropriate flows for fish and water quality. Augmentation of spring peak flows and maintenance of late summer minimum in-stream flows in order to support the recovery of endangered fish are new issues in reservoir management. CDC has engaged reservoir managers seeking information to help address increasingly complex issues, and thus who are willing to consider new uses of climate information.

As illustrated in the decision calendar schematic (**Fig. 6.9**), NOAA long-lead precipitation and temperature forecasts can be incorporated into a fall forecast of winter snowpack accumulation with implications for subsequent April–June runoff. An improved understanding of ENSO influences on seasonal evolution of snowpack can lead to a more accurately planned "start of fill" target. By late spring, the NOAA long lead precipitation and temperature forecasts can be incorporated into summer season forecast irrigation demands. Throughout the spring one to two week precipitation and temperature forecasts can be used to provide improved estimates of volume and timing of spring releases needed to augment peak flows for habitat restoration and for flood mitigation. Throughout the summer, one to two week precipitation

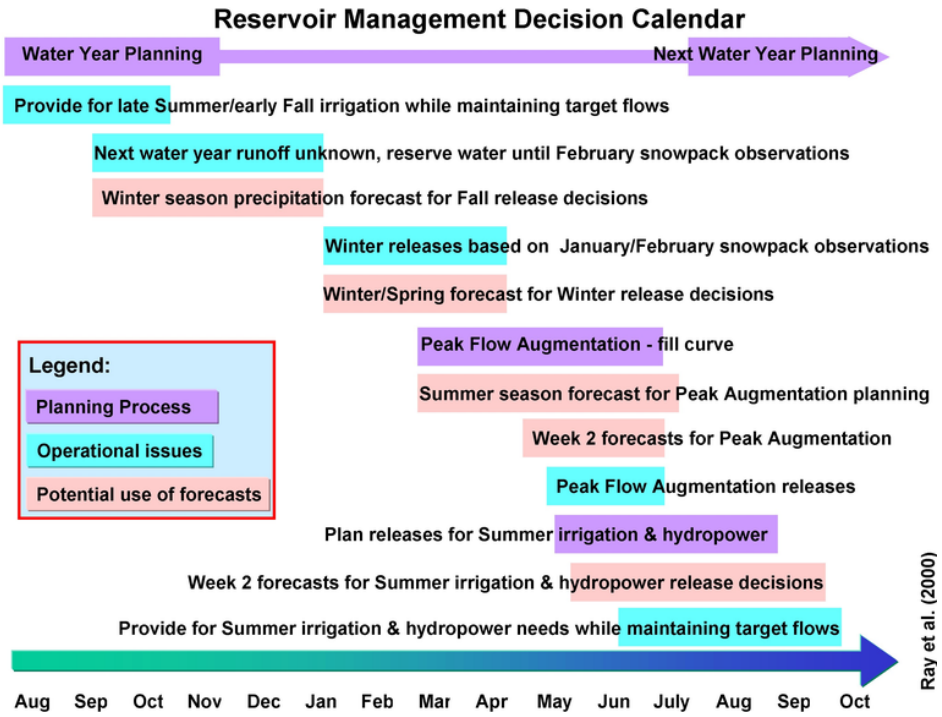

Fig. 6.9. The Reservoir Management Decision Calendar indicates the timing of select planning processes (purple bars) and operational issues (blue bars) for the Upper Colorado River Basin reservoirs. Also shown are the potential use of various types and timings of climate and weather forecasts (yellow bars) that could be used to address these concerns. The width and position of the bars indicate the intervals of relevant time periods. The distinction in classifying an activity in ones of categories: "Planning process" can be thought of as making strategic decisions in anticipation of upcoming events, whereas "operational issues" can be thought of as making tactical decisions on implementing a course of action in response to a near term event.

and temperature forecasts can be used to improve hydropower and irrigation scheduling, as well as low flow mitigation.

The decision calendar has proven useful in linking water resources management planning processes and operational issues with potential uses of variable lead-time forecasts and climate information. Future CDC climate applications research are anticipated to employ a similar approach, using the decision calendar framework to assess the role of climate information in decision-making related to energy, forest fires, air quality, and human health issues.

6.4 Western Water Assessment: A Regional Integrated Assessment for the Intermountain Western United States

CDC has collaborated with researchers from CIRES and the University of Colorado to develop the Western Water Assessment (WWA), an interdisciplinary research project linking climate, water resources, and society. The project is designed to do integrated interdisciplinary research and to interact with users in an effort to ensure society relevant research. The WWA, funded through the NOAA/OGP Regional Integrated Sciences and Assessments (RISA) program, represents an effort to forge genuine partnerships among the scientific community, climate service providers, and users. The goal is to provide the relevant climate/hydrology information that will support informed decision-making and thus reduce vulnerability to the impacts of climate variability and change.

CDC's WWA research has focused on the role of climate information for the decision-making process for water managers in the Upper Colorado River Basin. Colorado and the Interior West are ideally suited for a regional focus since the climate conditions (e.g., snowpack, timing of peak runoff, and extreme events) are orographically controlled. Investigations have evaluated the use of existing suites of climate predictions and products by the region's decision makers for specific sectors, and have undertaken the task of developing new products, or adding value to existing ones. The effort involves frequent interactions with users through regular briefings, workshops, coordination meetings, or web-enabled tools. The applied climate research aims to provide an improved regional description of climate and its variations on spatial and temporal scales that are relevant to users. Applied hydrologic research examines the role and evolution of snowpack, and identifies those predictable weather and climate patterns that influence variability in regional hydrographs.

6.4.1 User interactions

Over the past two years, CDC scientists have worked with managers of reservoir operations in the Upper Colorado to determine how climate information might be used more effectively throughout the water year. These user studies involved: a) direct participation in planning by attending and or hosting reservoir management meetings, b) partnering with the Denver Water Board and Colo-

rado River Water Conservation District to hold a workshop focused on the use of climate information and seasonal forecasts in water resource management focused on endangered fish habitat restoration, c) preparation of "Climate Forecast Discussions for the Upper Colorado Basin" for distribution to USBR and other interested water managers, d) providing briefings on climate forecasts and current status to the Colorado Drought Task Force and various water resource coordination meetings for the Upper Colorado Basin, and e) focused user studies described previously. These activities, while labor intensive, have established the needs and potential uses of forecasts and climate information in water resource management. The next step will be to incorporate climate forecasts and information into the NOAA Colorado Basin River forecasts used by reservoir managers. On-going activities are focused on implementing a technology transfer process to integrate seasonal climate information into river forecast procedures. A collaborative effort with the Colorado Basin River Forecast Center, in Salt Lake City is envisioned following an iterative process of identifying prototype climate products needed by the River Forecast Centers and then developing applied climate research products.

6.4.2 Regional climate variability

Identified user needs and interests in regionally based climate information have helped motivate research to enhance understanding of climate variability in the intermountain western US. CDC researchers have performed empirical analyses on western U.S. precipitation patterns (derived from historic climate station and automated SNOTEL data) at a number of spatial and temporal scales to document and provide insights into patterns of observed range of climate variability. These analyses have concentrated on the South Platte and Upper Colorado River basins, and have also assessed higher elevation climate records relative to more continuous low elevation sites (**Fig. 6.10**). Results for Colorado reveal relatively low temporal variability in the regionally important winter precipitation season at high elevations (red/orange colors), which contrasts with more variable winter precipitation at lower elevations (blue/green) colors.

CDC researchers also developed hydroclimatically based experimental "climate divisions" using multivariate analysis of the annual cycle of precipitation in order to improve monitoring of the seasonal evolution of precipitation across Colorado (**Fig. 6.10**). The resulting experimental "climate divisions" regions explain more than half of the average local precipitation variance. Since each regional average explains more precipitation variance than the operational divisional time series, these internally consistent experimental regions are proposed as alternative to existing climate divisions to monitor the seasonal evolution of precipitation.

6.4.3 Regional hydrologic variability

Identified user needs and interests in regionally based climate information also have helped motivate research focused

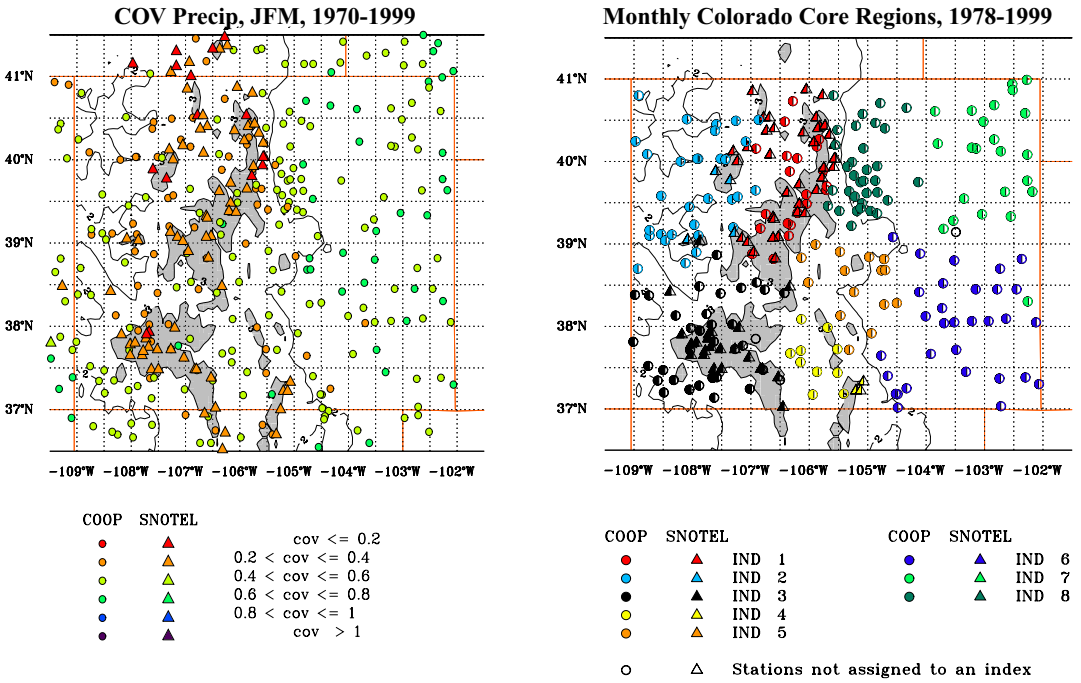

Fig. 6.10. Wintertime coefficient of variation for precipitation data at individual Colorado stations (left panel) and proposed experimental "climate divisions" based on multivariate analysis of the annual cycle of precipitation (right panel). The low wintertime coefficient of variation in the left panel indicates reduced interannual variability. The colors in the right panel correspond to individual experimental "climate divisions" and the amount of color for each symbol reflects the amount of variance explained at individual stations by the experimental "climate divisions" regional precipitation index.

on the potential for predicting the magnitude and timing of late spring/early summer peak runoff. The observed hydrologic regime in the upper Colorado River Basin is driven largely by the cold season snowpack dynamics, warm season melt, and characteristic space-time scales of relevant weather and climate precursors. Seasonal streamflow variations and peak floods in the West reflect an integration of seasonal-to-interannual climate influences (through snowpack development in the cold season) and weather patterns on month-to-seasonal time scales (responsible for snowmelt in the spring). The magnitude and timing of springtime peak streamflow represents the joint influences of the wintertime climate (as reflected in the snowpack), and the springtime weather patterns that aid in the melting of snowpack. Diagnostics and monitoring of intraseasonal-to-interannual hydroclimatic variations in the Yampa River drainage have shown consistent relationships between the April 1 snowpack and April–July streamflow. Analysis of historical records suggests that over 60% of the observed variations in streamflow can be explained by a linear snow-streamflow relationship (**Fig. 6.11**).

The large-scale climate controls on extreme (high and low) snowpack years in the Yampa River Basin can be interpreted in terms of composite SST anomaly patterns. Low snowpack occurs during winters with anomalously warm

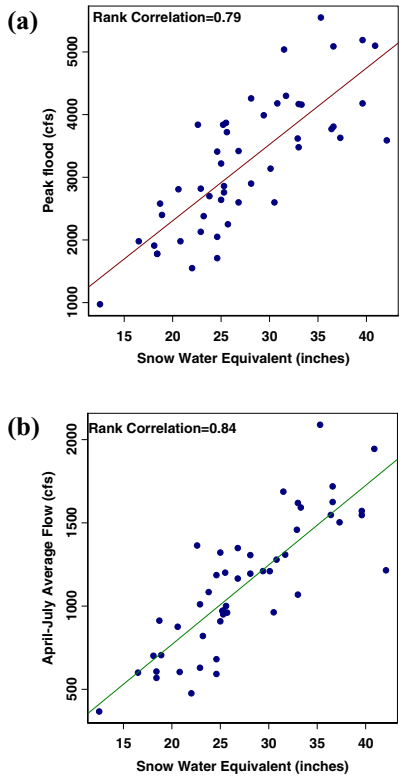

Fig. 6.11. Yampa River streamflow: relationship between April snowpack at Rabbit Ears snow monitoring station and Maybell, Colorado streamflow. (a) Relationship between April 1 snowpack and subsequent snowmelt peak flow. (b) Relationship between April 1 snowpack and April–July streamflow.

tropical Pacific and a cold North Pacific. High snowpack years are associated with warm North Pacific SST and a cold tropical Pacific SST anomalies. Ongoing research is investigating: (a) the associated winter and spring variations in intraseasonal precipitation and temperatures to assess the risk for extreme surface hydrologic variations, and (b) the underlying mechanism for the associated patterns of SST anomalies and their predictability, to aid snowpack predictions.

Streamflow during the April–July melt season is driven by regional temperature patterns that determine the shape of melt hydrograph and the timing of peak flow. The timing of peak flow (or annual maximum flood) is critically important for reservoir operations and assessing downstream flood potential. Preliminary analysis suggests a causal relationship between the regional temperatures and the timing of peak flow. In the Yampa region, a three-to-five day lag is observed between the temperature and snowmelt-driven streamflow. Further, the amplitude of Eastern Pacific and Pacific North American teleconnection patterns (April) show a statistical relationship with the date of peak streamflow. The results from these analyses point to the potential for modeling and forecast of snowmelt and the timing of peak flows, based on a detailed analysis of medium-range temperature variations and available forecast products. Near real-time monitoring of the relevant hydroclimatic variables and CPC temperature forecasts for the Yampa region are now available on the WWW (http://www.cdc.noaa.gov/~sjain/waterpulse/).

6.5 Public Health and Climate Research

During the last decade, there has been considerable interest in better understanding the possible impacts of climate variability on public health. This interest has evolved into a basic research component within the CDC experimental climate services portfolio. These interdisciplinary research activities not only provide a better understanding of

the relationships between climate variability and human health, but also guide climate research to ensure the development of the climate information needed to better forecast or monitor potential public health crises.

6.5.1 Precipitation and encephalitis

CDC is currently collaborating with epidemiologists at the University of California at Davis and the Scripps Institution of Oceanography on possible associations between interannual precipitation changes and variations in the incidence of western equine encephalitis (WEE) in the Central Valley of California. WEE and SLE (St. Louis encephalitis) are mosquito-borne diseases endemic in California. Human vaccines and therapeutic drugs currently are not available for the viruses, and vector abatement remains the only method of controlling human infection. Vector abatement relies strongly upon accurate surveillance of environmental conditions to provide sufficient warning to implement intervention. Amplification of encephalitis viruses to levels that place the human population at eminent risk of infection depends on the rate of virus replication in the mosquito host. The replication rates are related to temperature and mosquito population size which in turn are related to surface water availability. Improved understanding of global (and tropical Pacific) atmospheric teleconnections, the use of numerical model guidance for long range forecasting of climatic conditions in California, and the availability of short-range forecasts in conjunction with hydrological models, can collectively provide accurate depictions of snowpack and run-off. Quantitative relationships between climate and enzootic virus amplification are being developed retrospectively to forecast the level of virus activity during the principal transmission seasons of spring and summer.

6.5.2 Climate variability and Kawaski disease

A second collaborative research project with the University of California at San Diego and Scripps is to improve current understanding of the possible link between weather and climate variability and Kawasaki Disease (KD), an acute illness of the circulatory system primarily affecting infants and young children. A winter and spring seasonal KD peak has been recognized for over two decades, but recent studies suggest an association at synoptic time scales as well. KD incidence data for San Diego County from 1994 to present shows a moderate correlation with precipitation. The distribution of cases is characterized by the presence of clusters in which multiple KD cases occurred within a time interval of just a few days. Fifteen clusters occurred during the cool season (November–April) between 1994 and 2000. Weather patterns were examined starting 6 days before and continuing through 6 days after the date of KD onset (first day of fever is designated day 0) for the first child in the cluster. The composite patterns were compared to a second control sample of randomly selected days for the same cool seasons (1994–2000), but during prolonged periods with no KD events. The 700mb height anomaly field was composited over the 15-event sample set. The atmospheric circulation pat-

tern preceding the occurrence of KD data clusters exhibit strong negative anomalies over the North Pacific upstream from San Diego (**Fig. 6.12, left panel**), indicating an active storm track and typically wet conditions in San Diego County. This pattern appeared to be developing by Day –6, was very strong on Day –4, and then persisted, though weaker, for several days thereafter. In contrast, the composite from control sample days extracted from the non-KD periods shows no significant anomaly pattern in atmospheric circulation over the Pacific (**Fig. 6.12, right panel**). Inspection of the 15 individual KD clusters revealed precipitation of at least 0.1" associated with 10 of the clusters. These results warrant further investigation and exploration of other variables (humidity, cloud cover, minimum temperature, time elapsed since last significant rain storm) in relation to KD clustering.

CDC scientists are also part of an international regional network to foster interdisciplinary research to better understand the relationships between climate variability and human health in the Americas. As part of a five-year project funded by the InterAmerican Institute for Global Change Research, a major effort is underway to develop a database of climate and selected human diseases, primarily vector borne diseases, such as malaria and dengue fever, to allow diagnostic studies and monitoring activities to be carried out.

EPILOGUE

CDC is uniquely positioned within NOAA's emerging climate services. Through its diverse research in climate diagnostics and analyses, CDC is an extensive user of new and enhanced climate forecasts and products. Participa-

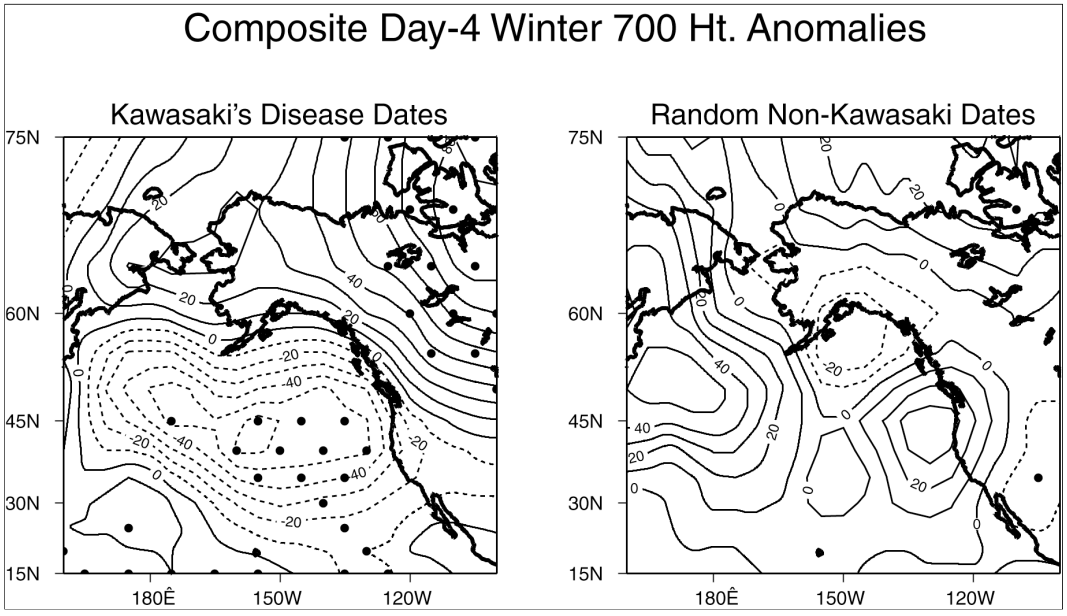

Fig. 6.12. Composite 700 mb height anomalies, 4 days prior to the onset of KD case clusters in San Diego County. Dots denote significance of being different from the null hypothesis (zero anomaly) with 90% (or greater) confidence by a t-test.

tion in the NOAA-CIRES western water regional integrated science assessment project engages CDC in research to identify gaps between climate information and societal needs, and to develop decision support services that make climate information and products more useful. Finally, as an experimental provider of climate services, CDC is developing the infrastructure and expertise to provide improved access to climate and weather products for use by the scientific research community and less traditional users.

CDC will continue to develop experimental research products that meet the needs of both the scientific research community and less tradition users of climate information and forecasts. To ensure improved regular and systematic communication of needed climate information, CDC will work to formalize partnerships within NOAA and outside of NOAA. Within NOAA, enhanced interactions with OAR (e.g., GFDL and ETL), NESDIS (WRCC and NCDC) and NWS (NCEP/CPC and RFCs) will ensure the development of experimental climate monitoring and forecast products that can be used by, and then transferred to, operational distribution centers. As climate science matures, there is a greater awareness in society of the importance of climate, and the emerging role for climate information in decision-making related to energy, forest fires, air quality and human health, and water resources management. Although these are national issues, there is a growing recognition that providing an improved scientific basis for public planning and policy decisions will require regionally specific climate information and products designed to meet local, state, and regional interests. In collaboration with WRCC, CDC will continue to expand the links between fundamental climate research and regional applications to society-relevant problems, including the timely and routine transfer of data, products, and information to current and future user communities. Enhanced partnerships between CDC and university-based regional climate assessment activities, as well as identified stakeholders in the West, will be essential to accelerate the increased flow of climate information to support decisions. In-house research at CDC will continue to work directly with active, or potential, users of climate information to improve the understanding and usefulness of climate information while identifying areas for research to develop new and improved experimental climate products. In addition, CDC research will be expanded to identify the possible impacts of climate variability on public health and to develop climate products that better forecast and monitor potential public health crises.

***Contributed by**: G. Bates, H. Diaz, R. Dole, M. Hoerling, S. Jain, L. Matrosova, M. Medovaya, M. Newman, C. Penland, R. Pulwarty, X. Quan, A. Ray, A. Roubicek, P. D. Sardeshmukh, R. Schweitzer, J. Scott, C. Smith, R. Webb, K. Weickmann, C. Winkler, and K. Wolter.*

CHAPTER 7

Computing, Network, Web, and Data Services

7.1 Computing Services

CDC operates a centralized computing facility, based on high-end UNIX workstations, that emphasizes shared resources and is designed for the benefit of all CDC science projects. The goal of CDC's systems services is to provide near state-of-the-art computational and storage facilities and to accomplish this within a target budget that is 15% of CDC's total budget. The purpose of CDC's systems services is to allow CDC to efficiently fulfill its mission and research obligations and to enable CDC scientists to compete effectively with their peers at other institutions. Resource allocation and policy issues are considered by an internal CDC review group, the Computer Users Advisory Committee (CUAC), that makes recommendations to CDC's systems and upper management.

The bulk of CDC's computer facility investment is in mid-range computing, utilizing a tightly integrated network of Unix workstations and servers (**Figs. 7.1 and 7.2**). Total capacity of this system is approximately 18-Gflops of aggregate throughput, with 2.4-Gflops peak symmetric multi-processor (SMP) through-

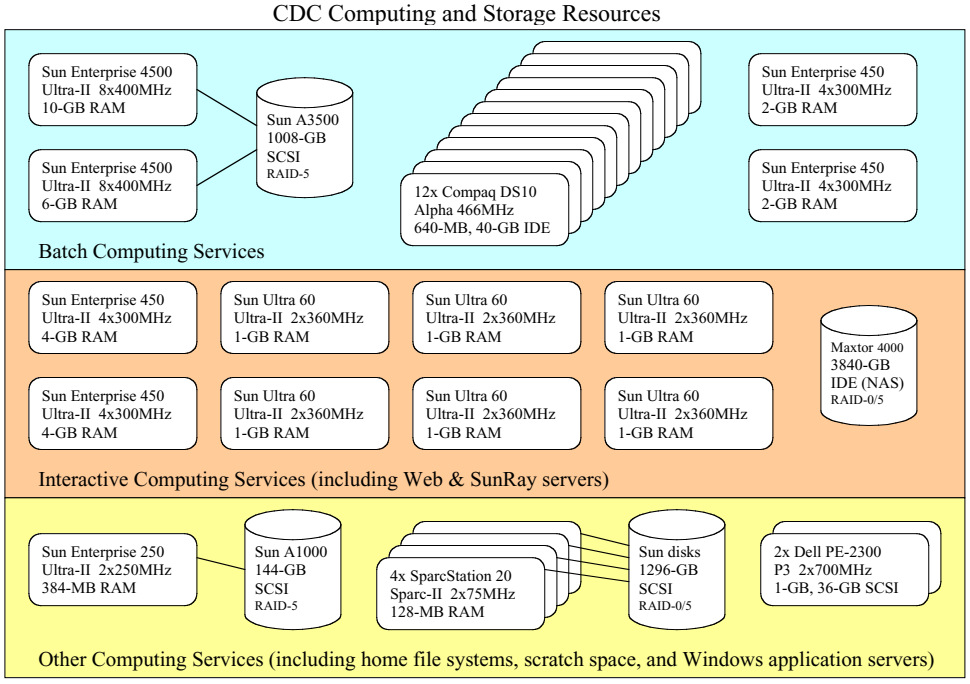

Fig. 7.1. Schematic overview of CDC's computing services and resources.

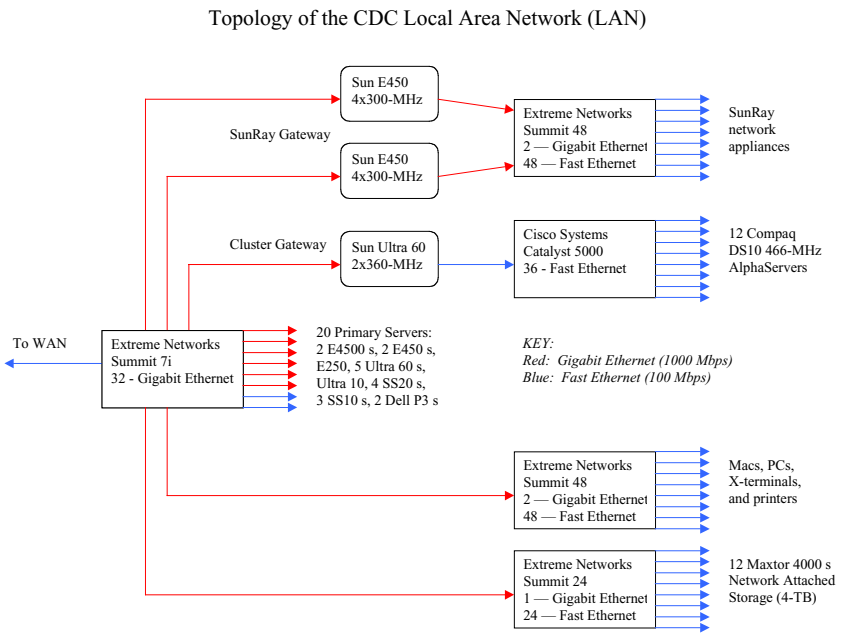

Fig. 7.2. Schematic depiction of CDC's local area network.

put on each Sun Enterprise 4500 and 525-Mflops peak single-processor throughput on each node of our Compaq DS10 Alpha-cluster. Comparable figures for CDC from four years ago are 1.75-Gflops aggregate, 250-Mflops SMP peak, and 125-Mflops single processor peak, respectively. Total aggregate and SMP throughput have increased by an order of magnitude. **Table 7.1** shows the breakout of CDC computing power (in units of aggregate DP LINPACK) by type of processor. Note that one Sun Enterprise 4500 is configured as a large memory machine with 10-GB of RAM.

Industry trends are allowing CDC to increasingly provide traditional super-computing-class services in-house using commodity workstation technologies. In 1999, when a computer-room fire disabled the National Weather Service's CRAY C-90 supercomputer used for operational forecasts, CDC was able to implement a replacement for the week-two ensemble model runs and allowed NWS to continue issuing short-term climate forecasts until their own systems were repaired. CDC accomplished this using six dual-processor Sun Ultra 60 computers dedicated to the task. Lately, several CDC researchers have brought their compute-intensive modeling activities in-house, as external supercomputer facilities have become less cost effective, outmoded, or have switched to massively parallel processor (MPP) technologies that may require significant recoding (e.g., the National Center for Environmental Prediction's IBM RISC-cluster and the Forecast Systems Laboratory's HPTI Alpha-cluster). Since MPP facilities often employ large numbers of workstation-class processors, it is fairly easy to create small clusters of these same processors that come close to the per-processor performance of their larger brethren, at a fraction of the cost. This

Table 7.1: CDC Primary Computing Resources

CONFIGURATION	CPUs	LINPACK
Compaq Alpha DS10 (12 nodes)	12 x 466-MHz	6.30-Gflops
Sun Enterprise 4500 (2 nodes)	16 x 400-MHz	4.80-Gflops
Sun Ultra 60 (6 nodes)	12 x 360-MHz	3.25-Gflops
Sun Enterprise 450 (4 nodes)	16 x 300-MHz	3.60-Gflops
TOTAL		**17.95-Gflops**

economy is especially true if the computing can be done as a "loose cluster" which uses traditional Ethernet LAN technology for the inter-processor communications. Ensemble model runs are well suited to loose clusters, since each invocation of the model can be run independently on its own processor. Thus, in the past year CDC has concentrated its modest financial resources on providing this type of high-end computing. For example, for typical ensemble model runs, total throughput on our 12-node Compaq DS10 Alpha-cluster is close to 6 Gflops, with a total acquisition cost of only $60,000. For high-end computing needs that cannot easily be met within CDC, some users continue to make some use of outside facilities, primarily at NCEP, FSL, and NCAR.

Several smaller machines, not included in the general computing category, are dedicated to specific functions to minimize system downtime, segregate competing demands, and to maximize system security. For instance, various servers specialize in electronic mail, anonymous-FTP (file transfer protocol), NIS (network information services), DNS (domain name service), tape backups, and NFS (network file system) mounting of the users' home file systems. Two of the general-purpose Ultra 60 servers also act as fully redundant hosts for the CDC web site.

Total on-line (raw) disk storage capacity is approximately 12.5 TB, of which nearly 6 TB is a Dell storage area network (SAN) device that was acquired as excess property from the 2000 Census, but is still in the process of being brought on-line at CDC. The Dell SAN will be used to host climate model output for ease of model intercomparisons and for efficient generation of model diagnostic statistics. CDC's next largest category of disk storage, at 3.8 TB, is composed of newly acquired Maxtor network attached storage (NAS) devices. Each device is basically a stripped down PC with four large disks in a 1U (1.75" high) rack-mount form factor. These NAS devices can be procured for $3200 for 320 GB or approximately a penny per megabyte.

Although they do not provide fast throughput, they are a convenient alternative to magnetic tape. In 1997, total CDC disk capacity was 600 GB of traditional magnetic disks and 400 GB of fairly slow magneto-optical disks. A breakdown of CDC's current magnetic disk storage is shown in **Table 7.2**.

For large data sets that are of interest to only one or two PI's or for archival purposes, users have access to a variety of tape devices: eight DLT-7000 drives, including two auto-loading stackers, six 8-mm Exabyte drives with one stacker, and a 4-mm DAT drive. An IBM-style 4380 drive and stacker is also available to support the occasional ingest of 1/2" square-cartridge tapes. In addition, systems staff uses two Exabyte Mammoth-2 20-slot tape jukeboxes, dedicated to systems backups, with a total single-pass backup capacity of 2.4 TB. All of the users' home file systems, containing their programming code and executables, are incrementally backed up nightly, while the users' data files are backed up approximately once a month. Since 1997, CDC has discontinued support for 1/2" open-reel tapes and 1/4" cartridge QIC tapes.

Systems users have a variety of printing options through the network, including standard monochrome laser printers, both solid-ink and laser color printers, a large-format color ink-jet poster plotter, and a 65-ppm Xerox digital copier that can also staple the output. Color flatbed scanners with optical character recognition software, a very large digitizing tablet, and a bar-code scanner are available as alternative input devices.

There are three solutions provided for desktop computing, depending on the user's needs. CDC's administrative officer and secretaries use PCs that have specialized software for budgetary, personnel, and procurement record keeping. If scientists or their support staff have a strong predisposition to the

Table 7.2: CDC Primary Disk Storage

TYPE	DISKS	CAPACITY
Dell SAN (RAID5)	160 x 36 GB	5760 GB
Maxtor NAS (IDE)	48 x 80 GB	3840 GB
Sun A3500 (RAID5)	56 x 18 GB	1008 GB
Sun A1000 (RAID5)	8 x 18 GB	144 GB
Sun 6-PACKS	36 x 18 GB	648 GB
Sun 6-Packs	72 x 9 GB	648 GB
Alpha-cluster (IDE)	12 x 40 GB	480 GB
TOTAL		**12528 GB**

MacOS look-and-feel, they are provided with Apple Macintosh computers and Citrix client software to access the other CDC systems. Most users, however, are provided with SunRay network appliances. The SunRay has the look-and-feel of a traditional Sun workstation console and can be set up to support a variety of window environments, such as CDE or FVWM, much like an X-terminal. In reality, the SunRay is a further abstraction of the X-terminal concept. Instead of complex X11 calls being transmitted from a server to the user's desktop client, in the SunRay paradigm, only the frame buffer calls are transmitted from the server to the desktop. The hardware components in a SunRay box are those necessary to interface with user: video out, video in, audio out, audio in, keyboard and mouse. These components have been engineered to the limits of human perception, so, in theory, a SunRay will never need to be upgraded. The SunRay costs $350 and takes only minutes to replace if one should fail. A "smart-card" capability allows users to transfer their active session from one SunRay device to another for the purpose of collaboration or presentation. For all of our users, whether on a PC, Mac, or SunRay, CDC provides high-resolution LCD flat-panel displays to reduce eyestrain, glare, energy consumption, and hazardous emissions.

To supply typical office productivity software, CDC operates two dual-processor 700-MHz Pentium-III PCs, running the Windows 2000 Terminal Server Edition (TSE) operating system. Via Citrix, these servers provide access to Microsoft Word, Excel, PowerPoint, WordPerfect, Quatro Pro, Corel Presentations, Systat, Netscape, and Internet Explorer to our SunRay and Macintosh users. All of the Sun systems are running the Solaris 7 or Solaris 8 Unix variants. These Sun operating systems are scrupulously updated with the latest security patches to provide a high level of system integrity. All unnecessary network services are disabled and an automated security check is routinely performed to detect unauthorized attempts to gain access to the CDC systems. Software provided on the Sun systems includes FORTRAN (77, 90, and 95), C, and C++ compilers, IMSL, NAG, IDL, Matlab, Splus, Maple, NCAR Graphics, and GrADS. Other, publicly licensed software (freeware and shareware) available to users on the Sun systems totals 15 GB. The Compaq Alpha cluster runs the Linux operating system, which is considered a potential security weakness. To minimize the risk, CDC has placed the Alpha cluster behind a Sun Ultra 60 running Solaris, which serves as a gateway to separate the cluster from the rest of the CDC local area network. A user must successfully log into the Solaris box to "see" the Linux boxes. The Alpha cluster provides minimal software for the user - only a single FORTRAN compiler. The Alpha cluster and the high-end Sun systems are limited to batch-only jobs. To access the batch machines the user submits their job to the PBS scheduler, which routes the job to the most appropriate computing resource. Once a job starts running on a given processor, it generally will run to completion without swapping. This technique maximizes total system

throughput by reducing the system overhead for each job run.

System downtime at CDC has been fairly minimal in the last few years. Redundancy has been designed into much of the systems infrastructure (e.g., two SunRay servers, two web servers, two Enterprise 4500's, two Pentium servers, and disk arrays using RAID-5). If something breaks, users can usually still get work done. Preventative maintenance and hardware/software upgrades are scheduled and performed by CDC systems staff one evening per month. All critical hardware systems are on maintenance contracts with the manufacturers. CDC also keeps a supply of "hot spares" for many commodity hardware components.

7.2 Network Services

CDC's network facilities can be divided into the internal Local Area Network (LAN) and the connectivity to the Wide Area Network (WAN). Heavy reliance upon centralized computing resources, with minimal computing power on the individual's desktop, requires dependable, high-bandwidth networking to maintain user productivity. Access to remote computer systems at NCEP, NCAR, and GFDL and the importance of CDC on-line data sets and graphical web products to external users dictate that CDC also requires adequate connectivity to the Internet.

CDC is in the fortunate position of having considerable control over its internal LAN wiring. Although LAN equipment was provided to CDC as part of the move to the new David Skaggs Research Center (DSRC) in March 1999, it quickly became apparent that a mixture of Asynchronous Transfer Mode (ATM) and Ethernet protocols within the LAN and the use of edge switches in the role of core switches were not providing CDC the level of service needed. Consequently, with the advent of inexpensive copper-based Gigabit Ethernet technology, CDC completely replaced their LAN in 2000 for approximately $45,000. The new LAN (**Fig. 7.2**) features an Extreme Networks Summit 7i Gigabit Ethernet switch at its heart. The switch provides 28 1000BT (copper wire) ports and four 1000SX (fiber cable) ports. The 7i's backplane can handle all active ports at full wire speed. Most of CDC's Sun servers are connected directly into the 7i to provide high-bandwidth for the NFS (network file system) traffic between the user's running job and the user's data files. Other Gigabit links go to Fast Ethernet concentrators, the Extreme Networks Summit 24 and a Summit 48. The Summit 48 provides 48 Fast Ethernet ports for the desktop PC's, Mac's, and printers. The Summit 24 connects to our 12 Maxtor NAS devices, with plenty of room for expansion. Another Gigabit link from the 7i goes to a Sun Ultra 60 that serves as the gateway to our Compaq Alpha-cluster. This Sun gateway serves to shield the 7i from the Linux operating system on the Alphas. The Alphas are connected to the Ultra 60 using a Cisco Catalyst 5000, our only holdover from our former location on the CU east campus. Finally, two Gigabit links go from the 7i to the two SunRay servers. The SunRay architecture requires a private LAN for communication between the SunRay server and the SunRay desktop

clients. CDC utilizes an Extreme Networks Summit 48 for this purpose. The Summit 48 has been configured so that if one of the SunRay servers fails, the SunRay users are still able to log on to the other SunRay server. In 1997, each office user had access to an Ethernet (10-Mbps) line shared with nine other users or devices. Today, each office user has a dedicated Fast Ethernet (100-Mbps) line.

For connections to the outside world, CDC takes advantage of the excellent connectivity provided by the DSRC's ATM backbone and the Boulder Research and Administrative Network (BRAN), a fiber-based metropolitan-area network that CDC helped create (see **Fig. 7.3**). The DSRC ATM backbone provides OC12 (622-Mbps) links between CDC and the other building tenants, including the Forecast Systems Laboratory (FSL), the Aeronomy Laboratory (AL), and the National Geophysical Data Center (NGDC). An OC3 (155-Mbps) link via BRAN connects the DSRC backbone both to the University of Colorado-Boulder and to NCAR. Both of these institutions are connected at OC3 speeds to the Front Range GigaPOP (FRGP), which provides connectivity to the commercial Internet via Qwest and to the Next Generation Internet (NGI) in the form of Abilene. If problems develop at the FRGP, the DSRC backbone can switch to a secondary route though FSL, albeit at fractional T3 (6-Mbps) speeds. A bottleneck for CDC is caused by the connection from the CDC Summit 7i to the DSRC ATM backbone. At present this is only a Fast Ethernet (100-Mbps) connection. Despite this, CDC, which represents only 5% of the DSRC's occupants, has accounted for 28% of the total network traffic through the DSRC's gateway to the outside world over the past

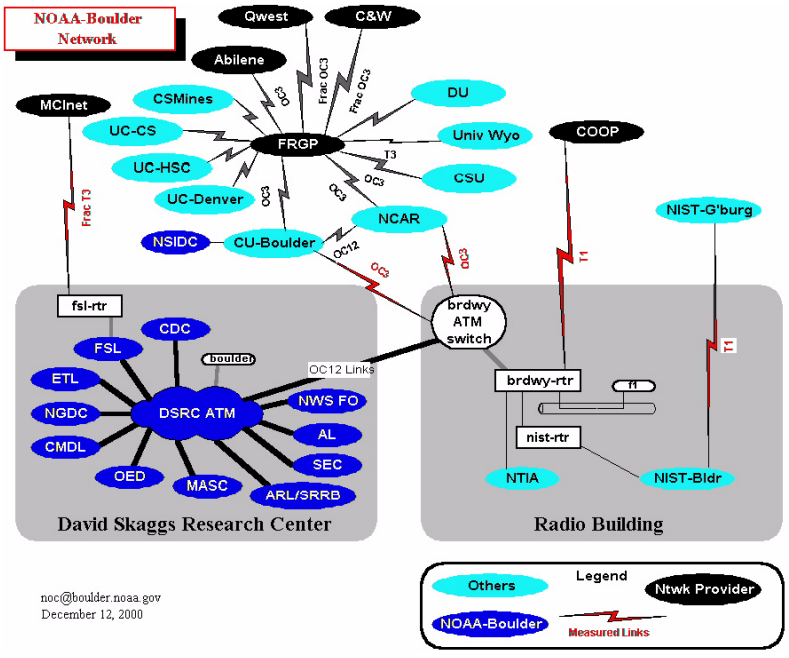

Fig. 7.3. Layout of the NOAA-Boulder Network.

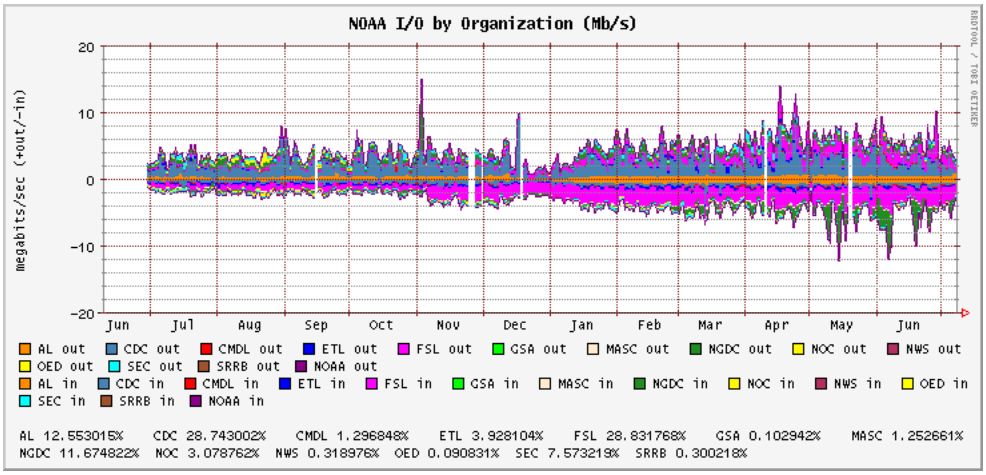

Fig. 7.4. Network traffic into and out of the DSRC over the past year.

year (**Fig. 7.4**). Most of this traffic has been outbound, meaning transfer of information from CDC to the rest of the scientific community and to the general public. Only FSL can equal CDC's network traffic through the DSRC gateway, but most of their traffic has been inbound on that link. In the near future, the DSRC network operations center is planning to upgrade our 100-Mbps bottleneck to a 1000-Mbps Gigabit Ethernet connection.

7.3 Web Services

CDC's systems and data management groups provide the infrastructure and support for CDC's primary and subsidiary web sites. The primary web site (http://www.cdc.noaa.gov/) is generated using a set of document templates which result in a consistent site look-and-feel and ensure compliance with Federal policies and regulations. A recent example of a Federal policy is the prohibition on the use of "cookies," which deposit information on the end user's computer. An example of a regulation is the Federal Acquisition Regulation which implements Section 508 of the Rehabilitation Act of 1973. Currently, the CDC webmaster is responsible for tracking these various directives and translating them into meaningful courses of action. Our document structure provides a central point of change if the document layout and navigation schemes need to be modified to comply with changing policies and requirements. This allows local scientists to concentrate on content generation, and not, for example, on the need to add links to "disclaimer" and "privacy" statements. These high-level links are included in the document templates and hence automatically included in any document which is generated using the templates.

The CDC webmaster, and the broader data management group, are also tasked with staying abreast of technology trends in the rapidly evolving area of web site architecture and management. CDC actively participates in and often helps organize opportunities for web technology exchange, including the OAR Tech-

nical Committee on Computing Resources (TCCR), OAR Web Workshops, NOAA Web Workshops, NOAA Tech Workshops, the Federal Webmasters' Conference series, WWW Consortium meetings, and the American Meteorological Society (AMS) Interactive Information and Processing Systems (IIPS) Conferences. CDC has also been a leader within NOAA in the investigation and, if warranted, local deployment of Java, JavaScript, Java Server Pages (JSP), XML, webcasts, and digital certificates. The CDC web site underwent a major makeover this year to improve site navigation and to incorporate better support for some of these new technologies.

Subsidiary web sites are those which are largely autonomous sites hosted on the CDC web server. They serve a broader institutional purpose but are maintained by CDC staff. These sites include the COADS web site (http://www.cdc.noaa.gov/coads/), the Metropolitan Denver Combined Federal Campaign (CFC) web site (http://www.cdc.noaa.gov/cfc/), the AMS Committee on IIPS (http://www.cdc.noaa/gov/iips/), and a NOAA-level site devoted to the NOAA Strategic Goal on "Seasonal to Interannual Climate Prediction" (http://www.cdc.noaa.gov/seasonal).

The success of the CDC web site(s) can be measured to some degree by tracking the number of files served, often referred to as "hits." Since its inception, the CDC web server has seen almost exponential growth in the number of documents served to outside users (**Fig. 7.5**). Current "hits" are in the range of two million per month, about six times the rate of four years ago.

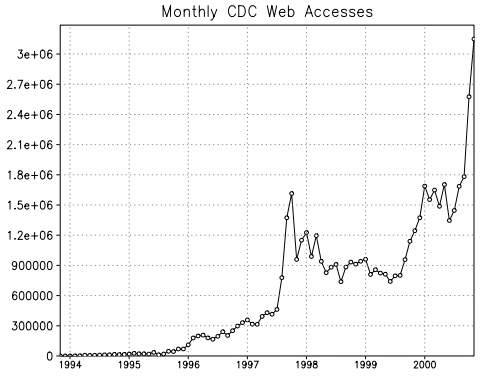

Fig. 7.5. Total number of "hits" per month for all of CDC's web pages.

7.4 Data Services

While many CDC scientists adequately manage their own data needs, there are many instances where shared data sets and shared data expertise make cooperation on data management issues highly desirable. To that end, CDC provides data management services to acquire, ingest, store, and maintain a wide variety of climate-related data sets at CDC. Most data sets, so maintained, are made available to CDC's internal users as directly accessible files and to outside collaborators through anonymous-FTP or tape copies. Over the past four years, the CDC web site has become the primary method by which external users locate, browse, and download CDC's diverse data holdings. CDC's Computer Users Advisory Committee (CUAC) provides advice to the data management group on which data sets to include in the centrally managed on-line data archive. Currently

supported data sets are detailed in **Table 7.3**.

CDC data management has standardized much of its data work in the netCDF format. NetCDF was chosen because of its widespread use in the atmospheric sci-

Table 7.3: Summary of Cooperatively Managed Data Sets at CDC

DATASET TITLE	SIZE (GB)
Climate Diagnostics Data Base	1.70
CPC Merged Analysis of Precipitation	0.15
CPC .25 x .25 Daily US Unified Precipitation	1.94
Comprehensive Ocean-Atmosphere Data Set (COADS)	62.85
DOE Gridded Surface Precipitation and Temperature Anomalies	0.05
DAI Palmer Drought Severity Index	0.05
ECMWF (non-public)	1.48
GFDL Consortium Derived Products	0.31
GFDL Consortium (non-public)	1.55
Global Sea-Ice and Sea Surface Temperature (non-public)	0.39
Hadley Sea-Ice and Sea Surface Temperature (non-public)	0.39
NOAA Interpolated OLR	0.22
Kaplan Sea Surface Temperature	0.01
Monterey Marine Real-time Marine Data	0.33
Microwave Sounding Unit (MSU) Data	0.61
NCEP Daily Global Analyses	16.09
NCEP GCM T42 MRF1 (non-public)	0.02
NCEP Pacific Ocean Analysis	1.66
NCEP Real-time Marine Data	0.23
NCEP/NCAR Reanalysis Products (4x daily)	393.45
CDC Derived NCEP/NCAR Reanalysis Daily Averages	80.94
CDC Derived NCEP/NCAR Reanalysis Monthly/Long-term Means	5.99
NCAR Daily Observed SLP daily data (non-public)	0.09
NOAA Highly Reflective Clouds	0.47
NODC World Ocean Atlas 1994	0.58
NODC World Ocean Atlas 1998	1.74
Reconstructed Reynolds SST	0.02
Reynolds Sea Surface Temperature	0.12
Northern Hem. EASE-Grid Weekly Snow Cover and Sea-Ice Extent	0.02
University of Delaware Precipitation and Air Temperature	0.58
TOTAL	**574.22**

ences, especially in academia, and because its files are self-describing and machine-independent. Beyond that, however, CDC has cooperated with data managers at the Pacific Marine Environmental Laboratory (PMEL) and the National Climatic Data Center (NCDC) to further refine netCDF for use with gridded climate data sets. The result has been the Cooperative Ocean-Atmosphere Research Data Standard (COARDS) convention that defines a metadata format, including required variables, variable attributes, and a data packing algorithm.

Use of the COARDS netCDF convention has allowed CDC and cooperating institutions to develop data sets and data access routines that are more easily exchanged. For example, CDC data management has developed COARDS-compliant access routines for GrADS and IDL, while PMEL has developed similar routines for MATLAB and their FERRET software package. In the past four years, the COARDS convention has become the de-facto standard for gridded climate data sets wherever netCDF is in common use. To comply with national policy directives, CDC also provides metadata for all of its data sets in the required FGDC format.

As can be seen elsewhere in this volume, CDC has made a major commitment to make climate information and products available through the Web. The public portions of our on-line archive can be searched, previewed, and downloaded via a locally developed web-based search interface or through cooperative initiatives, such as ESDIM's NOAAServer, NESDIS' National Virtual Data System (NVDS), URI/UCAR's Distributed Oceanograhpic Data System (DODS), and PMEL's Live Access Server (LAS). In several cases, CDC provides the largest on-line data archive accessible through these services. CDC is also currently cooperating in the development and installation of a next-generation data service, called the GrADS-DODS server (GDS). The GDS will form the core of the new NOAA Operational Model Archive and Distribution System (NOMADS) that will provide enhanced access to climate model output to researchers. CDC is scheduled to come online as a NOMADS node later this year.

Total usage of these services is tracked to anticipate adequate allocation of resources to pace user demand (**Fig. 7.6**). Data set transfers into and out of CDC using anonymous-FTP (the default for Web downloads) are now in the range of 1000 GB per month, 25 times the rate of four years ago. The NCEP Reanalysis data set has been particularly popular. Since its inception in 1995, CDC's

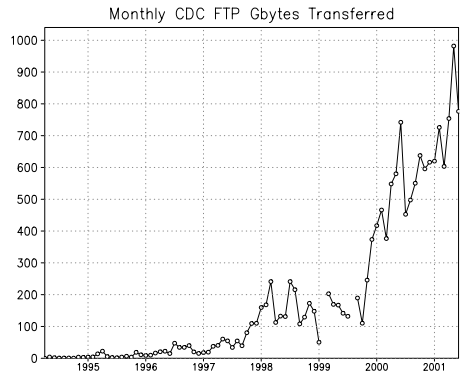

Fig. 7.6. Total gigabytes per month of files transferred using FTP at CDC.

NCEP Reanalysis web pages have received 2,157,250 "hits", leading to 257,838 downloads that have totaled 11.1 Terabytes. In addition, a total of 360 8-mm and DLT tape orders, often involving multiple tapes, have been filled which total an additional 14.9 Terabytes. Only CDC's netCDF version of NCEP Reanalysis is provided to external users. The original GRIB-format version of the Reanalysis can be acquired from NCDC or NCAR. The figures quoted above do not include CDC's own internal usage of the Reanalysis data set, which is considerable.

7.5 Ensuring long-term observed climate records

CDC pioneered the development of the Comprehensive Ocean-Atmosphere Data Set (COADS)—an international resource for historical weather observations over the globe. The ability to detect any future changes in regional, hemispheric, and global climate, and to make improvements in global climate models, depends crucially on the availability of high-quality retrospective data and metadata. As such, COADS forms the central oceanic ingredient for past and present National Scientific Assessments and for the Intergovernmental Panel on Climate Change, as well as for Global Atmospheric Reanalyses by US groups and by the European Centre for Medium-Range Weather Forecasts.

In 1985, the cooperating organizations issued the first version (Release 1) of this comprehensive historical record of marine meteorological data—observations from ships now extending back for over two centuries, supplemented since the late 19th century by data from oceanographic research vessels, and in recent decades from moored and drifting environmental buoys—and made them widely available and readily accessible to users. Both observational and gridded monthly summary products, which offer an unparalleled level of archival and statistical detail, were offered to the research community. These products have been periodically updated and enhanced, with the period of record now covering 1784–1997. To date, the data have been the basis for more than 500 published papers (up to 60 a month in American Meteorological Society Journals for recent years).

In 2001, a major milestone for COADS was the release of higher quality data and products that extend from 1997 back to 1784. Our most recent efforts concentrated on the period prior to 1950, requiring exceptional efforts in data archaeology to locate and digitize millions of historical ship records from US and international archives that were never previously available in digital form. This also required extensive cooperation with a host of international partners, including China, Germany, India, Japan, the Netherlands, Russia, and the United Kingdom. Major input data sources for the pre-1950 period are detailed in **Table 7.4**.

Final observational and statistical products based on these and other data were completed in early 2001, comprising COADS Release 1c (1784–1949). Similar updates to more contemporary periods, Releases 1b (1950–1979) and 1a

Table 7.4: New Pre-1950 Data Sources for COADS

NAME	YEARS	# of OBS
Blend of UK Main Marine Data Bank (MDB) and COADS	1854–1949	12.1M
Maury Collection	1784–1863	1.3 M
Norwegian Logbook Collection	1867–1889	0.2 M
Japanese Kobe Collection	1890–1932	1.0 M
US Merchant Marine Collection	1912–1946	3.5 M
Russian Makarov Collection	1804–1891	3.5 K
World Ocean Database	1998	405 K
Arctic drift shifts and stations	various	16 K
Russian MARMET data (previously known as MORMET)	various	268 K

(1980–1997), were finished during 1996–1997. Thus upon completion of Release 1c, the original Release 1 (1854–1979) data were fully replaced by a consistent set of data and metadata products covering the extended period 1784–1997, with many additions of new and improved data. Web-based capabilities are now under development for subsetting in space and time of the basic 1784–1997 observations and statistics into easily used ASCII formats. When these new capabilities are finalized, COADS Release 2 will be considered complete.

Increases in the number of observations for the pre-1950 period due to new data are illustrated in **Fig. 7.7**. The two panels show the number of observations prior to 1950 previously available in COADS Release 1, plus the new observations recently added. The major contribution of the Maury Collection (left panel) towards extending the start of COADS prior to 1854 is clearly evident. It should be noted, however, that instrumental data are sparse prior to 1854 and most of these observations are wind estimates from sailing ships. Similarly, the right panel shows the importance of additions from the UK MDB, Kobe and US Merchant Marine Collections in the first half of the 20th century.

The increase in SLP observations between Release 1 and Release 1c is dramatic especially in the 19th century (**Fig. 7.8**). Much of the Release 1 data prior to about 1880 were from a “Dutch” source (possibly of international origin), in

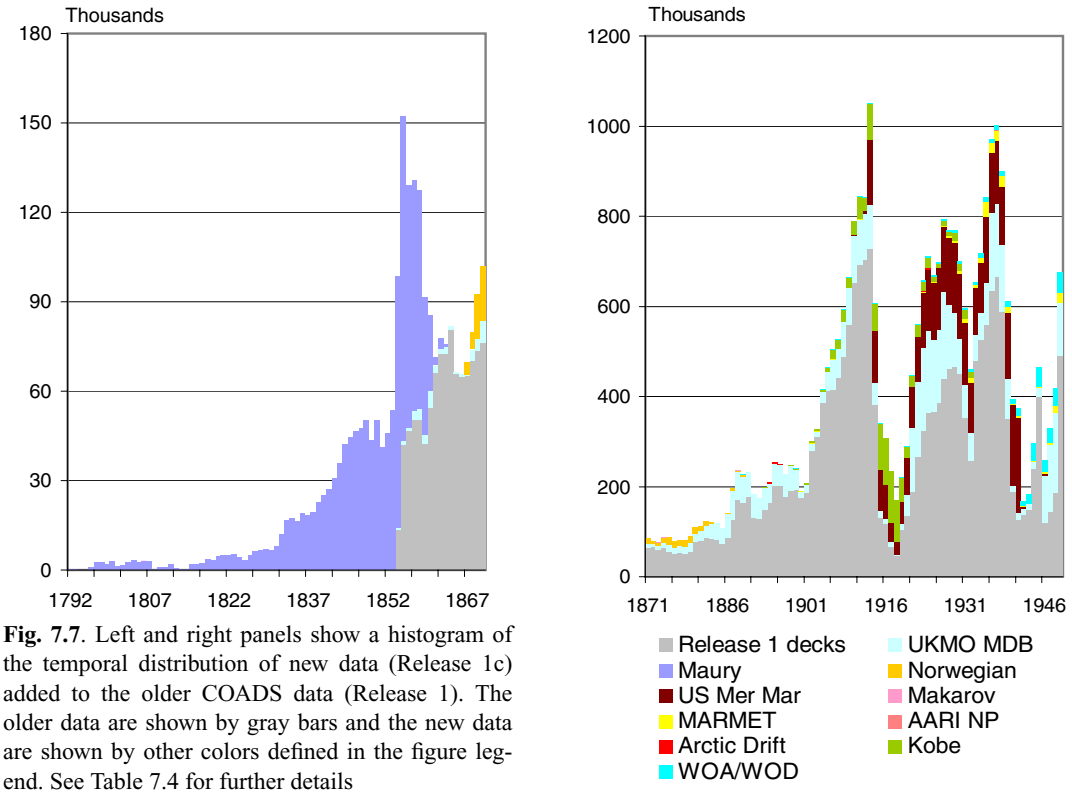

Fig. 7.7. Left and right panels show a histogram of the temporal distribution of new data (Release 1c) added to the older COADS data (Release 1). The older data are shown by gray bars and the new data are shown by other colors defined in the figure legend. See Table 7.4 for further details

which pressure was available among supplemental data but not adjusted for gravity. These SLP observations have been adjusted for gravity and made available for the first time in Release 1c. We believe that these and other important increases in the numbers of historic observations have significantly improved COADS coverage, providing a good basis for future planned improvements.

A "Workshop on Advances in the Use of Historical Marine Climate Data" will be hosted by CDC 18–21 September 2001 in Boulder, Colorado, USA. The workshop, organized by NOAA, the UK Met Office and the Japan Meteorological Agency, and sponsored by the Global Climate Observing System (GCOS) and WMO, will build on the blend of the US Comprehensive Ocean-Atmosphere Data Set (COADS), with the UK Met Office MDB, plus with newly digitized data in the US and from other international partners. The blended product, encompassing 1784–1997, will provide the climate research community with an unprecedented assembly of *in situ* marine data.

Contributed by: *J. Collins, C. Harrop, D. Hooper, S. Lubker, A. McColl, C. McColl, B. McInnes, D. Mock, R. Schweitzer, and S. Woodruff.*

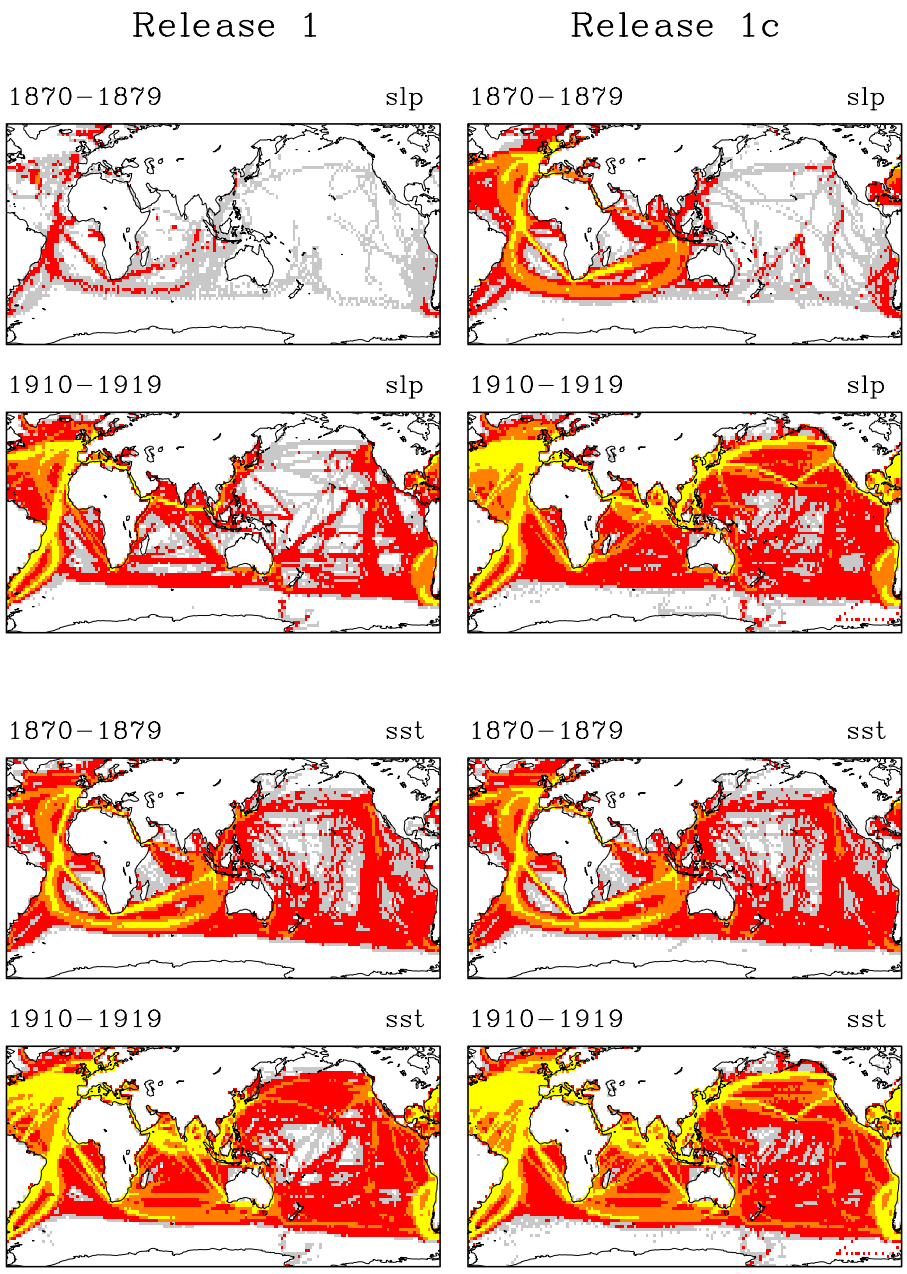

Fig. 7.8. Mapped comparison of decadal totals of SLP and SST observations (70°N–78°S; 68°W–68°W) for two decades (1870–1879 and 1910–1919) in COADS Release 1 and 1c. Older data available in COADS Release 1 are shown in the left column; existing plus new data added for Release 1c are shown on the right column. The colors correspond to the number of observations in each 2° box per decade: blue indicates 10–99, yellow indicates 100–399, orange indicates 400 or more.

CHAPTER 8

CDC Publications 1997–2001

Ackerman, S. A., and **R. Pincus**, 2001: Radiation in the atmosphere: Observations and applications. In *The McGraw-Hill Handbook of Meteorology*, T. D. Potter and B. Colman (Eds.), McGraw-Hill, New York, in press.

Alexander, M. A., **M. S. Timlin**, and **J. D. Scott**, 2001: Winter-to-Winter recurrence of sea surface temperature, salinity and mixed layer depth anomalies. *Prog. Oceanog.*, in press.

Alexander, M. A., and **J. K. Eischeid**, 2001: Climate variability in regions of amphibian declines. *Conservation Biology*, in press.

Alexander, M. A., **J. D. Scott**, and C. Deser, 2000: Processes that influence sea surface temperature and ocean mixed layer depth variability in a coupled model. *J. Geophys. Res.*, **105** , 16823–16842.

Alexander, M. A., C. Deser, and **M. S. Timlin**, 1999: The re-emergence of SST anomalies in the North Pacific Ocean. *J. Climate*, **12**, 2419–2431.

Alexander, M. A., and **J. D. Scott**, 1997: Surface flux variability over the North Pacific and North Atlantic Oceans. *J. Climate*, **10**, 2963–2978.

Alley, R.B., P. U. Clark, L. D. Keigwin, and **R. S. Webb**, 1999. Making sense of millennial-scale climate change. In *Mechanisms of Millennial-Scale Global Climate Change*, P. U. Clark, R. S. Webb, and L. D. Keigwin (Eds.), American Geophysical Union, Washington, 385-394.

Barros, V., M. Gonzalez, **B. Liebmann**, and I. Camilloni, 2000: Influence of the South Atlantic convergence zone and South Atlantic sea surface temperature on interannual summer rainfall variability in southeastern South America. *Theor. Appl. Climatol.*, **67**, 123–133.

Barsugli, J. J., **J. S. Whitaker**, **A. F. Loughe**, **P. D. Sardeshmukh,** and Z. Toth, 1999: Effect of the 1997–98 El Niño on individual large-scale weather events. *Bull. Amer. Met*. Soc., **80**, 1399–1411.

Barsugli, J. J., and D. S. Battisti, 1998: The basic effects of atmosphere-ocean thermal coupling on midlatitude variability. *J. Atmos. Sci*., **55**, 477–493.

Bates, G. T., **M. P. Hoerling**, and A. Kumar, 2001: Central U. S. springtime precipitation extremes: Teleconnections and relationships with sea surface temperatures. *J. Climate*, in press.

Bates, J. J., and **D. L. Jackson**, 1997: A comparison of water vapor observations with AMIP-I simulations. *J. Geophys. Res*., **102**, 21, 837–852.

Beniston, M., **H. F. Diaz**, and R. S. Bradley, 1997: Climatic change at high elevation sites: An overview. *Climate Change*, **36**, 233–251.

Berg, W. K., **J. J. Bates**, and **D. L. Jackson**, 1999: Analysis of upper tropospheric water vapor using SSM/T2, HIRS-12, and GMS VISSR data. *J. Appl. Met.*, **38**, 580–595.

Berg, W., W. Olson, R. R. Ferraro, S. J. Goodman, and F. J. LaFontaine, 1998: An assessment of the first- and second-generation Navy operational precipitation retrieval algorithms. *J. Atmos. Sci.*, **55**, 1558–1575.

Bergman, J. W., **H. H. Hendon**, and **K. M.**

Weickmann, 2001: Intraseasonal air-sea interaction and the onset of ENSO. *J. Climate*, **14**, 1702–1719.

Bergman, J. W., and **H. H. Hendon**, 2000: Cloud radiative forcing of the low latitude tropospheric circulation: linear calculation. *J. Atmos. Sci.*, **57**, 2225–2245.

Bergman, J. W., and **H. H. Hendon**, 2000: The impact of clouds on the seasonal cycle of radiative heating over the Pacific. *J. Atmos. Sci.*, **57**, 545–566.

Bergman, J. W., and **H. H. Hendon**, 1998: Calculating radiative fluxes and heating rates from monthly observations of cloud cover. *J. Atmos. Sci.*, **55**, 3471–3491.

Bergman, J. W., and M. L. Salby, 1997: The role of cloud diurnal variations in the time-mean energy budget. *J. Climate,* **10**, 1114–1124.

Bergman, J. W., 1997: A numerical investigation of cloud diurnal variations. *J. Climate*, **10**, 2330–2350.

Bhatt, U. S., **M. A. Alexander**, D. S. Battisti, D. D. Houghton, and L. M. Keller, 1998: Atmosphere-ocean interaction in the North Atlantic: near-surface climate variability. *J. Climate*, **11**, 1615–1632.

Black, R. X., and **R. M. Dole**, 2000: Storm tracks and barotropic deformation in climate models. *J. Climate*, **13**, 2712–2728.

Borges, M. D., and **P. D. Sardeshmukh**, 1997: Application of perturbation theory to the stability analysis of realistic atmospheric flows. *Tellus*, **49A**, 321–336.

Breon, F.-M., **D. L. Jackson**, and **J. J. Bates**, 1999: Evidence of atmospheric contamination on the measurement of the spectral response of GMS-5 water vapor channel. *J. Atmos. Oceanic Technol.,* **16**, 1851–1853.

Bush, M. B., M. Stute, M. P. Ledru, H. Behling, P. A. Colinvaux, P. E. De Oliveira, E. C. Grimm, H. Hooghiemstra, H. S. Haberle, B. W. Leyden, M.-L. Salgado-Labouriau, **R. S. Webb**, 2001: Paleotemperature estimates of the lowland Americas between 30°S and 30°N at the last glacial maximum. In *Interhemispheric Climate Linkages*, V. Markgraf (Ed.), Academic Press, New York, 293–306.

Capotondi, A., and **M. A. Alexander**, 2001: Rossby waves in the tropical North Pacific and their role in decadal thermocline variability. *J. Phys. Oceanogr.*, in press.

Cayan, D. R., M. D. Dettinger, **H. F. Diaz**, and N. E. Graham, 1998: Decadal variability of precipitation over western North America. *J. Climate,* **11**, 3148–3166.

Chang, P., **C. Penland**, L. Ji, H. Li, and **L. Matrosova**, 1998: Prediction of tropical Atlantic sea surface temperature. *Geo. Res. Lett.*, **23**, 2089–2092.

Changnon, S. A., R. Pielke, Jr., D. Changnon, R. T. Sylves, and **R. Pulwarty**, 2000: Human factors explain the increased losses from weather and climate extremes. *Bull. Amer. Met. Soc.,* **81**, 437–442.

Charles, C. D., D. Rind, R. Healy, and **R. S. Webb**, 2001: Tropical cooling and the isotopic composition of precipitation in general circulation model simulations of the ice age climate. *Climate Dynamics*, **17**, 489–502.

Chen, P., **M. P. Hoerling**, and **R. M. Dole**, 2001: The origin of the subtropical anticyclones. *J. Atmos. Sci.*, **58**, 1827–1835.

Chen, P., 2001: Thermally forced stationary waves in a quasigeostrophic system. *J. Atmos. Sci*., **58**, 1585–1594.

Chen, P., and **M. Newman**, 1998: Rossby-wave propagation and the rapid development of upper-level anomalous anticyclones during the 1988 U.S. drought. *J. Climate*, **11**, 2491–2504.

Chou, C.-B., and **H.-P. Huang**, 2000: Application of AVHRR data to a one-dimensional variational retrieval scheme for cloudy

TOVS data. *Mon. Wea. Rev.*, **128**, 3867–3878.

Clark, P. U., **R. S. Webb**, and L. D. Keigwin (Eds.), 1999: *Mechanisms of Millennial-Scale Global Climate Change*, American Geophysical Union, Washington, 394 pp.

Comfort, L., B. Wisner, **R. Pulwarty**, S. Cutter, K. Hewitt, A. Oliver-Smith, W. Peacock, J. Wiener, M. Fordham, and F. Krimgold, 1999: Reframing disaster policy: The global evolution of vulnerable communities. *Env. Hazards,* **1**, 39–44.

Compo, G. P., **P. D. Sardeshmukh**, and **C. Penland**, 2001: Changes of subseasonal variability associated with El Niño. *J. Climate*, **14**, 3356–3374.

Compo, G. P., G. N. Kiladis, and P. J. Webster, 1999: Horizontal and vertical structure of East Asian pressure surges. *Quart. J. Roy. Met. Soc*., **125**, 29–54.

Deser C., J. E. Walsh, and **M. S. Timlin**, 2000: Arctic sea ice variability in the context of recent atmospheric circulation trends. *J. Climate*, **13**, 617–633.

Deser, C., **M. A. Alexander**, and **M. S. Timlin**, 1999: Evidence for a wind-driven intensification of the Kuroshio Current Extension from the 1970s to the 1980s. *J. Climate*, **12**, 1697–1706.

Deser, C., and **C. A. Smith**, 1997: Diurnal and semidiurnal wind variations over the tropical Pacific Ocean. *J. Climate*, **10**, 1730–1748.

Deser, C., and **M. S. Timlin**, 1997: Atmosphere-ocean interaction on weekly timescales in the North Atlantic and Pacific. *J. Climate*, **10**, 393–408.

Dettinger, M. D. and **H. F. Diaz**, 2000: Global characteristics of streamflow seasonality and variability. *J. Hydromet.*, **1**, 289–310.

Dettinger, M. D., D. R. Cayan, **H. F. Diaz**, and D. M. Meko, 1998: North-south precipitation patterns in western North America on inter-annual-to-decadal time-scales. *J. Climate*, **11**, 3095–3111.

Diaz, H. F., **M. P. Hoerling**, and **J. K. Eischeid**, 2001: ENSO variability, teleconnections, and climate change. *Int. J. Climatol.,* in press.

Diaz, H. F., R. S. Kovats, A. J. McMichael, and N. Nicholls, 2001: Climate and human health linkages on multiple timescales. In *History and Climate: Memories of the Future?,* P. D. Jones, T. D. Davies, A. E. J. Ogilvie, and K. R. Briffa (Eds.), Kluwer Academic/Plenum, New York, 267–289.

Diaz H .F., and V. Markgraf (Eds.), 2000: *El Niño and the Southern Oscillation: Multi-scale Variability and Global and Regional Impacts,* Cambridge University Press, Cambridge, 496 pp.

Diaz, H. F., and G. J. McCabe, 1999: A possible connection between the 1878 yellow fever epidemic in the southern United States and the 1877–78 El Niño episode. *Bull. Amer. Met. Soc*., **80**, 21–27.

Diaz, H. F., and R. S. Bradley, 1997: Temperature variations during the last century at high elevation sites. *Climate Change*, **36**, 253–279.

Diaz, H. F., and **R. S. Pulwarty** (Eds.), 1997: *Hurricanes: Climate and Socioeconomic Impacts,* Springer-Verlag, Heidelberg, 292 pp.

Diaz, H. F., M. Beniston, and R. S. Bradley (Eds.), 1997: *Climatic Change at High Elevation Sites*, Kluwer Academic, Dordrecht, 298 pp.

Dole, R. M., 2001: Predicting climate variations in the Interior West: What are our prospects? In *Managing Western Water Resources in an Uncertain Climate*, W. Lewis (Ed.), Univer-

sity of Colorado Press, Boulder, in press.

Dole, R. M., 1999: Prospects for drought forecasts in the United States. In *Drought: A Global Assessment,* D. A. White (Ed.), Routledge, London, pp. 83–89.

Easterling, D. R., **H. F. Diaz**, A. V. Douglas, W. D. Hogg, K. E. Kunkel, J. C. Rogers, and J. F. Wilkinson, 1999: Long-term observations for monitoring extremes in the Americas. *Climate Change*, **42**, 285–308.

Eischeid, J. K., P. Pasteris, **H. F. Diaz**, M. Plantico, and N. Lott, 2000: Creating a serially complete, national daily time series of temperature and precipitation for the Western United States. *J. Appl. Meteorol.,* **39**, 1580–1591.

Epstein, P. R., **H. F. Diaz**, S. Elias, G. Grabherr, N. E. Graham, W. J. M. Martens, E. Mosley-Thompson, and J. Susskind, 1998: Biological and physical signs of climate change: Focus on mosquito-borne diseases. *Bull. Amer. Met. Soc*., **79**, 409–417.

Farrington, A. J., **S. Lubker**, U. Radok, and **S. Woodruff**, 1998: South Atlantic winds and weather during and following the Little Ice Age—A pilot study of English East India Company (EEIC) ship logs. *Meteorol. Atmos. Phy.*, **67**, 253–257.

Fasullo, J., and **D.-Z. Sun**, 2001: Radiative sensitivities to tropical water vapor under all-sky conditions. *J. Climate*, **14**, 2798–2807.

Ferraro, R. R., E. A. Smith, **W. Berg**, and G. J. Huffman, 1998: A screening methodology for passive microwave precipitation retrieval algorithms. *J. Atmos. Sci.*, **55**, 1583–1600.

Forman, S. L., R. Oglesby, **R. S. Webb**, 2001: Temporal and spatial patterns of Holocene dune activity on the Great Plains of North America: megadroughts and climate links. *Global and Planetary Change*, **29**, 1–29.

Fu, C., **H. F. Diaz**, D. Dong, and J. O. Fletcher, 1999: Changes in atmospheric circulation over the Northern Hemisphere oceans associated with the rapid warming of the 1920s. *Int. J. Climatol.*, **19**, 581–606.

Garcia, R. R., **H. F. Diaz**, R. G. Herrera, J. Eischeid, M. R. Prieto, E. Hernandez, L. Gimeno, F. R. Duran, and A. M. Bascary, 2001: Atmospheric circulation changes in the tropical Pacific inferred from the voyages of the Manila Galleon in the 16^{th}–18^{th} centuries. *Bull. Amer. Met. Soc.*, in press.

Graham, N. E. and **H. F. Diaz**, 2001: Evidence for intensification of North Pacific winter cyclones since 1948. *Bull. Amer. Met. Soc.,* in press.

Hall, N. M. J. and **P. D.Sardeshmukh**, 1998: Is the time-mean Northern Hemisphere flow baroclinically unstable? *J. Atmos. Sci.*, **55**, 41–56.

Hamill, T. M., and C. Snyder, 2001: Using improved background error covariances from an ensemble Kalman filter for adaptive observations. *Mon. Wea. Rev.*, in press.

Hamill, T. M., **J. S. Whitaker**, and C. Snyder, 2001: Distance-dependent filtering of background error covariance estimates in an ensemble Kalman filter. *Mon. Wea. Rev.*, in press.

Hamill, T. M., 2001: Interpretation of rank histograms for verifying ensemble forecasts. *Mon. Wea. Rev.*, **129**, 550–560.

Hamill, T. M., C. Snyder, D. P. Baumhefner, Z. Toth, and S. L. Mullen, 2000: Ensemble forecasting in the short to medium range: Report from a workshop. *Bull. Amer. Met. Soc.*, **81**, 2653–2664.

Hendon, H. H., 2000: Impact of air-sea coupling on the MJO in a GCM. *J. Atmos. Sci*., **57**, 3939–3952.

Hendon, H. H., **B. Liebmann**, **M. E. Newman**, **J. D. Glick**, and J. E. Schemm, 2000: Medium range forecast errors associated

with active episodes of the Madden-Julian oscillation. *Mon. Wea. Rev.*, **128**, 69–86.

Hendon, H. H., C. Zhang, and **J. D. Glick**, 1999: Interannual variation of the Madden-Julian oscillation during austral summer. *J. Climate*, **12**, 2538–2550.

Hendon, H. H., **B. Liebmann**, and **J. D. Glick**, 1998: Oceanic Kelvin waves and the Madden-Julian oscillation. *J. Atmos. Sci.*, **55**, 88–101.

Hendon, H. H., and **J. Glick**, 1997: Intraseasonal air-sea interaction in the tropical Indian and western Pacific Oceans. *J. Climate*, **10**, 647–661.

Hoerling, M. P., J. Hurrell, and **T. Xu**, 2001: Tropical origins for North Atlantic climate change. *Science*, **292**, 90–92.

Hoerling, M. P., A. Kumar, and **T. Xu**, 2001: Robustness of the nonlinear climate response to ENSO's extreme phases. *J. Climate*, **14**, 1277–1293.

Hoerling, M. P., **J. S. Whitaker**, A. Kumar, and W. Wang, 2001: The mid-latitude warming during 1998–2000. *Geo. Res. Lett.*, **28**, 755–758.

Hoerling, M. P., and A. Kumar, 2000: Understanding and predicting extratropical teleconnections related to ENSO. In *El Niño and the Southern Oscillation: Multi-scale Variations and Global and Regional Impacts*,. H.F. Diaz and V. Markgraf (Eds.), Cambridge University Press, Cambridge, 57–88.

Hoerling, M. P., and A. Kumar, 1997: Why do North American climate anomalies differ from one El Niño event to another? *Geophys. Res. Lett*, **24**, 1059–1062.

Hoerling, M. P., A. Kumar, and M. Zhong, 1997: El Niño, La Niña, and the nonlinearity of their teleconnections. *J. Climate*, **10**, 1769–1786.

Hoerling, M. P., and A. Kumar, 1997: Origins of extreme climate states during the 1982–83 ENSO winter. *J. Climate*, **10**, 2859–2870.

Huang, H.-P., B. Galperin, and S. Sukoriansky, 2001: Anisotropic spectra in two-dimensional turbulence on the surface of a rotating sphere. *Phys. Fluids* , **13**, 225–240.

Huang, H.-P., **K. M. Weickmann**, and C. J. Hsu, 2001: Trend in atmospheric angular momentum in a transient climate change simulation with greenhouse gas and aerosol forcing. *J. Climate*, **14**, 1525–1534.

Huang, H.-P., and **P. D. Sardeshmukh**, 2000: Another look at the annual and semiannual cycles of atmospheric angular momentum. *J. Climate*, **13**, 3221–3238.

Huang, H.-P., **P. D. Sardeshmukh**, and **K. M. Weickmann**, 1999: The balance of global angular momentum in a long-term atmospheric data set. *J. Geophys. Res*., **104**, 2031–2040.

Huang, H.-P., 1999: Scale-dependent properties of optimal perturbations on a zonally varying barotropic flow. *J. Atmos. Sci*., **56**, 1238–1247.

Huang, H.-P., and W. A. Robinson, 1998: Two-dimensional turbulence and persistent zonal jets in a global barotropic model. *J. Atmos. Sci*., **55**, 611–632.

Jackson, S., **R. S. Webb,** J. T. Overpeck, K. A. Anderson, T. Webb III, J. Williams, B. C. S. Hansen, 2000: Vegetation and environment in eastern North America during the last glacial maximum. *Quat. Sci. Rev.*, **19**, 489–508.

Jain, S., and U. Lall, 2001: Floods in a changing climate: Does the past represent the future? *Water Resour. Res.*, in press.

Jain, S., and U. Lall, 2000: Magnitude and timing of annual maximum floods: Trends and large-scale climatic associations for the

Blacksmith Fork River, Utah. *Water Resour. Res.*, **36**, 3641–3651.

Johnson, R. H., and **B. E. Mapes**, 2001: Mesoscale processes and severe convective weather. In *Severe Convective Weather,* AMS Monograph, American Meteorological Society, Boston, in press.

Kerwin, M., J. T. Overpeck, **R. S. Webb**, A. DeVernal, D. H. Rind, and R. J. Healy, 1999: The role of oceanic forcing in mid-Holocene Northern Hemisphere Climatic Change. *Paleoceanography*, **14**, 200-210.

Kiladis, G. N. and **K. M. Weickmann**, 1997: Horizontal structure and seasonality of large-scale circulations associated with submonthly tropical convection. *Mon. Wea. Rev.*, **125**, 1997–2013.

Kumar, A., A. G. Barnston, and **M. P. Hoerling**, 2001: Seasonal predictions, probabilistic verifications, and ensemble size. *J. Climate*, **14**, 1671–1676.

Kumar, A., W. Wang, **M. P. Hoerling**, A. Leetma, and M. Ji, 2001: The sustained North American warming of 1997 and 1998. *J. Climate*, **14**, 345–353.

Kumar, A., A. Barnston, P. Peng, **M. P. Hoerling**, and L. Goddard, 2000: Changes in the spread of the seasonal mean atmospheric states associated with ENSO *J. Climate*, **13**, 3139–3151.

Kumar, A., and **M. P. Hoerling**, 2000: Analysis of a conceptual model of seasonal climate variability and implications for seasonal prediction. *Bull. Amer. Met. Soc.*, **81**, 255–264.

Kumar, A., and **M. P. Hoerling**, 1998: On the specification of regional SSTs in AGCM simulations. *J. Geophy. Res*., **103**, 8901–8907.

Kumar, A., and **M. P. Hoerling**, 1998: Annual cycle of Pacific/North American seasonal predictability associated with different phases of ENSO. *J. Climate*, **11**, 3295–3308.

Kumar, A., and **M. P. Hoerling**, 1997: Interpretation and implications of observed inter-El Niño variability. *J. Climate*, **10**, 83–91.

Liebmann, B., and J. A. Marengo, 2001: Interannual variability of the rainy season and rainfall in the Brazilian Amazon Basin. *J. Climate*, in press.

Liebmann, B., C. Jones, and L. M. V. de Carvalho, 2001: Interannual variability of daily extreme precipitation events in the State of São Paulo, Brazil. *J. Climate*, **14**, 208–218.

Liebmann, B., G. N. Kiladis, J. A. Marengo, T. Ambrizzi, and **J. D. Glick**, 1999: Submonthly convective variability over South America and the South Atlantic convergence zone. *J. Climate*, **12**, 1877–1891.

Liebmann, B., J. A. Marengo, **J. D. Glick**, V. E. Kousky, I. C. Wainer, and O. Massambani, 1998: A comparison of rainfall, outgoing longwave radiation, and divergence over the Amazon Basin. *J. Climate*, **11**, 2898–2909.

Liebmann, B., H. H. Hendon, and J. D. Glick, 1997: On the generation of two-day convective disturbances across the western equatorial Pacific. *J. Meteor. Soc. Japan*, **75**, 939–946.

Lo, F., and **H. H. Hendon**, 2000: Empirical prediction of the MJO. *Mon. Wea. Rev.*, **128**, 2528–2543.

Lucas, L. E., D. E. Waliser, P. P. Xie, J. E. Janowiak, and **B. Liebmann**, 2001: Estimating the satellite equatorial crossing time biases in the daily, global outgoing longwave radiation dataset. *J. Climate*, **14**, 2583–2605.

Mapes, B. E., 2001: Water's two height scales: the moist adiabat and the radiative troposphere. *Quart. J. Roy. Met. Soc*., in press.

Mapes, B. E., and X. Wu, 2001: Convective eddy momentum tendencies in long cloud-resolving model simulations. *J. Atmos. Sci.*, **58**, 517–526**.**

Mapes, B. E., 2000: Convective inhibition, subgridscale triggering, and stratiform instability in a toy tropical wave model. *J. Atmos. Sci.*, **57**, 1515–1535.

Mapes, B. E., 1998: The large-scale part of tropical mesoscale convective system circulations: a linear vertical spectral band model. *J. Meteor. Soc. Japan*, **76**, 29–55.

Mapes, B. E., 1997: Equilibrium vs. activation controls on large-scale variations of tropical deep convection. In *The Physics and Parameterization of Moist Convection*, R. K. Smith (Ed.), Kluwer Academic Publishers, Dordrecht, 321–358.

Mapes, B. E., 1997: Mutual adjustment of mass flux and stratification profiles. In *The Physics and Parameterization of Moist Convection*, R. K. Smith (Ed.), Kluwer Academic Publishers, Dordrecht, 399–412.

Marengo, J. A., **B. Liebmann**, V. E. Kousky, N. P. Filizola, and I. C. Wainer, 2001: Onset and end of the rainy season in the Brazilian Amazon Basin. *J. Climate*, **14**, 833–852.

Markgraf, V. and **H. F. Diaz**, 2000: The past ENSO record: A synthesis. In *El Niño and the Southern Oscillation*: *Multiscale Variability and Global and Regional Impacts*, H. F. Diaz and V. Markgraf (Eds.), Cambridge University Press, Cambridge, 465–488.

Markgraf, V., T. R. Baumgartner, J. P. Bradbury, **H. F. Diaz**, R. B. Dunbar, B. H. Luckman, G. O. Seltzer, R. W. Swetnam, and R. Villalba, 2000: Paleoclimate reconstruction along the Pole-Equator-Pole transect of the Americas (PEP 1). *Quat. Sci. Rev.*, **19**, 125–140.

Marshall, S., R. J. Oglesby, K. A. Maasch and **G. T. Bates**, 1999: Improving climate model representations of snow hydrology. *Environmental Modelling and Software*, **14**, 327–334.

Meehl, G. A., R. Lukas, G. Kiladis, **K. Weickmann**, A. Matthews, and M. Wheeler, 2001: A conceptual framework for time and space scale interactions in the climate system. *Clim. Dyn.*, in press.

Meehl, G.A., T. Karl, D. R. Easterling, S. Changnon, R. Pielke, Jr., D. Changnon, J. Evans, P. Y. Groisman, T. R. Knutson, K. E. Kunkel, L.O. Means, C. Parmesan, **R. Pulwarty**, T. Root, R. T. Sykes, P. Whetton, and F. Zwiers, 2000: An introduction to trends in extreme weather and climate events: observations, socioeconomic impacts, terrestrial ecological impacts, and model projections. *Bull. Amer. Met. Soc.,* **81**, 413–416.

Newby, P. E., P. Killoran, M. R. Waldorf, **R. S. Webb**, and T. Webb III, 2000: 11,500 years of sediment, vegetation and water level changes at the Makepeace Cedar Swamp, Southeastern Massachusetts. *Quat. Res.*, **53**, 352–368.

Newman, M. E., **M. A. Alexander**, **C. R. Winkler**, **J. D. Scott**, and **J. J. Barsugli** , 2000: A linear diagnosis of the coupled extratropical ocean-atmosphere system in the GFDL AGCM. *Atmos. Sci. Lett.*, **1**, 1–8.

Newman, M., **P. D. Sardeshmukh**, and **J. W. Bergman**, 2000: An assessment of the NCEP, NASA and ECMWF reanalyses over the tropical west Pacific warm pool. *Bull. Amer. Met. Soc.,* **81**, 41–48.

Newman, M., and **P. D. Sardeshmukh**, 1998: The impact of the annual cycle on the North Pacific/North American response to remote low frequency forcing. *J. Atmos. Sci.*, **55**, 1336–1353.

Newman, M., **P. D. Sardeshmukh**, and **C. Penland**, 1997: Stochastic forcing of the wintertime extratropical flow. *J. Atmos. Sci*., **54**, 435–455.

Overpeck, J. T., and **R. S. Webb**, 2000: Non-glacial rapid climate events: Past and future. *Proc. Nat. Acad. Sci. USA*, **97**, 1335–1338.

Peng, S., and W. A. Robinson, 2001: Relationships between atmospheric internal variability and the responses to an extratropical SST anomaly. *J. Climate*, **14**, 2943–2959.

Peng, S., and **J. S. Whitaker**, 1999: Mechanisms determining the atmospheric response to midlatitude SST anomalies. *J. Climate*, **12**, 1393–1408.

Peng, S., W. A. Robinson, and **M. P. Hoerling**, 1997: The modeled atmospheric response to midlatitude SST anomalies and its dependence on background circulation states. *J. Climate*, **10**, 971–987.

Penland, C., 2001: On the perception of probabilistic forecasts. In *Facts and Speculation about La Niña and its Societal Impacts*, M. H. Glantz (Ed.), United Nations University Press, Tokyo, in press.

Penland, C., and **L. Matrosova**, 2001: Expected and actual errors of linear inverse modeling forecasts. *Mon. Wea. Rev.*, **129**, 1740–1745.

Penland, C., M. Fluegel, and P. Chang, 2000: On the identification of dynamical regimes in an intermediate coupled ocean-atmosphere model. *J. Climate,* **13**, 2105–2115.

Penland, C., and **L. Matrosova**, 1998: Prediction of tropical Atlantic sea surface temperatures using linear inverse modeling. *J. Climate*, **11**, 483–496.

Pielke, R., J. Kimpel, C. Adams, J. Baker, S. Changnon, R. Keener, P. Leavitt, J. McCarthy, K. Miller, A. Murphy, **R. S. Pulwarty**, R. Roth, E. Stanley, T. Stewart, T. Zacharias, 1997: The U.S. Weather Research Program: Societal impacts. *Bull. Amer. Met. Soc.,* **79** , 867–876.

Pincus, R., and S. A. Ackerman, 2001: Radiation in the atmosphere: Fundamentals. In *The McGraw-Hill Handbook of Meteorology*, T. D. Potter and B. Colman (Eds.), McGraw-Hill, New York, in press.

Pulwarty, R. S., 1998: Hurricane impacts in the context of climate variability, climate change and coastal management policy on the eastern U.S. sea-board. In *Climate, Change and Risk.Downing*, T. A. Olsthoorn, and R. Tol (Eds.), Routledge, London, 173–204.

Pulwarty, R. S., R. Barry, C. Hurst, K. Sellinger, and L. Mogollon, 1998: Precipitation on the Venezuelan Andes in the context of regional climate. *Meteor. Atmos. Phys. ,* **16***,* 217-237.

Pulwarty, R. S., and K. Redmond, 1997: Climate and salmon restoration in the Columbia River basin: the role and usability of seasonal forecasts. *Bull. Amer. Met. Soc.*, **78***,* 381–397.

Pulwarty, R. S., and W. R. Riebsame, 1997: The political ecology of hurricane-related hazards. In *Hurricanes: Climate and Socio-economic impacts*, H. Diaz and R. Pulwarty (Eds.), Springer-Verlag, Heidelberg, 185–214.

Radok, U., **C. A. Smith** and G. Wendler 1998: Southern Ocean synoptics—observations and analyses. *Meteorol. Appl.*, **5**, 33–36.

Ribera, P., R. Garcia, **H. F. Diaz**, L. Gimeno, and E. Hernandez, 2000: Trends and interannual oscillations in the main sea-level surface pressure patterns over the Mediterranean, 1955–1990. *Geophys. Res. Lett.*, **27**, 1143–1146.

Ricciardulli, L., and R. R. Garcia, 2000: The excitation of equatorial waves by deep convection in the NCAR Community Climate Model (CCM3). *J. Atmos. Sci*., **57**, 3461–3487.

Rufenach, C., **J. Bates**, and S. Tosini, 1998: ERS-1 scatterometer measurements: Part 1, the relationship between radar cross section and buoy wind in two oceanic regions. *IEEE Trans. Geosci. Rem. Sens*., **36**, 603–622.

Sardeshmukh, P. D., **C. Penland**, and **M. Newman**, 2001: Rossby waves in a fluctuating medium. In *Stochastic Climate Models,* P. Imkeller and J.-S. von Storch (Eds.),

Progress in Probability, **49**, Birkhaueser, Basel, 369–384.

Sardeshmukh P. D., **G. P. Compo**, and **C. Penland**, 2000: Changes of probability associated with El Niño. *J. Climate*, **13**, 4268–4286.

Sardeshmukh, P. D., **M. Newman**, and **M. D. Borges**, 1997: Free barotropic Rossby wave dynamics of the wintertime low-frequency flow. *J. Atmos. Sci.,* **54**, 5–23.

Schneider, N., A. J. Miller, **M. A. Alexander**, C. Deser, 1999: Subduction of decadal north Pacific temperature anomalies: observations and dynamics. *J. Phys. Oceanogr.*, **29**, 1056–1070.

Scott, J. D., and **M. A. Alexander**, 1999: Net shortwave fluxes over the ocean. *J. Phys. Oceanogr.,* **29**, 3167–3174.

Scott, J. D., **M. A. Alexander**, **J. A. Collins**, and **C. A. Smith**, 1997: Interactive visualization of climate data on the WWW. *Bull. Amer. Met. Soc*., **78**, 1985–1989.

Serreze, M., M. Clark, R. Armstrong, D. McGinnis, and **R. Pulwarty**, 1999: Characteristics of western U.S. snowpack telemetry (SNOTEL) data. *Water Resour. Res.*, **35**, 2145–2160.

Shaw. J. A., **J. J. Bates**, H. M. Zorn, and J. H. Churnside, 1999: Observations of downwelling infrared radiance at Mauna Loa, Hawaii during the 1997–1998 ENSO event. *Geophys. Res. Lett*., **26**, 1727–1730.

Shinoda T., and **H. H. Hendon**, 2001: Upper ocean heat budget in response to the Madden-Julian Oscillation in the western equatorial Pacific. *J. Climate*, in press.

Shinoda, T., **H. H. Hendon**, and **J. D. Glick**, 1999: Intraseasonal surface fluxes in the tropical western Pacific from NCEP reanalyses. *Mon. Wea. Rev.*,**127**, 678–693.

Shinoda, T., **H. H. Hendon**, and **J. D. Glick**, 1998: Intraseasonal variability of surface fluxes and sea surface temperature in the tropical western Pacific and Indian Oceans. *J. Climate*, **7**, 1685–1702.

Shinoda, T., and **H. H. Hendon**, 1998: Mixed layer modeling of intraseasonal sea surface temperature variability in the tropical western Pacific and Indian Ocean. *J. Climate*, **11**, 2668–2685.

Smith, C. A., and **P. D. Sardeshmukh**, 2000: The effect of ENSO on the intraseasonal variance of surface temperature in winter. *Int. J. Climatol*., **20**, 1543–1557.

Soden, B., S. Tjemkes, J. Schmetz, R. Saunders, **J. Bates**, B. Ellingson, R. Engelen, L. Garand, **D. Jackson**, G. Jedlovec, T. Kleespies, D. Randel, P. Rayer, E. Salathe, D. Schwarzkopf, N. Scott, B. Sohn, S. de Souza-Machado, L. Strow, D. Tobin, D. Turner, P. van Delst, and T. Wehr, 2000: An intercomparison of radiation codes for retrieving upper tropospheric humidity in the 6.3-micron band: A report from the Firstt GVaP Workshop. *Bull. Amer. Met. Soc.,* **81**, 797–808.

Suarez, M. J., W. J. Emery, and **G. A. Wick**, 1997: The multi-channel infrared sea truth radiometric calibrator (MISTRC). *J. Atmos. Oceanic Technol*., **14**, 243–253.

Sun D.-Z., C. Covey, and R. S. Lindzen, 2001: Vertical correlations of water vapor in GCMs. *Geophys. Res. Lett.*, **28**, 259–262.

Sun, D. Z., 2000: The heat sources and sinks of the 1986-87 El Niño. *J. Climate*, **13**, 3533–3550.

Sun, D. Z., 2000: Global climate change and El Niño: A theoretical framework. In *El Niño and the Southern Oscillation: Multiscale Variability and Global and Regional Impacts*, H. F. Diaz and V. Markgraf (Eds.), Cambridge University Press, Cambridge,

443–463.

Sun, D. Z., and K. E. Trenberth, 1998: Coordinated heat removal from the equatorial Pacific during the 1986-87 El Niño. *Geophys. Res. Lett.* , **25**, 2659–2662.

Sun, D. Z., 1997: El Niño: A coupled response to radiative heating? *Geophys. Res. Lett*., **24**, 2031–2034.

Ting, M., **M. P. Hoerling**, **T. Xu**, and A. Kumar, 2000: Reply to Comments on "Northern Hemisphere teleconnections patterns during extreme phases of the zonal-mean circulation". *J. Climate*, **13**, 1040–1043.

Torrence, C., and **G. P. Compo**, 1998: A practical guide to wavelet analysis. *Bull. Amer. Met. Soc*., **79**, 61–78.

Weickmann, K. M., W. A. Robinson, and **C. Penland**, 2000: Stochastic and oscillatory forcing of global atmospheric angular momentum. *J. Geophys. Res.*, **105**, 15543–15557.

Weickmann, K. M., G. N. Kiladis and **P. D. Sardeshmukh**, 1997: The dynamics of intraseasonal atmospheric angular momentum oscillations. *J. Atmos. Sci.*, **54**, 1445–1461.

Wheeler, M., and **K. M. Weickmann**, 2001: Real time monitoring of modes of coherent synoptic to intraseasonal convective variability. *Mon. Wea. Rev.*, in press.

Whitaker, J. S., and **K. M. Weickmann**, 2001: Subseasonal variations of tropical convection and week two prediction of wintertime western North American rainfall. *J. Climate*, **14**, 3279–3288 .

Whitaker, J. S., and **A. F. Loughe**, 1998: The relationship between ensemble spread and ensemble mean skill. *Mon. Wea. Rev.* **126**, 3292–3302.

Whitaker, J. S., and **P. D. Sardeshmukh**, 1998: A linear theory of extratropical synoptic eddy statistics. *J. Atmos. Sci*., **55**, 237–258.

Wick, G. A., and A. T. Jessup, 1998: Simulation of ocean skin temperature modulation by swell waves. *J. Geophys. Res*., **103**, 3149–3161.

Winkler C. R., **M. Newman**, and **P. D. Sardeshmukh**, 2001: A linear model of wintertime low-frequency variability. Part I: Formulation and forecast skill. *J. Climate*, in press.

Wolter, K., **R. M. Dole** and **C. A. Smith**, 1999: Short-term climate extremes over the continental U.S. and ENSO, Part I: Seasonal temperatures. *J. Climate*, **12**, 3255–3272.

Wolter, K., and **M. S. Timlin**, 1998: Measuring the strength of ENSO events: How does 1997/98 rank? *Weather*, **53**, 315–324.

Wolter, K., 1997: Trimming problems and remedies in COADS. *J. Climate*, **10**, 1980–1997.

Woodruff, S. D., **H. F. Diaz**, J. D. Elms, and S. J. Worley, 1998: COADS Release 2 data and metadata enhancements for improvements of marine surface flux fields. *Phys. Chem. Earth*, **23**, 517–526.

Yano, J.-I., W. W. Grabowski, G. L. Roff, and **B.E. Mapes**, 2000: Asymptotic approaches to convective quasi-equilibrium, *Quart. J. Roy. Met. Soc*., **126**, 1–27.

Zhang, C., and **Hendon, H. H.**, 1997: On the propagating and standing components of the intraseasonal oscillation in tropical convection. *J. Atmos. Sci*., **54**, 741–752.

CHAPTER 9

CDC Organization and Personnel

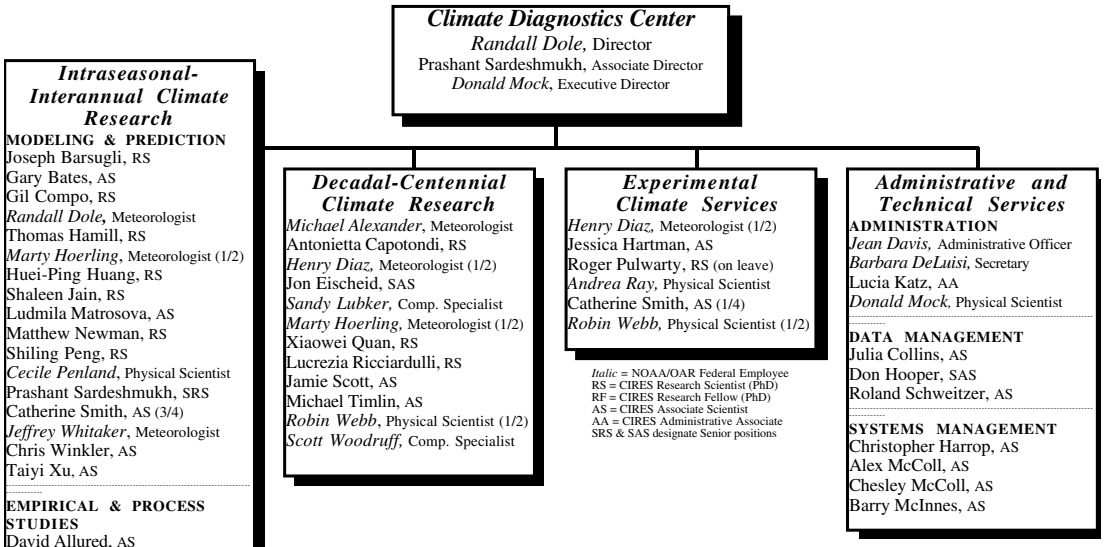

Advancing Understanding and Predictions of Climate Variability

CDC conducts fundamental research to identify the nature and causes of climate variations on time scales ranging from weeks to centuries. The goal of this work is to develop the ability to predict important climate variations on these time scales.

Climate Diagnostics Center Personnel

NAME	EMAIL	PHONE	ROOM	TITLE
Michael Alexander	maa@cdc.noaa.gov	497-6030	1D121	Physical Scientist
Dave Allured	dallured@cdc.noaa.gov	497-6825	1D505	Research Associate
Joseph Barsugli	jjb@cdc.noaa.gov	497-6042	1D502	Research Scientist
Gary Bates	gtb@cdc.noaa.gov	497-6058	1D133	Associate Scientist
John Bergman	jwb@cdc.noaa.gov	497-6076	1D513	Research Scientist
Antonietta Capotondi	mac@cdc.noaa.gov	497-6105	1D106	Research Scientist
Julia Collins	jac@cdc.noaa.gov	497-6113	1D113	Associate Scientist

NAME	EMAIL	PHONE	ROOM	TITLE
Gil Compo	gpc@cdc.noaa.gov	497-6115	1D501	Research Scientist
Jean Davis*	jyd@cdc.noaa.gov	497-7690	1D117	Administrative Officer
Barbara DeLuisi*	barb@cdc.noaa.gov	497-4233	1D118	Secretary
Henry Diaz	hfd@cdc.noaa.gov	497-6649	1D122A	Meteorologist
Randall Dole*	rmd@cdc.noaa.gov	497-5812	1D116	Director
Jon Eischeid	jon@cdc.noaa.gov	497-5970	1D132	Sr. Associate Scientist
Thomas Hamill	hamill@cdc.noaa.gov	497-3060	1D507	Research Scientist
Christopher Harrop	harrop@cdc.noaa.gov	497-6808	1D113	Associate Scientist
Jessica Hartman	jhartman@cdc.noaa.gov	497-5276	1D136	Associate Scientist
Martin Hoerling	mph@cdc.noaa.gov	497-6165	1D127	Physical Scientist
Don Hooper	hoop@cdc.noaa.gov	497-6168	1D609	Sr. Associate Scientist
Huei-Ping Huang	hp@cdc.noaa.gov	497-6175	1D405	Research Associate
Shaleen Jain	sjain@cdc.noaa.gov	497-6295	1D511	Research Scientist
Lucia Katz*	lucia@cdc.noaa.gov	497-6188	1D118	Admin Associate
Shuanglin Li	lshl@cdc.noaa.gov	497-3877	1D131	Associate Scientist
Brant Liebmann	bl@cdc.noaa.gov	497-6190	1D137	Research Scientist
Sandra Lubker	sjl@cdc.noaa.gov	497-6641	1D509	Computer Specialist
Brian Mapes	bem@cdc.noaa.gov	497-6213	1D105	Research Scientist
Ludmila Matrosova	lem@cdc.noaa.gov	497-6130	1D119	Associate Scientist
David McBreen	mcbreen@cdc.noaa.gov	497-6551	1D504	Student
Alex McColl	ham@cdc.noaa.gov	497-6218	1D126	Associate Scientist
Chesley McColl	ckm@cdc.noaa.gov	497-6222	1D503	Associate Scientist
Barry McInnes	bjm@cdc.noaa.gov	497-6231	1D404	Associate Scientist
Don Mock*	drm@cdc.noaa.gov	497-6643	1D114	Executive Director
Matt Newman	matt@cdc.noaa.gov	497-6233	1D604	Research Scientist
Shiling Peng	sp@cdc.noaa.gov	497-6644	1D122B	Research Scientist
Cecile Penland	mcp@cdc.noaa.gov	497-6234	1D109	Research Scientist
Robert Pincus	robert@cdc.noaa.gov	497-6310	1D123	Research Scientist

NAME	EMAIL	PHONE	ROOM	TITLE
Roger Pulwarty	rsp@cdc.noaa.gov	497-6236	leave	Research Scientist
David Pyles	dqpyles@cdc.noaa.gov	497-6236	1D111	Research Scientist
Xiaowei Quan	qxw@cdc.noaa.gov	497-6807	1D506	Research Scientist
Andrea Ray	ajr@cdc.noaa.gov	497-6434	1D512	Physical Scientist
Lucrezia Ricciardulli	lr@cdc.noaa.gov	497-6214	1D119	Research Scientist
Andres Roubicek	aro@cdc.noaa.gov	497-6096	1D104	Associate Scientist
Prashant Sardeshmukh*	pds@cdc.noaa.gov	497-6248	1D112	Sr. Research Scientist
Roland Schweitzer	rhs@cdc.noaa.gov	497-6249	off site	Associate Scientist
Jamie Scott	jds@cdc.noaa.gov	497-6257	1D602	Associate Scientist
Toshiaki Shinoda	ts@cdc.noaa.gov	497-6262	1D508	Research Scientist
Catherine Smith	cas@cdc.noaa.gov	497-6263	1D106	Associate Scientist
Dezheng Sun	ds@cdc.noaa.gov	497-6272	1D108	Research Scientist
Michael Timlin	mst@cdc.noaa.gov	497-6295	off site	Associate Scientist
Robert Webb	rwebb@cdc.noaa.gov	497-6967	1D107	Physical Scientist
Klaus Weickmann	kmw@cdc.noaa.gov	497-6720	1D125	Meteorologist
Jeffrey Whitaker	jsw@cdc.noaa.gov	497-6313	1D124	Physical Scientist
Chris Winkler	crw@cdc.noaa.gov	497-6329	1D104	Associate Scientist
Klaus Wolter	kew@cdc.noaa.gov	497-6340	1D607	Research Scientist
Scott Woodruff	sdw@cdc.noaa.gov	497-6747	1D129	Computer Specialist
Taiyi Xu	tx@cdc.noaa.gov	497-6343	ID128	Assoc. Scientist

APPENDIX A

Guide to Acronyms and Abbreviations

AAM	Atmospheric Angular Momentum
AGCM	Atmospheric General Circulation Model
AL	OAR Aeronomy Laboratory Boulder, CO
AMIP	Atmospheric Modeling Intercomparison Project
ARCs	OGP Applied Research Centers
ARL	OAR Air Resources Laboratory Washington, DC
ATM	Asynchronous Transfer Mode
BRAN	Boulder Research and Administrative Network
CCA	Canonical Correlation Analysis
CDC	OAR Climate Diagnostics Center Boulder, CO
CIRES	CU Cooperative Institute for Research in Environmental Sciences Boulder, CO
CLIVAR	Climate Variability and Predictability Research
CMDL	OAR Climate Monitoring and Diagnostics Laboratory Boulder, CO
COADS	Comprehensive Ocean-Atmosphere Data Set
COARDS	Cooperative Ocean-Atmosphere Research Data Standard
CPC	NWS Climate Prediction Center Camp Springs, MD
CRF	Cloud Radiative Forcing

CU	University of Colorado Boulder, CO
DOC	US Department of Commerce Washington, DC
DODS	Distributed Oceanographic Data System
DOE	US Department of Energy Washington, DC
DOI	US Department of the Interior Washington, DC
DSR	David Skaggs Research Center Boulder, CO
ECHAM	European Center/ Hamburg, Germany
ECMWF	European Center/ Hamburg, Germany
ELLFB	Experimental Long-Lead Forecast Bulletin
ENSO	El Niño- Southern Oscillation
EOF	Empirical Orthogonal Function
ESDIM	NESDIS Environmental Services Data and Information Management Program Washington, DC
ETL	OAR Environmental Technology Laboratory Boulder, CO
FRGP	Front Range GigaPOP
FSL	OAR Forecast Systems Laboratory Boulder, CO
GCM	Global Climate Model
GCOS	Global Climate Observing System
GEWEX	Global Energy and Water Cycle Experiment
GFDL	OAR Geophysical Fluid Dynamics Laboratory Princeton, NJ
GLERL	OAR Great Lakes Environmental Research Laboratory Ann Arbor, MI
GSFC	NASA Goddard Space Flight Center Greenbelt, MD

GWD	Gravity Wave Drag
IRI	International Research Institute for Climate Prediction Palisades, NY
ITCZ	Intertropical Convergence Zone
KD	Kawasaki Disease
LAN	Local Area Network
LIM	Linear Inverse Modeling
MEI	Multivariate ENSO Index
MJO	Madden-Julian Oscillation
MLM	Maximum Likelihood Method
MLM	Mixed Layer Model
MOA	Memorandum of Agreement
MPP	Massively Parallel Processor
MRF	Medium-Range Forecast
NAO	North Atlantic Oscillation
NAS	Network Attached Storage
NASA	National Aeronautics and Space Administration Washington, DC
NCAR	National Center for Atmospheric Research Boulder, CO
NCDC	NESDIS National Climatic Data Center Asheville, NC
NCEP	National Center for Environmental Prediction Camp Springs, MD
NESDIS	NOAA National Environmental Satellite Data and Information Service Silver Spring, MD
NGDC	NESDIS National Geophysical Data Center, Boulder, CO
NMFS	NOAA National Marine Fisheries Service Silver Spring, MD
NOAA	DOC National Oceanic and Atmospheric Administration Silver Spring, MD

NODC	NESDIS National Oceanographic Data Center Washington, DC
NOMADS	NOAA Operational Model Archive and Distribution System
NOS	NOAA National Ocean Service Silver Spring, MD
NSF	National Science Foundation Washington, DC
NVDS	National Virtual Data System
NWP	Numerical Weather Prediction
NWPPC	Northwest Power Planning Council Portland, OR
NWS	NOAA National Weather Service Silver Spring, MD
OAR	NOAA Office of Oceanic and Atmospheric Research Silver Spring, MD
OAS	Organization of American States Washington, DC
OBS	Observations
OCN	Optimal Climate Normals
OGP	OAR Office of Global Programs
OLR	Outgoing Long-range Radiation
PDF	Probability Density Function
PNA	Pacific/ North America
QBO	Quasi-biennual Oscillation
QG	Quasigeostrophic
RISA	Regional Integrated Sciences Assessments
RMS	Root Mean Square
SACZ	South Atlantic Convergence Zone
SLP	Sea Level Pressure
SMP	Symmetic multi-processor
SST	Sea Surface Temperature

SSTA	Sea Surface Temperature Anomaly
TOGA-COARE	Tropical Ocean Global Atmosphere Comprehensive Ocean Atmosphere Research Experiment
USGS	DOI United States Geological Survey Washington, DC
WAN	Wide Area Network
WEE	Western Equine Encephalitis
WRCC	NESDIS Western Regional Climate Center Reno, NV
WWA	NOAA-CIRES Western Water Assesment